Chemical and Dynamical Evolution of Early-Type Galaxies

Nicholas Adam Scott

Christ Church, Oxford

Trinity 2011

Thesis submitted in candidature for the degree of Doctor of Philosophy

Declaration

I declare that no part of this thesis has been accepted or is currently being submitted, for any degree or diploma or certificate or any other qualification at this University or elsewhere.

This thesis is the result of my own work unless otherwise specified.

The JAM modelling described in Chapter 2 was developed and carried out by Michele Cappellari, who also implemented the improvements to the JAM modelling technique described at the end of Chapter 2. 24 of the MGE and JAM models for the SAURON sample were produced by Michele Cappellari and are presented in Cappellari et al. (2006). The ATLAS^{3D} survey used in Chapter 4 was selected, observed, reduced and analysed by the ATLAS^{3D} team, (led by Michele Cappellari, Eric Emsellem, Davor Krajnovic and Richard McDermid) of which I am a full member. In addition to what is reported in this thesis I undertook the observations and the measurements of line strength indices and stellar population parameters. The analytic calculation of the effect of major mergers on V_{esc} in Section 4.8.1 was determined in collaboration with Eric Emsellem. The N-body merger simulations in the same section were provided by Maxime Bois. The observations of the SWIFT Coma ETG sample described in Chapter 5 were carried out in part by the SWIFT team as part of the calibration of the instrument.

Parts of this thesis have been submitted for publication in (or are to be submitted to) the following refereed journals:

Parts of Chapters 2 and 3: Scott N., et al., *The SAURON Project - XIV. No escape from V_{esc}: a global and local parameter in early-type galaxy evolution*, 2009, MNRAS, 398, 1835

Parts of Chapters 2 and 4: Scott N., et al., *The ATLAS^{3D} Project - ??. Towards an understanding of the role of V_{esc} in early-type galaxy evolution*, to be submitted

Parts of Chapter 5: Thatte N., Tecza M., Clarke F., Goodsall T., Fogarty L., Houghton R., Salter G., Scott N., Davies R. L., Bouchez A., Dekany R., *The Oxford SWIFT Spectrograph: first commissioning and on-sky results*, 2010, SPIE, 7735, 258

Parts of Chapters 5 and 6: Scott N., et al., *An IFU view of early-type galaxies in the Coma cluster*, to be submitted

Chemical and Dynamical Evolution of Early-Type Galaxies

Nicholas Adam Scott
Christ Church, Oxford

Trinity 2011

Thesis submitted in candidature for the degree of Doctor of Philosophy

Abstract

In this work I have examined the spatially resolved properties of the local early-type galaxy population. Using Hubble Space Telescope and ground based photometry I constructed Jeans Anisotropic Multi Gaussian Expansion models of the SAURON sample of early-type galaxies, from which I determined the depth of the local gravitational potential well, quantified by the local escape velocity, V_{esc}. I found that V_{esc} correlated tightly with the three Lick indices: Mgb, Fe5015 and Hβ. The Mgb-V_{esc} relation within individual galaxies is identical to that between different galaxies; the relation is both *local* and *global*. The Mgb-V_{esc} relation is: $\log \mathrm{Mgb} = (0.35 \pm 0.01) \log V_{esc} - (0.41 \pm 0.03)$. While the metallicity, [Z/H] is correlated with V_{esc} it does not show the same local and global behaviour. Age (t) and alpha enhancement ([α/Fe]) are only weakly correlated with V_{esc}. A combination of [Z/H] and t is tightly correlated with V_{esc}, with scatter comparable to the Mgb-V_{esc} relation, and does show the local and global behaviour. This combination is given by: $\log V_{esc} = 0.85[\mathrm{Z/H}] + 0.43 \log t$.

Using the volume limited ATLAS^{3D} sample of 260 local ETGs I examined in detail the behaviour of the Mgb-V_{esc} relation and its dependence on other galaxy properties. I found that systematic deviations from the relation correlate with the local environmental density and molecular gas mass of a galaxy, and with the local [α/Fe] measurement. I found that there is a population of galaxies that do not follow the relation, found only at $V_{esc} < 400\ \mathrm{kms}^{-1}$. These galaxies have negative gradients, high central Hβ indices and young (t < 3 Gyrs) ages. Using stellar population models I demonstrated that these negative gradient galaxies are perturbed from the relation by recent star formation and will return to the relation as they age.

I also describe the observation, reduction and analysis of a new sample of ETGs in the core of the Coma cluster, the highest density environment in the local Universe, observed with the SWIFT Integral Field Spectrograph. I determined the fraction of slow rotators in the sample, comparing it to results from the ATLAS^{3D} survey, and found an enhanced slow rotator fraction in the Coma cluster. I also determined the Fundamental Plane of Coma early-type galaxies, given by: $\log R_e = (1.20 \pm 0.22) \log \sigma_e - (0.79 \pm 0.09) \log \langle I_e \rangle$.

Support and facilities used

I would like to thank the Science and Technology Facilities Council for the support of an STFC studentship that has allowed me to study for a DPhil. I would also like to thank Christ Church for a graduate grant and the European Southern Observatory for support as an unpaid associate.

The research in this thesis has been made possible due to extensive use of observational facilities. The SAURON and ATLAS^{3D} surveys are based on observations made with the William Herschel Telescope operated on the island of La Palma by the Isaac Newton Group in the Spanish Observatorio del Roque de los Muchachos of the Instituto de Astrofsica de Canarias. The Isaac Newton Telescope at the same facility was used to provide additional photometry for the ATLAS^{3D} survey. Photometry for the SAURON survey was obtained at the 1.3m McGraw-Hill Telescope of the MDM Observatory and from the Hubble Legacy Archive, based on observations made with the NASA/ESA Hubble Space Telescope, which is a collaboration between the Space Telescope Science Institute (STScI/NASA), the Space Telescope European Coordinating Facility (ST-ECF/ESA) and the Canadian Astronomy Data Centre (CADC/NRC/CSA). The majority of the photometry for the ATLAS^{3D} survey was obtained from the SDSS archive. Funding for the SDSS and SDSS-II has been provided by the Alfred P. Sloan Foundation, the Participating Institutions, the National Science Foundation, the U.S. Department of Energy, the National Aeronautics and Space Administration, the Japanese Monbukagakusho, the Max Planck Society, and the Higher Education Funding Council for England. The SDSS Web Site is http://www.sdss.org/. The SDSS is managed by the Astrophysical Research Consortium for the Participating Institutions. The Participating Institutions are the American Museum of Natural History, Astrophysical Institute Potsdam, University of Basel, University of Cambridge, Case Western Reserve University, University of Chicago, Drexel University, Fermilab, the Institute for Advanced Study, the Japan Participation Group, Johns Hopkins University, the Joint Institute for Nuclear Astrophysics, the Kavli Institute for Particle Astrophysics and Cosmology, the Korean Scientist Group, the Chinese Academy of Sciences (LAMOST), Los Alamos National Laboratory, the Max-Planck-Institute for Astronomy (MPIA), the Max-Planck-Institute for Astrophysics (MPA), New Mexico State University, Ohio State University, University of Pittsburgh, University of Portsmouth, Princeton University, the United States Naval Observatory, and the University of WashingtonThe SWIFT data were observed on the 200" Hale Telescope at the Palomar Observatory, which is funded and run by the California Institute of Technology. In addition this research has made use of the Hyperleda and NED databases.

Acknowledgements

I would like to thank my supervisors, Roger Davies and Michele Cappellari, for their help in producing this thesis but more importantly for guiding me throughout the course of my DPhil. I would like to thank the SAURON and ATLAS^{3D} teams for the opportunity to be a part of two very exciting projects. In particular I would like to thank Eric Emsellem, Davor Krajnovic, Richard McDermid, Harald Kuntschner and Jesus Falcon-Barroso for their advice and insight on various aspects of this work. I would also like to thank the SWIFT team, in particular Fraser Clarke, Ryan Houghton, Mathias Tceza and Niranjan Thatte for welcoming me into the group and working with me on the observation and reduction of SWIFT data. Many thanks to the observatory staff at Palomar and Roque de Los Muchacos; when ash was falling from the sky or the telescope just refused to move you were always there to help.

I would like to thank Christ Church for its support, both financial and otherwise. Thanks to the GCR community, for providing an escape from the world of astrophysics when I'd spent too long staring at a computer screen. I would like to thank the Oxford astrophysics graduate students for making that world an enjoyable place to work and play. I would like to thank the staff, fellows and students of the European Southern Observatory for making me feel so welcome in Munich. Particular thanks go to Markus Kissler-Partig for giving me the opportunity to spend time at ESO in the first place. I would like to thank Helen Bones for proof reading this thesis, and for being much better with words than I am. Finally I would like to thank my parents for supporting and encouraging me through many years of education. I hope you are all as proud of this work as I am.

Contents

Chapter 1

Introduction

It is almost a century since astronomers first confirmed galaxies as objects external to our own Milky Way (Curtis, 1921; Shapley, 1921; Hubble, 1936). Since that time galaxies have been studied extensively as systems that are physically interesting in themselves but also as probes of the wider history of the Universe. As the dominant collections of luminous matter in the Universe, galaxies are our principal tool in studying the evolution of the Universe after the early years of the Big Bang and the decoupling of the Cosmic Microwave Background (CMB) radiation. Galaxies as we observe them today contain information about many billions of years of cosmic evolution. Galaxy evolution proceeds under a framework established by the cosmological evolution of the Universe; the two are intrinsically linked. To further our understanding of galaxy evolution we must first understand the cosmological framework.

While observations at redshifts greater than zero allow us to directly follow this evolutionary process, we will always have more detailed information on the local population of galaxies because of their proximity and therefore their large apparent brightnesses. Local early-type galaxies (ETGs) in particular are thought to represent the end-point of the evolutionary process for massive galaxies. Understanding their evolutionary histories can reveal many of the physical processes that play a role in

galaxy evolution. They are also important in a cosmological context, as at any given redshift they are amongst the most luminous objects and so the most available probes of the high-redshift Universe. Detailed observations of the local ETG population can be used to test our current paradigm of galaxy formation, as well as give direct information on the physical processes occurring in galaxies today.

In this chapter I will briefly discuss our current understanding of cosmology and the paradigm for galaxy evolution, focusing in particular on areas relevant to ETG formation. In the second section I will describe the properties of the local ETG population and empirical relations observed between some of these properties. In the final section I will outline the contents of the rest of this work.

1.1 Cosmology and Galaxy Evolution

1.1.1 The Big Bang and the expanding Universe

Observational cosmology began with Edwin Hubble's observation that, on average, galaxies are receding from us and the rate of recession is proportional to their distance (Hubble, 1929). This recession, combined with the assumption that the Universe is isotropic and homogeneous, led naturally to the notion that the Universe had a beginning. The Big Bang Theory (Lemaître, 1931; Gamow, 1948) was confirmed by the observation of the CMB (Penzias & Wilson, 1965), the light relic of the early expansion of the Universe. Detailed observations of the CMB have allowed us to constrain the energy-content of the Universe, the nature of the expansion and early inhomogeneities in the mass distribution of the Universe (Spergel et al., 2003). A Universe with a beginning, as opposed to a static Universe, is by necessity a changing and evolving Universe. The Universe, and in particular the galaxy population, was very different ~ 10 billion years ago.

1.1.2 Dark matter and structure formation

Observations of the CMB, Baryon Acoustic Oscillations (BAOs; Eisenstein et al., 2005; Percival et al., 2010) and high-redshift Type 1a supernovae (Riess et al., 1998; Perlmutter et al., 1999; Astier et al., 2006) suggest our Universe contains 72 per cent dark energy and 28 per cent matter, however the nature of these constituents is not yet clear. The theory of Big Bang nucleosynthesis (Alpher et al., 1948; Walker et al., 1991; Copi et al., 1995), combined with censuses of baryonic matter (essentially stars and gas; e.g. Fukugita et al., 1998) show a significant shortfall in the amount of baryonic matter we observe, compared to the CMB predictions. The existence of additional non-luminous mass was first postulated by Fritz Zwicky in the 1930s (Zwicky, 1933, 1937), based on the dynamics of the Coma cluster. Several decades later, further observations of the Coma cluster (Rood et al., 1972) and galaxy rotation curves (Rubin & Ford, 1970) confirmed this excess of gravitational mass that could not be accounted for by normal matter alone. The presence of this additional gravitating mass or dark matter (DM) has been confirmed across a large range of scales using a variety of different techniques from galaxy dynamics (van Albada et al., 1985; Gerhard et al., 2001; Cappellari et al., 2006; Thomas et al., 2007) to strong and weak lensing (Wittman et al., 2000; Refregier, 2003; Treu & Koopmans, 2004) and X-ray observations of hot gas (Evrard et al., 1996; Lewis et al., 2003). Taken together these observations define our current understanding of the Universe and are encapsulated by the dark energy - cold dark matter ΛCDM paradigm (see for example, Ostriker & Steinhardt, 1995; Coles, 2005; Springel et al., 2006).

The dynamical history of the Universe can be viewed as the history of the growth of structures in the Universe. These structures began as quantum scale fluctuations in the smooth distribution of the very early Universe. Their signature is visible as temperature fluctuations in the CMB. At late times these quantum fluctuations have evolved into the galaxies and clusters of galaxies we observe in the low redshift

Universe. For most of the history of the Universe this evolution has been driven by gravitational interactions, dominated by dark matter. Dark matter, unlike baryonic matter, does not 'feel' the electromagnetic force, so its interactions are all dissipationless making it comparatively straightforward to model over a large range of scales. Dark matter-only simulations of cosmological volumes (Press & Schechter, 1974; Davis et al., 1985; Kauffmann & White, 1993) are able to reproduce, in a statistical sense, observations of large-scale structure (for example the 2-degree-Field Galaxy Redshift Survey (2dFGRS) Percival et al., 2001). In these simulations the most massive structures are produced at late times from the merger of less massive units; this is known as 'hierarchical assembly'.

1.1.3 Galaxy formation

Dark matter provides the framework for galaxy formation to occur. As dark matter structures collapse and merge they carry baryonic matter along with them. Galaxies are thought to form inside individual dark matter structures, commonly known as dark halos (White & Rees, 1978; Navarro et al., 1996). Gas condenses to form stars as the dark halo becomes sufficiently massive, and as halos merge so do their gaseous and stellar components. While both dark matter and stars have dissipationless interactions this is not the case for gas, which experiences much more complicated physics. Dissipation, star formation, gas cooling and heating and chemical enrichment are only some of the complex processes that have to be modelled to successfully reproduce the baryonic evolution of the Universe.

A variety of different modelling techniques are used to attempt to reproduce this complicated baryonic physics. Studies cover a broad range of scales, from cosmological volumes covering several hundred square megaparsecs , through clusters and groups of galaxies down to the scale of individual galaxies (Kauffmann et al., 1993; Cole et al., 1994; Springel et al., 2001; Naab et al., 2007). Even when modelling a single galaxy, modern computing power is insufficient to resolve the scales on which

star formation and similar processes occur. The simulations deal with this using so-called 'sub-grid' physics - by introducing analytic recipes to reproduce the effect of these small-scale processes. Semi-analytic models (SAMs) take this idea to its natural conclusion by combining the dark matter-only halo merger trees with a full set of analytic recipes to describe all aspects of baryonic physics. In order to reproduce the observed luminosity-function (LF) of galaxies (Schechter, 1976; Blanton et al., 2001; Norberg et al., 2002; Bell et al., 2003) the SAMs had to introduce the idea of feedback. The role of feedback, from both active galactic nuclei (AGN; Silk & Rees, 1998) and supernovae (Dekel & Silk, 1986; Mac Low & Ferrara, 1999) is not well understood, but is believed to be crucial in quenching star formation in massive galaxies (Bower et al., 2006; Croton et al., 2006). Inconsistencies between the models and observations typically indicate problems with how the models address the baryonic physics. Adjusting the treatment of the baryonic physics in the models should be guided by observational results.

Observations with redshift

Observations at intermediate and high redshift are particularly useful for refining the treatment of baryons in simulations. These observations provide direct information on the time dependence of various galaxy properties. Observing high redshift galaxies has the drawback that these objects are significantly fainter than nearby galaxies, not only due to the natural $1/r^2$ dimming but also because of the redshifting and stretching of the light, resulting in the luminosity being inversely proportional to $(1+z)^3$. These galaxies also appear significantly smaller, as apparent angular size also decreases with redshift. While these effects make high-redshift observations challenging the advent of the Hubble Space Telescope (HST) and ground-based 8 and 10m class telescopes with adaptive optics has made the study of the high-redshift Universe feasible.

While many diverse observations have contributed to the current generation of

cosmological simulations I will only describe three of the most significant here. I focus on these three observational results because they have had significant impact, but also because they are most relevant to the evolutionary histories of the local ETG population. Perhaps the most obvious way to study galaxy evolution is to simply count the number of galaxies of a given absolute luminosity (the LF) at each redshift. The two principal studies to attempt this are the Deep Extragalactic Evolutionary Probe survey (DEEP1 and DEEP2, Im et al., 2002; Willmer et al., 2006) and the Classifying Objects by Medium-Band Observations survey (COMBO-17; Wolf et al., 2003). Faber et al. (2007) summarises the findings, concluding that the number and typical luminosity of blue galaxies remain constant between z= 0 and 1, however the number of red galaxies increases by a factor ~ 2.

The second key observational result I wish to highlight is the measurement of the universal star formation rate (SFR) as a function of redshift. This was first determined up to z$\sim$ 1 by Lilly et al. (1996) and Madau et al. (1998) using UV flux to determine the SFR. They found that the global SFR steadily increased with redshift over the range of their observations. Recent work by, for example, Bunker et al. (2004) and Giavalisco et al. (2004) has extended these measurements up to z ~ 6, finding that the universal SFR carried on increasing with redshift up to a peak at z $\sim$ 2, before declining slowly at higher redshifts. This also coincides with the peak in Universal AGN activity (Schmidt, 1968; Pei, 1995; Fan et al., 2001b).

The last key observational result to consider is also connected to star formation. As well as measuring the global amount of star formation, several groups have also examined what kind of objects dominate the global SFR at a given redshift. One might expect that as the hierarchical assembly paradigm suggests the most massive objects form last they should provide the dominant contribution to the global SFR at late times. However, observations suggest the exact opposite of this: the typical mass of a star forming galaxy decreases with redshift. This trend, first highlighted by Cowie et al. (1996), is known as 'downsizing'. Other examples of

this downsizing behaviour include: the most massive galaxies typically contain the oldest stars (Thomas et al., 2005), massive quiescent galaxies are observed out to redshifts ≥ 2.5 (Daddi et al., 2005; Yamada et al., 2005) and the faint end of the LF shows greater evolution at low redshift than the bright end (Glazebrook et al., 2004; Cimatti et al., 2006). The semi-analytic models are able to accommodate these observations by forming stars at high redshift then assembling them into individual dynamical structures (galaxies) at low redshift (Springel et al., 2005; Bower et al., 2006). This allows the most massive galaxies to still be assembled at late times (as predicted by hierarchical assembly) while ensuring that their stars are actually formed at early times. This requires that the majority of stars in the most massive galaxies were not formed in their current host halo.

Influence of environment

As well as variations of galaxy properties with mass and redshift, there are also variations with the local environment around the galaxy. Environments are typically classified as either field (low density), group (intermediate density) or cluster (high-density), and can be quantified in various ways including local number density, luminosity density, mass density or distance to the xth nearest neighbour. Historically, the first environmental effect to be observed was the morphology-density relation: that the proportion of ETGs increases with increasing local density (Oemler, 1974; Dressler, 1980; Postman & Geller, 1984). This effect is closely linked to the SFR-density relation, where the mean SFR of a galaxy decreases with increasing density (Gómez et al., 2003).

High-density environments also show differential evolution compared to low density environments. One example of this is the Butcher-Oemler effect (Butcher & Oemler, 1984) that in rich clusters of galaxies there is rapid evolution of the fraction of blue galaxies from $z \sim 0.5$ to $z = 0$. No such evolution is observed in group or field environments, where the fraction of blue galaxies remains relatively con-

stant over that time. Similarly, the morphological Butcher-Oemler effect (Butcher & Oemler, 1978) is a rapid evolution in the morphological mix of rich clusters that is not observed in less dense environments over the same redshift range. Rich clusters show a rapid decrease in the fraction of spiral galaxies with a corresponding rise in the ETG fraction. Studies of the stellar populations in high - and low-density environments suggest cluster galaxies have more rapid or truncated star formation histories (Thomas et al., 2005; Bernardi et al., 2006).

The simulations described in Section 1.1.3 also predict a dependence on the local environment of a galaxy. Simulations suggest a range of potential physical processes that can lead to the observed environmental effects, though the strength of these trends is typically over-predicted in the simulations. Most of the physical mechanisms occur only in the highest density environments, whereas observations show the trends with environment are present even at low densities (Cappellari et al., 2011b). The mechanisms driving these environmental effects are not yet well understood (Balogh et al., 1999). This is due in part to the difficulty of disentangling the effects of mass and environment (Bundy et al., 2006). High density environments contain the most massive galaxies which are typically absent in the field. This differing mass function naturally produces differences in the galaxy populations of high and low density environments, but this is *not* an environmental effect. It is residual trends after this mass dependence has been accounted for that show the influence of environment. Additional observations of the variation of a range of galaxy properties with environment are required to properly identify which physical processes are driving the observed trends.

1.2 Early-Type Galaxies

After outlining the current state of galaxy formation theories (and how observations have shaped those theories) in the previous section I will now move on to describe

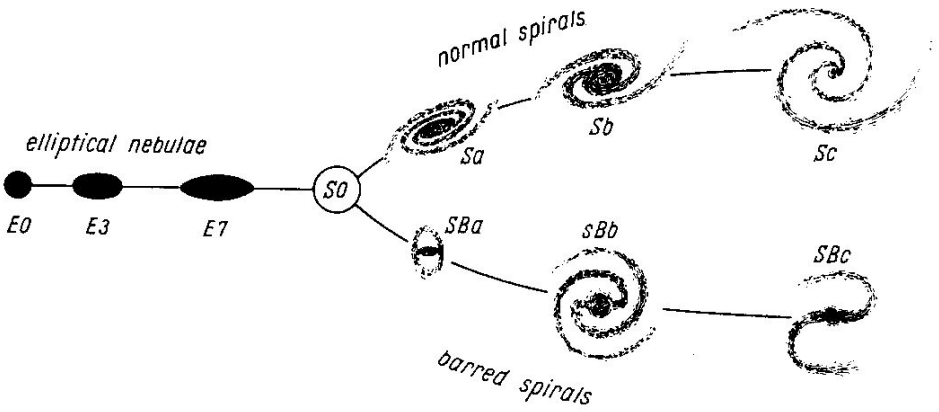

Figure 1.1: The Hubble tuning fork diagram, taken from Hubble (1936). Early-type galaxies occupy the left hand side of the diagram, from E0 to S0.

the detailed properties of early-type galaxies in the local Universe. ETGs have been extensively studied both locally and at higher redshifts and much is known about their dynamics, stellar populations and gas content. I will predominantly focus here on their low-redshift properties as that regime is the focus of this work, but I will also outline trends with redshift where important. The local ETG population is an important test of theories of galaxy evolution, and detailed studies of its properties can help refine and improve those theories.

1.2.1 Defining Early-Type Galaxies

Before discussing their properties it is first necessary to define precisely what an ETG is. Only massive galaxies, those with masses greater than $\sim 10^{9.5}\mathrm{M}_{\odot}$ are considered to be ETGs (I will not examine dwarf galaxies in this work). The traditional (and most common) definition of an ETG is based on morphology and Hubble's tuning fork diagram (Figure 1.1). ETGs make up the left hand side of this diagram, consisting of ellipticals (Es) and lenticulars (S0s), as opposed to late-type spiral galaxies. One disadvantage of the Hubble system is that it cannot be applied to highly inclined systems because spiral structure cannot be identified. This leads to a degeneracy between edge-on S0s and spirals. In this work I will be adopting the simple Hubble-based definition of an ETG, stated by Sandage (1961), as any mas-

sive galaxy that does not have spiral structure or, in the case of edge on galaxies, a prominent dust lane.

Defining ETGs as any massive galaxy that does not show spiral structure works well at low redshift where deep, high resolution photometry is easily available, and for small samples where visual classification can be carried out. However, at higher redshifts and for large samples of galaxies other techniques need to be used. Many approaches have been explored, including bulge-to-total decomposition, Sérsic profile fitting (Sersic, 1968; Graham & Driver, 2005), classifications based on concentration, clumpiness and asymmetry and the Gini coefficient (Abraham et al., 1994; Bershady et al., 2000; Lotz et al., 2004). None of these systems are able to fully reproduce the Hubble classification (Andrae et al., 2011).

An alternative way of defining ETGs is based on their stellar populations and star formation histories. Many authors have defined ETGs as passive galaxies with little or no star formation and predominantly old stellar populations. Selecting a sample based on either of these criteria is relatively consistent with the Hubble classification for ETGs. Practically this can be done from photometry by selecting based on galaxy colour (old stellar populations have red colours; Baldry et al., 2004), or from spectroscopy based on emission line fluxes (typically Hα). If photometry or spectroscopy covering a broad wavelength range is available then an ETG-like sample can also be selected based on their spectral energy distributions. Colour-based classifications can suffer from significant contamination due to the effects of dust, which artificially reddens galaxy colours. Even purely passive galaxies become bluer at high redshift due to the the younger stellar ages. Any stellar population based classification must take into account this passive evolution in some way.

Finally, ETGs can be defined dynamically as systems that are dominated by pressure support rather than rotational support. Dynamically selected samples are less common that those based on morphology or stellar population because obtaining the high S/N spectroscopy needed to determine dynamical information requires a

large amount of telescope time. A dynamical classification has the advantage that it is robust against projection or evolution effects. It is not clear that this definition is consistent with either the morphological or stellar population based definitions described above.

1.2.2 Classifying ETGs into sub-populations

Much work has been devoted to dividing ETGs into two or more sub-classes. Identifying different populations of ETGs can be useful in that it may be indicative of different formation mechanisms and evolutionary paths for the different sub-classes, which can in turn help to identify the physical processes in play. However, this is only true if the division into sub-classes is physically motivated. It is one of the common pitfalls of scientific research to interpret a continuum of properties as a bimodality, leading to potentially false conclusions.

ETGs have historically been classified into two broad types, Es and S0s. This division suffers from the inclination effects described above - from morphology alone it is very challenging to differentiate between face-on Es and S0s. Additionally, it is possible to view the E/S0 division as a continuum in bulge-to-total ratio rather than as a truly bimodal distribution. Other authors have suggested dividing ETGs by the details of their light profiles. One common approach is to quantify the deviations from purely elliptical isophotes, dividing ETGs into those with boxy or disky isophotes (Kormendy & Bender, 1996). Boxiness or diskiness was found to correlate with radio and X-ray luminosity and with degree of rotation (Bender et al., 1989). However, this scheme again suffers from contamination due to inclination effects (Binney et al., 1990) and the presence of bars and it is unclear how this subdivision relates to the physical process of galaxy formation.

The current trend is to favour one of two competing classification schemes. In the first, galaxies are classified based on their detailed surface brightness profiles into those with a central light excess or deficit (Kormendy et al., 2009). A Sérsic

profile is fit to the outer parts of the object and the extrapolation of the profile into the centre of the object is compared to the observed surface brightness. The alternative approach uses integral field spectroscopy to determine the specific angular momentum for an object, and then classifies an ETG as either a Fast Rotator (FR) or Slow Rotator (SR) based on this parameter (Emsellem et al., 2007). This classification scheme is discussed in more detail in Chapter 6. Both classification systems correlate well with other galaxy properties and can also be related to differences in the physical processes that form the sub-classes. There is reasonable agreement between the two systems, though comparisons currently only cover a small number of objects (Emsellem et al., 2011). Both classification schemes also correlate with a broad range of galaxy properties such as mass, rotation, apparent flattening, kinematically decoupled components and the presence of a hot X-ray halo (Emsellem et al., 2007). While there is significant support for a bimodal classification scheme these studies cannot rule out the idea that a single continuum of properties can describe the entire ETG family.

1.2.3 Dynamical properties of ETGs

Having defined what an ETG *is* (in the context of this work) I will now move on to describe some of the properties of ETGs. In order to progress our understanding of galaxy evolution it is not enough to consider individual galaxy properties in isolation. We must also examine the relationship between different properties. In the remainder of this introduction I will focus on some of the key relationships between ETG properties and how these observational results can be used to advance the theory of galaxy evolution. I will begin by describing those observations that pertain to principally dynamical quantities and then move on to the chemical properties of ETGs.

Early observational correlations

The most basic photometric properties of a galaxy are its luminosity (L) and size (R). The simplest spectroscopic property of a galaxy is its central velocity dispersion, σ_0. Once the distance to a galaxy has been accurately determined (which is itself a challenging and complex task which I will not address here) it becomes possible to determine intrinsic luminosities and sizes for objects (as opposed to apparent quantities) and to compare these properties between a sample of ETGs. Faber & Jackson (1976) found a tight correlation between L and σ, $\mathrm{L} \propto \sigma^4$, known as the Faber-Jackson relation. Around the same time, Kormendy (1977) discovered a correlation between the effective surface brightness $\langle I_e \rangle$ and the effective radius, R_e (the radius which contains one half of a galaxy's total light), in the sense that larger galaxies have fainter $\langle I_e \rangle$.

The Fundamental Plane

As well as the two observed correlations described above, L, R_e and $\langle I_e \rangle$ are related by definition: $\mathrm{L} = 2\pi \langle I_e \rangle \mathrm{R}_e^2$. This definition allows relations to be constructed between any of the four variables discussed here, σ_0, L, R_e and $\langle I_e \rangle$. It was noticed that the residuals from these relations are correlated, which suggests that a tighter relationship can be constructed by combining 3 (or more) of the variables compared to any pair of variables alone. This was investigated initially by Djorgovski & Davis (1987) and Dressler et al. (1987), who found they were able to construct a tight relationship between σ_0, R_e and $\langle I_e \rangle$. This relation is known as the Fundamental Plane (FP) of ETGs.

A FP arises naturally from the Virial Theorem. This theorem states that any isloated, relaxed dynamical system must satisfy:

$$2K + U = 0 \tag{1.1}$$

where K is the total kinetic energy and U is the total potential energy of the system. Applying this to a collection of stars and noting that the potential energy of a galaxy comes entirely from its gravitational potential this leads to:

$$\mathrm{R}_e \propto \sigma_0^2 \langle I_e \rangle^{-1} \left(\mathrm{M/L}\right)^{-1} \tag{1.2}$$

which is the Virial Theorem prediction for the FP.

The FP has been studied by many authors in increasingly large samples of galaxies (Bernardi et al., 2003). Studies within individual clusters of galaxies have proved to be the most fruitful approach (Jorgensen et al., 1996) as this eliminates the need to determine the distances to individual objects, a significant source of error in the FP. While there is some disagreement between individual studies over the precise form of the FP it is clear that the observed FP is 'tilted' with respect to the Virial prediction. The best-fitting FP from Jorgensen et al. (1996) is given by:

$$\mathrm{R}_e \propto \sigma_0^{1.24} \langle I_e \rangle^{-0.82} \tag{1.3}$$

The cause of this tilt is not yet known, but is likely due to variations in the mass-to-light ratio (M/L) along the plane (Renzini & Ciotti, 1993). This variation may be due to systematic trends in the stellar M/L due to differing star formation histories (SFHs) or initial mass functions, different contributions of dark and luminous matter or a differing relative distribution between the dark and luminous mass (Cappellari et al., 2006; Thomas et al., 2011). The FP is one of the key observational tests of theories of galaxy evolution.

Other dynamical relations

As well as the FP ETGs obey other dynamical relations. As discussed in Section 1.2.1 ETGs are predominantly dispersion dominated systems (Bertola & Capaccioli, 1975; Binney, 1979), however the amount of rotation varies significantly with the

luminosity of the galaxy (Davies et al., 1983). This can be quantified by V/σ, the ratio of the peak rotational velocity to the velocity dispersion (Binney, 1977) or the specific stellar angular momentum, λ_R (Emsellem et al., 2004, discussed in detail in Chapter 6). Both these quantities show trends with mass, in that V/σ and λ_R are typically lower in more massive galaxies.

1.2.4 Chemical properties

As well as obeying purely dynamical relations ETGs also show strong correlations between their chemical properties. I use chemical properties to refer to any quantities relating to the stellar populations and cold gas content of ETGs. As well as being correlated with one another there are also relations linking the dynamical and chemical properties of ETGs. These correlations can be divided into two broad groups; those driven by the bulk of the old stars and those related to recent and ongoing star formation, and the potential for future star formation in the form of cold gas.

Stellar populations and SFHs

As mentioned in Section 1.2.1 on the definition of an ETG, most ETGs have red optical colours. When plotted against their absolute magnitude ETGs predominantly define a tight 'Red Sequence' of galaxies (Visvanathan & Sandage, 1977). This is in sharp contrast to late-types, which typically lie in a much less well defined region known as the 'Blue Cloud'. In addition there is a region known as the 'Green Valley' thought to consist of objects that are currently transitioning from the red sequence to the blue cloud or objects that are significantly reddened by dust (Cowie & Barger, 2008). The narrow range in optical colours spanned by ETGs suggests that these objects have similar SFHs and, given their redness, that their stars were formed at high redshift ($z \geq 1.5$, Thomas et al., 2005). Optical colours cannot uniquely constrain the SFH of a galaxy, as red colours can be the result of either old

or metal-poor stars. The red sequence has been observed out to z $\sim$ 2 and shows predominantly passive evolution, however different authors disagree over the rate of build up of the bright and faint ends of the sequence (Yamada et al., 2005; Faber et al., 2007).

Further information on the stellar populations of ETGs can be obtained from spectroscopy. The absorption line strengths, like the optical colours, are driven by the SFH of a galaxy. It is unsurprising then that measurements of the central absorption line strengths of ETGs were found to correlate with their dynamical properties. The most well-studied of these correlations is the Mg-σ relation (Bender et al., 1992; Colless et al., 1999). Like the colour-magnitude relation this has been studied for large samples of galaxies, however neither Mg or σ depend on distance so the Mg-σ relation is much easier to measure and is free from the significant errors related to inaccurate distance determinations.

The colour-magnitude relation relates global quantities of ETGs whereas the Mg-σ relation is between central properties of ETGs. There is also a tight correlation between the *central* line strengths and the *global* optical colours (Bender et al., 1993). This correlation between a central and a global property implies that the gradients of the chemical properties within ETGs are also tightly constrained. Line strength and colour gradients have been studied directly (Franx & Illingworth, 1990; Kuntschner et al., 2006; Sánchez-Blázquez et al., 2006a; Suh et al., 2010) and are found to show a wide variety of behaviours, though ETGs are typically older and more metal rich in their central regions. The presence of recent SF can significantly affect the observed gradients.

Gas content and recent star formation

ETGs are predominantly passive, red systems and this is thought to be due to the fact that they typically lack the large cold gas reservoirs found in late-types. Early neutral hydrogen observations revealed a lack of gas in ETGs consistent with

this picture. However, this lack has proved to be something of a mystery as mass-loss from stars should produce significant quantities of gas (Faber & Gallagher, 1976). Recent work by Young et al. (2011) has shown that many ETGs do possess a molecular gas reservoir and the detection rate is comparable to that found in spiral galaxies of similar mass. In addition, deeper HI observations are beginning to reveal that many ETGs do have an associated neutral-hydrogen component (Morganti et al., 2006), though frequently not in the regular disks found around spirals.

While a small number of ETGs had been observed to show significant SF (typically centrally concentrated) these were generally perceived as atypical of the type. Recent work making use of indicators more sensitive to low levels of SF than the optical colours (e.g. UV colours, FIR emission Yi et al., 2005; Kaviraj et al., 2007; Shapiro et al., 2010) has found that a significant number (> 30 per cent) have low levels of residual SF. Whether this SF and the associated gas reservoirs are entirely attributable to merger events or can remain associated with the ETG itself is as yet unclear.

1.3 Outline of this work

In this chapter I have described our current understanding, both theoretical and observational, of galaxy evolution and in particular the formation history and current state of the local ETG population. While the framework of ΛCDM successfully reproduces many properties of the local galaxy population, baryonic physics is complex and there are still many unanswered questions. In this work I intend to focus on two areas where the picture is not yet complete: the connection between dynamical and stellar population properties of local ETGs and the influence of the local environmental density on those properties. To do this I will use two-dimensional spatially-resolved spectroscopy, complemented by other observations, modelling tools and simulations, where they add useful insight.

The outline of this work is as follows. Chapter 2 describes the dynamical modelling of ETGs from spatially resolved two dimensional spectroscopy, focusing principally on the derivation of the depth of the local gravitational potential well at all points within a galaxy. Chapter 3 compares this quantity to many of the ETG properties discussed in the previous section, focusing on empirical relationships between variables. I also describe the use of stellar population models to examine the correlation of V_{esc} with the underlying physical properties. In Chapter 4 I explore the physical processes that drive correlations with the local potential, and under what conditions these correlations break down. Chapter 5 describes the integral field observations of a sample of ETGs in a dense environment, the Coma cluster, the reduction of this data and the extraction of kinematic information. Chapter 6 briefly describes additional photometry relating to these observations, then presents the FP and λ_R distribution for the sample, comparing this to results from lower-density environments. Finally, I summarise the principal results of this work and briefly discuss their implications for the evolutionary history of local ETGs in Chapter 7.

Chapter 2

Determining the depth of the local potential well in nearby galaxies

2.1 Overview

In this chapter I describe the determination of V_{esc} for local ETGs. I first describe the construction of surface brightness models from photometry, paying particular attention to how effects such as dust and non-axisymmetry are dealt with. Using these photometric models combined with spatially resolved spectroscopy I describe how dynamical models can be applied to model the three dimensional mass distribution of ETGs. Finally I describe how the above techniques can be adapted to deal with large samples of galaxies.

2.2 Summary of the dynamical modelling process

The process of determining the local escape velocity in nearby ETGs involves multiple steps. I describe these steps in detail in later sections but here I provide an overview of the process, briefly outlining each step.

i) Combine and flux-calibrate high-resolution space-based imaging and wide-field

ground-based imaging.

ii) Construct a Multi Gaussian Expansion (MGE) fit to the combined image.

iii) Produce a map of the second moments of the velocity field of the object from integral field spectroscopy.

iv) Use the MGE photometric model as input to the Jeans Anisotropic MGE (JAM) modelling to produce a set of dynamical models covering a range of inclinations, mass-to-light ratios and anisotropies.

v) Compare the observed second moments of the velocity field with the model second moments from the JAM modelling to determine the best-fitting inclination, mass-to-light ratio and inclination.

vi) Using the gravitational potential determined from the JAM modelling fit to the observed second moments determine the local escape velocity and integrate this along the line of sight.

2.3 Photometric data

ETGs are typically highly concentrated objects (e.g. de Vaucouleurs, 1948) and so much of their light (and hence mass) is concentrated in the central few tens of arcseconds. Because of this large central concentration, the gravitational potential and more importantly the kinematics of stars in this region vary rapidly hence require high resolution to resolve. Despite this, a significant fraction of an ETG's light is located at large radii, requiring a large field of view to ensure that the galaxy's total mass is properly accounted for. A large field of view is also essential to ensure that the night sky background is properly subtracted from the image.

Because of this it was necessary to combine two images, one with high resolution covering only the central region of each galaxy with the second covering a much larger

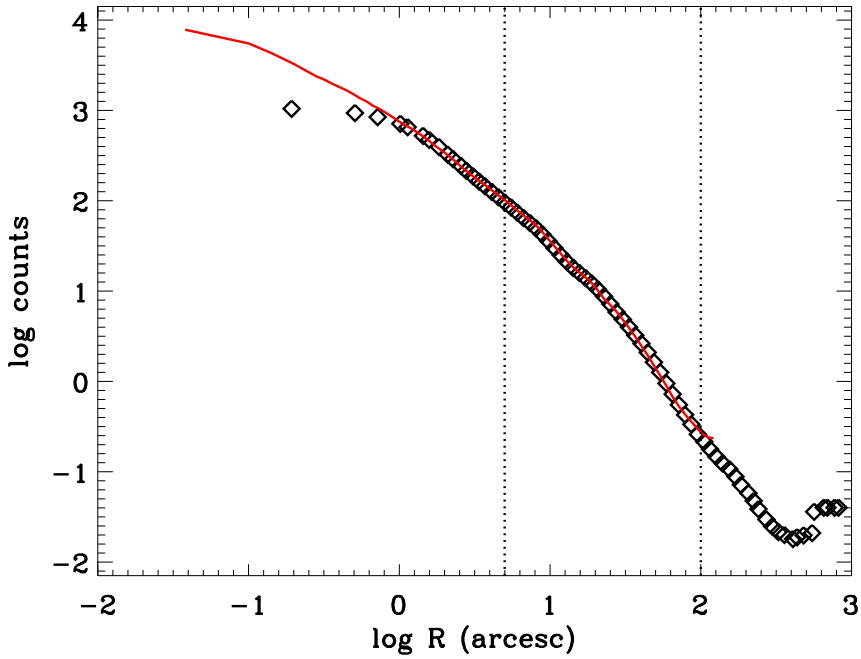

Figure 2.1: Match between the MDM (open diamonds) and HST (solid red line) photometric profiles for NGC4328. The free parameters used to match the two profiles were the sky level of the HST image and the flux scaling factor of the MDM image. The fit was performed over the region of overlap excluding the central 3 arcseconds to avoid PSF and saturation effects.

field of view but having coarser resolution. For the high resolution imaging I use Hubble Space Telescope (HST) Wide Field Planetary Camera 1 and 2 (WFPC1/2) and Advanced Camera for Surveys (ACS) photometric data. These data were obtained from the Space Telescope - European Coordinating Facility archive. The ground-based data were obtained from the 1.3-m McGraw-Hill Telescope at the MDM observatory on Kitt Peak. The observations and reduction of this data is fully described in Falcón-Barroso et al. (in preparation). The HST imaging is not required to construct the dynamical models (see Section 2.9), however it provides an excellent photometric calibration and the improved resolution will allow these models to be used to determine black hole masses (though this aspect is not explored in this work).

Once the data had been obtained the next step was to match the two images

and then sky-subtract the resulting combined image. The HST images were used as reference for the photometric calibration and the MDM images were rescaled to the same level. To achieve this I measured the photometric profiles of the two images in logarithmically sampled circular apertures. There are three free parameters when matching the two profiles: the scaling ratio between the ground-based and HST image and the sky background levels of the two images. The sky level of the ground based image is easily obtained by requiring that at large radii the profile tends asymptotically to a power-law. The remaining two free parameters were fitted by minimising the error between the two profiles in the region of overlap (excluding the central 3 arcseconds to avoid seeing effects). This process is illustrated in Figure 2.1. The scaling parameters determined here were used later in the photometric modelling process where the two images are fit in parallel. At this stage I visually inspected the images to ensure that the data reduction process and the matching had been successful. I also identified any bright sources in the image other than the object of interest and masked these sources where necessary. Such sources included bright stars, other galaxies that appear close to the target galaxy on the sky and any artefacts in the image.

2.3.1 Dust correction

A small but none-the-less significant fraction of ETGs have significant dust content which can strongly affect their photometry. One example of this is NGC2685, known as the Helix galaxy because of the apparently helical dust features that strongly obscure one half of the galaxy. Other ETGs show central dust disks, prominent dust lanes and other, more irregular dust morphologies. In order to accurately model the photometry of these galaxies it is necessary to remove the effect of this internal dust extinction either by masking affected regions or, preferably, by 'correcting' the photometry for this internal extinction.

In order to correct for the effect of internal extinction I followed the method of

Carollo et al. (1997), further described in Cappellari et al. (2002). The dust is treated as a screen in front of the object, rather than assuming that the dust is distributed throughout the object. This technique relies on the differential extinction between two different photometric bands to estimate the total dust extinction and therefore the magnitude of any correction that needs to be applied to the original photometry.

I first identified any galaxies with significant dust extinction by inspecting r-band (or where available HST F814W) images by eye for each galaxy. Once the dust-affected sub-sample had been identified I flagged those galaxies where a second image in a bluer photometric band was not available and masked the dust affected regions in these objects. The choice of bands used to determine the correction varied based on two requirements: i) sufficient signal-to-noise in each image and ii) a wide as possible wavelength baseline to maximise the difference between the two images due to the dust extinction. Using the two images for each galaxy I created a colour map by subtracting the redder image from the bluer image (shown in the top left panel of Figure 2.2).

I then plotted the colour of each pixel in the colour map against the logarithm of its elliptical radius from the centre of the galaxy (shown in the top right panel of Figure 2.2). The galaxy centre (x_c, y_c), ellipticity (ϵ) and position angle (PA) were determined using the second moments of the luminosity distribution measured from the red image and at a radius within about 5 $\mathrm{R_e}$ for each galaxy. The elliptical radius is then given by:

$$\mathrm{r}_\epsilon = \sqrt{x'^2 + \frac{y'^2}{q^2}} \tag{2.1}$$

where:

$$x' = -(x - x_c)\sin\theta_{PA} + (y - y_c)\cos\theta_{PA} \tag{2.2}$$

$$y' = (y - y_c)\sin\theta_{PA} + (x - x_c)\cos\theta_{PA}. \tag{2.3}$$

This logarithmic observed colour profile was used to determine a smooth, 'model'

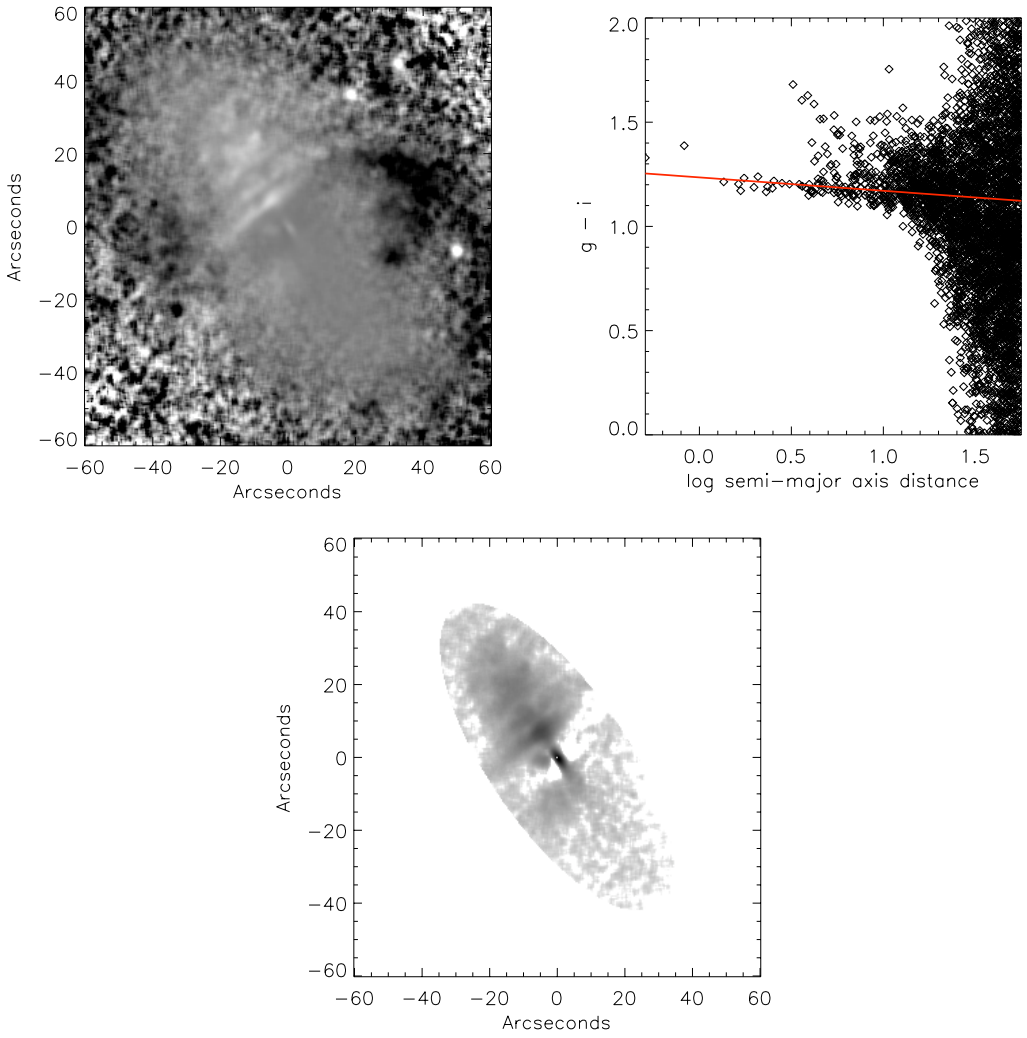

Figure 2.2: Upper left panel: *g-r* colour map of NGC2685. Dust is indicated by the white regions in the centre and upper left of the figure. Upper right panel: *g-r* vs. elliptical radius for all pixels. Red line indicates a fit to the data, showing the underlying galaxy colour profile. The outlying points at *(g-i)* ~ 1.5 and $\log d < 1.2$ are those affected by dust. Lower panel: pixels corrected for dust extinction based on their colour excess. Pixels greater than 50 arcseconds (in elliptical radius) from the centre of the galaxy were not corrected as the colour excess is dominated by noise at large radii.

colour profile by robustly fitting a straight line to the observed data, with the fit restricted to a radius covering only the high S/N region of the colour map (typically 1 to 3 R_e). Even in the dustiest galaxies the fraction of pixels affected by dust was < 20 per cent, allowing a good fit to the underlying colour profile to be determined. This smooth colour profile was transformed into a smooth model colour map using x_c, y_c, ϵ and the PA and was then subtracted from the observed colour map. This produced a map of the colour excess, E('blue' - 'red'). This colour excess is related to the extinction in a given band by the Galactic extinction law of Schlegel et al. (1998) and is given by:

$$A_V = 3.1E(B-V) \tag{2.4}$$

where A_V is the extinction (in magnitudes) in the V-band. This formalism can be applied to any pair of filters using the appropriate photometric transformation equations. For SDSS photometry these are given by Jester et al. (2005) and for HST WFPC2 photometry by Dolphin (2000). Using the colour excess map, the Galactic extinction law and the photometric transforms I computed the appropriate extinction correction to the observed photometry. This process was not always successful; the photometry for some galaxies was either too noisy or too strongly affected by dust to allow a reasonable model colour profile to be determined. In these cases the dusty regions were simply masked without being corrected for extinction. However, for the majority of galaxies, even in extremely dusty cases such as the previously mentioned NGC2685 the photometry was successfully corrected for internal extinction. An example of this is shown in Figure 2.3 with 'before' and 'after' images of the raw and extinction corrected photometry.

2.4 Multi Gaussian Expansion modelling

After treating the photometry as described above the next step is to find an analytic expression for the surface brightness profile of each galaxy to use as input for the

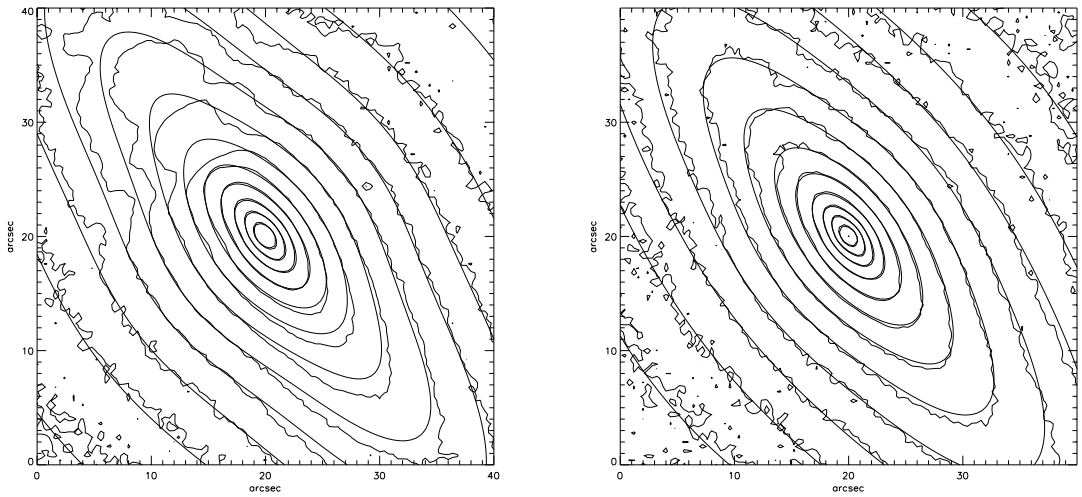

Figure 2.3: Photometry of NGC2685, the Helix Galaxy, with MGE models overplotted before (left panel) and after (right panel) dust correction, as described in the text. The effect of dust is visible as the band-like structure in the upper left of the galaxy; this structure is absent in the dust-corrected image.

dynamical modelling. An extremely flexible yet powerful formalism for doing this is the Multi Gaussian Expansion models of Emsellem et al. (1994), which describe the surface brightness profile of each object as the sum of two-dimensional Gaussians. This formalism can be used to accurately fit a wide variety of galaxy profiles and it also has the advantage that, being composed only of the sum of different Gaussian functions, it is easily integrable. While the MGE formalism is able to explicitly fit isophotal twists and other non-axisymmetric features by allowing each Gaussian component to have a different position angle (PA), I constrain my MGE models to be axisymmetric (constant PA). This allows the use of an axisymmetric dynamical modelling prescription. The physical motivation for this is discussed in Section 2.4.1. The surface brightness can then be described as:

$$\Sigma(x', y') = \sum_{j=0}^{N} G'_j = \sum_{j=0}^{N} \frac{L_j}{2\pi\sigma_j^2 q'_j} \exp\left\{-\frac{1}{2\sigma_j^2}\left(x_j'^2 + \frac{y_j'^2}{q_j'^2}\right)\right\} \tag{2.5}$$

where the model is composed of N Gaussian components of dispersion σ_j, axial ratio q_j and peak intensity I_j. The coordinates (x', y') are measured on the sky plane, with the x'-axis corresponding to the galaxy major axis. The total luminosity of each Gaussian component is given by $L_j = 2\pi I_j \sigma_j^2 q_j$. The MGE fitting method of Cappellari (2002) is used to facilitate fitting of the sample. The MGE model is convolved with the point spread function before matching to the observed photometry.The MGE models provide a good fit out to several R_e for the majority of objects. The photometry and corresponding MGE model for NGC4570 are shown in Figure 2.4. At this stage the match between the MGE model and the photometry was visually inspected to ensure a good match had been achieved. If the MGE contours clearly did not reproduce the photometry (despite having a nominally low χ^2 value), changes to the input parameters were made and the process iterated until a satisfactory fit was achieved.

Here I list some of the issues encountered during the MGE modelling:

- under-subtracting the sky causing the MGE model to fit very round Gaussians at large radii. This was addressed by improving the sky subtraction, or if a sufficiently accurate sky subtraction could not be determined by constraining the allowed axial ratio of the Gaussians to avoid small values.

- small ($\sim 1-2$ pixel) offsets between the galaxy centre and the model centre, typically due to small stars or dust features close to the centre of the galaxy. This was easily addressed by visually inspecting the MGE and photometric contours and adjusting the input parameters as necessary.

- small ($\sim 5^\circ$) misalignments between the model and true PA. The model PA was quite sensitive to the radius at which it was determined. Dust, nearby bright sources, non-axisymmetric features (see Section 2.4.1) and noisy pho-

tometry could also produce this issue. Again, this was easily addressed by visual inspection and manually adjusting the input parameters.

- overly round Gaussians being fit to the very centres (regions within 0.5 arcseconds of the centre of the object) of galaxies due to the PSF. In some cases this was easily addressed by constraining the allowed axial ratio of the Gaussians. If the galaxy had genuinely round isophotes at large radii (preventing the elimination of very round Gaussians from the MGE fit) then this issue was ignored as the effect on the inferred mass profile was negligible.

- more significant mismatches due to non-axisymmetric features (again see Section 2.4.1 for a full description of how non-axisymmetric features were dealt with).

2.4.1 Non-axisymmetric objects

As stated above the MGE models were constrained to be axisymmetric to allow the use of axisymmetric dynamical modelling techniques. The majority of ETGs are systems with high angular momentum dominated by disk-like rotation. These systems have smooth, virtually undisturbed morphologies and are easily reproduced with the axisymmetric MGE models described above. However, a substantial minority of systems have more complex morphologies that cannot be completely reproduced with axisymmetric models. These non-axisymmetric systems must be carefully dealt with in a way that allows us to extract reliable dynamical information without biasing the results.

ETGs exhibit three main types of non-axisymmetric structure: disturbed morphologies, bars and isophotal twists. Disturbed morphologies, such as tidal features, shells or strong asymmetries are generally indicative of a recent major merger. In this case the dynamical state of the galaxy is unlikely to be relaxed and the models are only a rough approximation of the true dynamical structure. If the disturbed

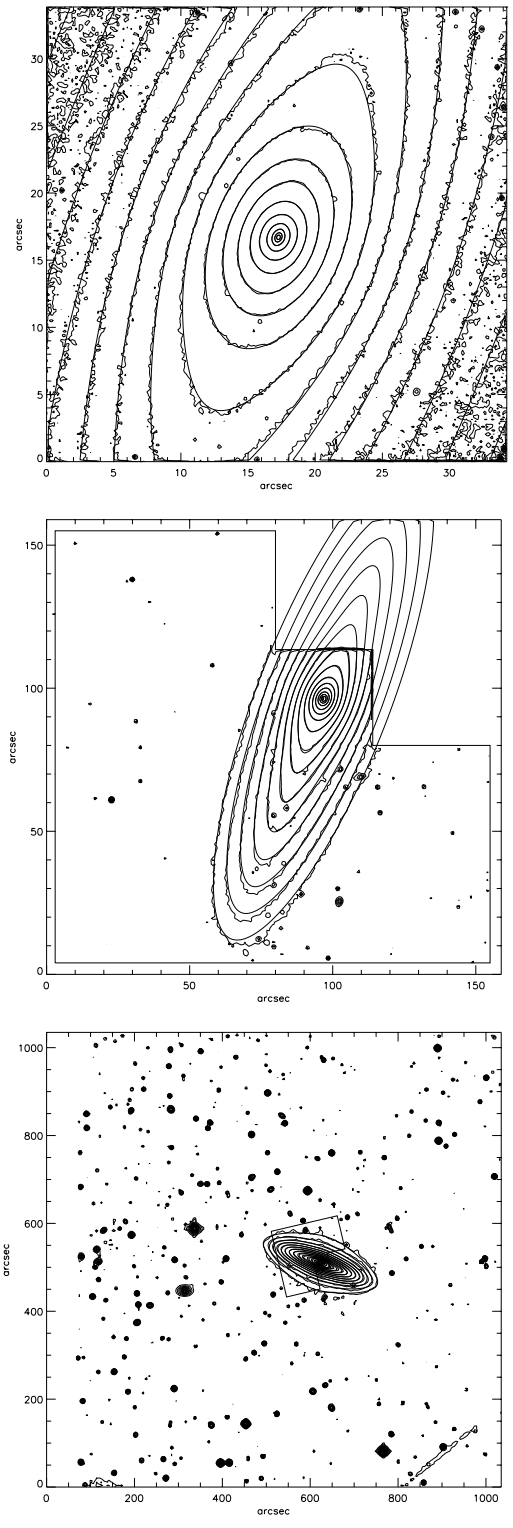

Figure 2.4: MGE model fit to the photometry of NGC4570. The photometry is shown as the rough contours with the MGE model as the smooth contours. Upper panel shows the PC1 image, middle panel the full the WFPC2 image and the lower panel the full extent of the ground-based MDM image with the relative position of the HST coverage indicated.

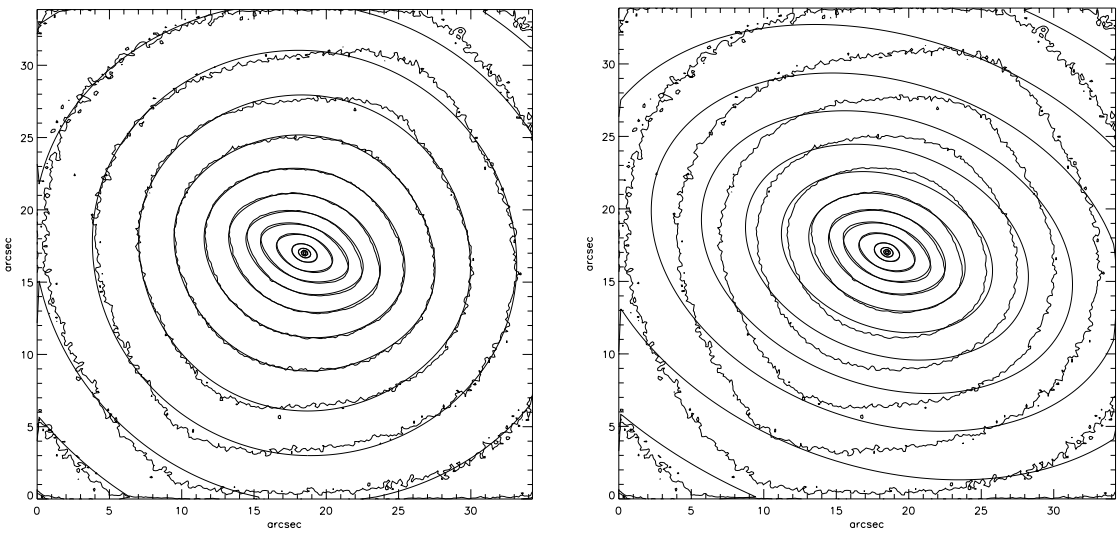

Figure 2.5: Two MGE model fits to the photometry of NGC3384 which has a prominent bar. The underlying photometry is the same in the two panels. The left panel shows an unconstrained MGE fit, the right panel an MGE fit constrained to match the axial ratios of the photometry both inside and outside the region where the bar dominates the light. In the left panel the model become much rounder than in the constrained model in order to fit the bar.

features are faint then the merger is likely to have occurred long enough ago that we can safely assume that the bulk of the galaxy (particularly the central region within 1 R_e where much of the mass is concentrated) is relaxed and model it as an axisymmetric object. This is generally the case for most passive, early-type galaxies.

The approach in the case of barred galaxies is somewhat different. A bar is clearly a non-axisymmetric feature and as such cannot be accurately reproduced by axisymmetric modelling. However the formation of a bar requires the presence of a disk, which is an axisymmetric structure. The majority of a galaxy's light comes from the disk rather than the bar and, assuming mass follows light, only a small fraction of a galaxy's mass is contained in the bar. Because of this I chose to treat bars as a first-order non-axisymmetric perturbation to the underlying zeroth-order axisymmetric structure of the disk. In practice this required tuning the MGE models to follow the underlying surface brightness profile of the disk rather than simply following the isophotes. This was achieved by constraining the axial ratio

of the Gaussians over the barred region of a galaxy to match that of the galaxy in regions both interior and exterior to those affected by the bar. This method worked well for the majority of barred galaxies, but in the case of extremely strong bars (systems which often also display a ring structure), where the fraction of the galaxy's mass in the bar is not small, this technique is less effective. Figure 2.5 illustrates the difference between an MGE that simply follows the galaxy isophotes and one which is constrained to ignore the bar.

The final case is galaxies which exhibit isophotal twists. Features of this nature are typically indicative of an underlying triaxial structure, though they can also result from merger activity. It is thought that all slow-rotating galaxies (which are typically the most massive early-type galaxies) have weakly triaxial structures (Binney, 1985; van den Bosch & van de Ven, 2009). Fortunately these triaxial galaxies are generally the most massive and roundest of ETGs, typically classified E0-E2, and hence any deviations from axisymmetry are generally small.

2.5 Integral field observations

Accurate modelling of the photometry is insufficient on its own to fully determine the gravitational potential of a nearby galaxy. In order to properly characterise the potential the MGE model must be deprojected, which requires that the inclination of the galaxy relative to the line of sight is known. The absolute scaling of the potential, which can be characterised by the mass-to-light ratio (M/L) of the galaxy, must also be determined. Finally, the shape of the galaxy must be constrained, which, under the assumption of axisymmetry described above, can be characterised as the 'flattening' or more technically the vertical anisotropy, β_z (which will be described in more detail in Sec. 2.6).

In order to constrain these parameters it is necessary to compare the predictions of the dynamical modelling to actual observations of the motions of the stars within

each galaxy. For all but the very nearest of galaxies one cannot observe the motions of individual stars. However, it is possible to infer the statistical properties of the motion of the stars, the mean radial velocity v_r', velocity dispersion σ_r' and higher order Gaussian moments from the integrated light of the galaxy. These quantities can be extracted from two dimensional spectroscopic observations carried out with an Integral Field Spectrograph (IFU).

I made use of the SAURON and ATLAS^{3D} surveys of nearby ETGs (described in Chapters 3 and 4 respectively) observed with the SAURON IFU. The reduction of this data and extraction of the kinematic parameters v and σ (as well as higher-order Gaussian moments) is fully described in de Zeeuw et al. (2002) and Emsellem et al. (2004), but I summarise it here for completeness.

SAURON is an IFU mounted on the William Herschel Telescope at the Roque de los Muchachos Observatoire on La Palma. SAURON is a lenselet-based IFU, using a grid of lenses to divide a two dimensional image on the sky into ~ 1400 spaxels and then dispersing the light from each spaxel into a spectrum. The instrument covers the wavelength range $4800 - 5200$ Å with ~ 4 Å FWHM spectral resolution (corresponding to an equivalent instrumental velocity dispersion of $\sigma_{\rm ins} = 108 {\rm kms}^{-1}$). It has a field-of-view of 30x40 arcseconds, with spatial resolution of 0.8 arcseconds. A detailed description of the instrument can be found in Bacon et al. (2001). SAURON data is reduced with the dedicated XSAURON pipeline (see de Zeeuw et al., 2002), involving bias subtraction, flat-fielding, wavelength calibration and sky subtraction. The reduced data forms a 'cube', with the x and y axis representing spatial position on the sky and the z axis representing wavelength.

Kinematic information was also extracted by the pipeline from the reduced data cubes. The data was initially spatially binned to a uniform signal-to-noise ratio (S/N) using the Voronoi binning technique of Cappellari & Copin (2003). The pipeline made use of the penalised PiXel Fitting (pPXF) technique of Cappellari & Emsellem (2004) to extract the stellar kinematics. The pPXF code first

constructed a best-fitting template spectrum from a library of stellar spectra (see Sánchez-Blázquez et al., 2006c, for details of the MILES library used for SAURON data). This template spectrum was then convolved with a line-of-sight velocity distribution (LOSVD) parameterised by the mean velocity v, velocity dispersion σ and higher order Gaussian moments h3 and h4. pPXF optimised the LOSVD to best match the observed spectrum in a given bin. This step was then repeated for each bin to determine the full set of kinematic parameters at all spatial positions within the SAURON field of view. This resulted in kinematic maps of v, σ and higher-order moments for each galaxy. See Chapter 5 for further discussion of kinematic extraction using pPXF.

2.6 Jeans Axisymmetric MGE (JAM) modelling

The Jeans Axisymmetric MGE (JAM) modelling procedure (Cappellari, 2008) takes the luminosity profile determined from the MGE modelling and the v and σ maps determined from the IFU observations as input and determines the full three-dimensional gravitational potential of the system. It does this by solving the Jeans equations (Jeans, 1922; Binney & Tremaine, 1987), which describe the evolution of the distribution function of the stars in terms of their positions and velocities, $f(x, y, z, v_x, v_y, v_z)$. In a steady state under the influence of a smooth gravitational potential the function $f(\mathbf{x}, \mathbf{v})$ must satisfy the collisionless Boltzmann equation:

$$\sum_{i=1}^{3} \left(v_i \frac{\partial f}{\partial x_i} - \frac{\partial \Phi}{\partial x_i} \frac{\partial f}{\partial v_i} \right) = 0 \tag{2.6}$$

where Φ is the gravitational potential.

However, the limited observational information we have available is not sufficient to fully constrain the solutions of this equation. The most common way to simplify this equation is to make the assumption of axial symmetry ($\partial\Phi/\partial\phi = \partial f/\partial\phi = 0$), which leads to the two Jeans equations:

$$\frac{\nu\overline{v_R^2} - \nu\overline{v_\phi^2}}{R} + \frac{\partial(\nu\overline{v_R^2})}{\partial R} + \frac{\partial(\nu\overline{v_R v_z})}{\partial z} = -\nu\frac{\partial\Phi}{\partial R} \tag{2.7}$$

$$\frac{\nu\overline{v_R v_z}}{R} + \frac{\partial(\nu\overline{v_z^2})}{\partial z} + \frac{\partial(\nu\overline{v_R v_z})}{\partial R} = -\nu\frac{\partial\Phi}{\partial z}, \tag{2.8}$$

where ν is the luminosity density and we use the notation:

$$\nu\overline{v_k v_j} = \int v_k v_j f d^3\mathbf{v}. \tag{2.9}$$

Further assumptions are still required to specify a unique solution. I made the observationally motivated assumptions (see Cappellari et al., 2006) that the velocity dispersion ellipsoid (specified by $\overline{v_R^2}, \overline{v_z^2}, \overline{v_R v_z}$) is aligned with the cylindrical coordinate system (R, z, ϕ) and that the vertical anisotropy is spatially constant and is parameterised by:

$$\overline{v_R^2} = b\overline{v_z^2} \tag{2.10}$$

where b parameterises the anisotropy. b is related to the classical anisotropy parameter, β_z by: $\beta_z = 1 - 1/b$. Under these assumptions the Jeans equations reduce to:

$$\frac{b\nu\overline{v_z^2} - \nu\overline{v_\phi^2}}{R} + \frac{\partial(b\nu\overline{v_z^2})}{\partial R} = -\nu\frac{\partial\Phi}{\partial R} \tag{2.11}$$

$$\frac{\partial(\nu\overline{v_z^2})}{\partial z} = -\nu\frac{\partial\Phi}{\partial z}. \tag{2.12}$$

The final assumption is that mass follows light, or equivalently that the M/L is constant. In this case the gravitational potential Φ is fully specified by deprojecting the surface brightness determined as described in Section 2.4.

The solution of the Jeans equations under these assumptions is fully described in Cappellari (2008). Here I outline the process while omitting most of the mathematical details. For a given inclination i, mass-to-light ratio M/L and total luminosity-

weighted anisotropy β_z, the MGE surface density distribution was deprojected, (from which the three-dimensional mass density distribution and hence Φ were obtained) and the Jeans equations were solved for $\overline{v_\phi^2}, \overline{v_z^2}$, which combine into a unique prediction for $\overline{v_{\rm los}^2}$. In order to determine the i, M/L and β_z that best described a given galaxy the model velocities were compared to the observed quantities. This required that the intrinsic quantities were first projected onto the sky plane and integrated along the line of sight. I defined a system of sky coordinates such that:

$$\begin{pmatrix} x \\ y \\ z \end{pmatrix} = \begin{pmatrix} 1 & 0 & 0 \\ 0 & -\cos i & \sin i \\ 0 & \sin i & \cos i \end{pmatrix} \begin{pmatrix} x' \\ y' \\ z' \end{pmatrix} \tag{2.13}$$

where (x, y, z) are the intrinsic galaxy coordinates and (x', y', z') are the sky coordinates. The z' axis lies along the line of sight and the x' axis is aligned with the galaxy major axis. The second moments of the velocity dispersion for a given Gaussian component are then given by Equation (26) of Cappellari (2008), and the total LOSVD is the sum of this quantity over all the Gaussians in the MGE model. The second moments of the velocity distribution, $\langle v_{los}^2 \rangle$ are a good approximation to the observed quantity, $V_{rms}^2 = V^2 + \sigma^2$, where V is the mean stellar velocity and σ the velocity dispersion determined from the SAURON observations.

To determine the best-fitting JAM model a series of models evenly sampling the i, M/L, β_z parameter space were constructed. For each model the second moments of the LOSVD were calculated as described above and compared to the observed V_{rms}^2 measured from the IFU observations (Section 2.5). The χ^2 parameter was computed for each model and then the model with the minimum χ^2 subject to the observationally motivated constraint that $\beta_z > 0$ was adopted (from Schwarzschild modelling of the SAURON sample, see Cappellari et al., 2007). Figure 2.6 shows a few examples of the observed first and second moments from SAURON and the corresponding best-fitting JAM moments.

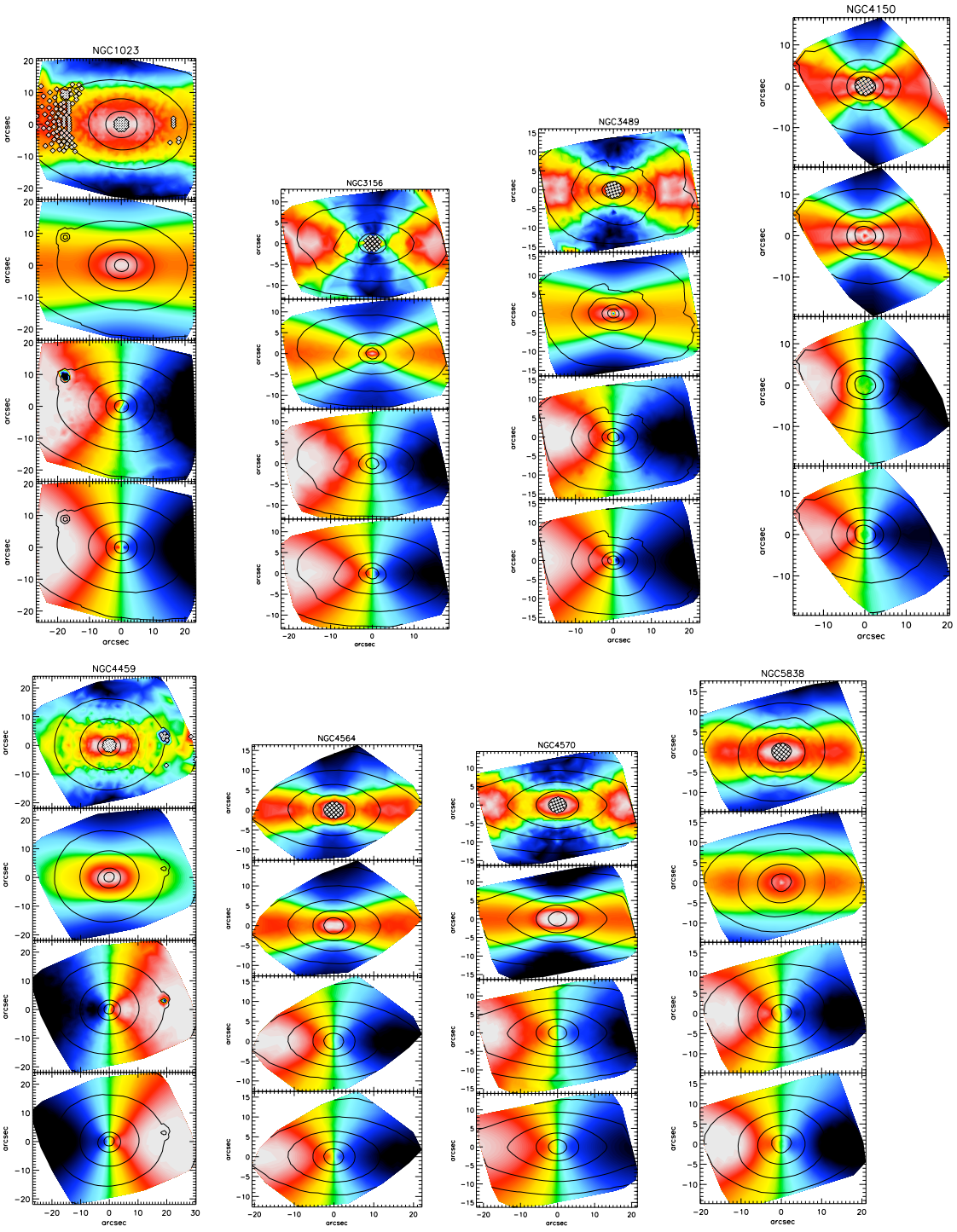

Figure 2.6: Examples of the JAM model fits to the observed SAURON kinematics. For each galaxy the panels show (top to bottom): the observed V^2_{rms}, the JAM model fit of the 2nd moments of the velocity distribution, the observed velocity field and the JAM prediction of the first moment of the velocity distribution. The JAM models are able to reproduce a wide variety of kinematic behaviour.

2.7 Determining the local escape velocity

Once the optimal gravitational potential Φ has been determined from the JAM model it is straightforward to determine the local escape velocity, V_{esc}. This quantity is simply related to Φ by the equation:

$$V_{esc} = \sqrt{2\Phi} \tag{2.14}$$

This returns the three dimensional distribution of V_{esc}, however the observed quantities I wish to compare V_{esc} to are only measured as integrated line-of-sight quantities. It was therefore necessary to project the three dimensional distribution of V_{esc} returned by the dynamical models onto the sky and integrate along each line of sight to produce a two dimensional map of V_{esc} before carrying out this comparison. The observed indices on the sky plane are the luminosity-weighted average of the local values in the galaxy along the line-of-sight. I made the quite general assumption that the indices are related to V_{esc} by a simple power-law relationship of the form:

$$\text{Index} \propto V_{esc}^{\gamma} \tag{2.15}$$

This leads to:

$$\begin{aligned} \Sigma(x', y')\text{Mgb} &\propto \Sigma(x', y')V_{esc}^{\gamma}(x', y') \\ &= \int_{-\infty}^{\infty} \rho(R, z)V_{esc}^{\gamma}(R, z)dz' \\ &= \int_{-\infty}^{\infty} \rho(R, z)|2\Phi(R, z)|^{\gamma/2}dz' \end{aligned} \tag{2.16}$$

With this assumption it is possible to extract the luminosity-weighted average of the local V_{esc} along the line-of-sight. In practice the V_{esc} values depend only weakly on the parameter γ and our conclusions hold for any reasonable choice of the parameter.

2.8 Dark matter and the assumption of constant M/L

The JAM modelling described in this chapter assumes a constant M/L for each galaxy. An alternative way of thinking of this assumption is that the models assume that the mass distribution within each galaxy follows the light distribution. This assumption is clearly not accurate for real galaxies, were the stars are embedded in dark matter halos that are significantly more extended than the luminous matter. Evidence from galaxy dynamics, X-ray halos and strong and weak lensing (Evrard et al., 1996; Gerhard et al., 2001; Refregier, 2003; Lewis et al., 2003; Koopmans et al., 2006) all suggest that the mass of a typical galaxy at large radius is much higher than the light alone would suggest, and that this contribution varies with radius. Because of this the JAM models may not accurately constrain the absolute value of the gravitational potential, Φ.

However all hope is not lost. The central regions of ETGs are dominated by luminous matter. Evidence from dynamical studies (see for example Côté et al., 2003; Weijmans et al., 2009) suggests that luminous matter dominates out to 3-5 Re, with dark matter contributing only 30 - 50 per cent within this region. The assumption that the mass distribution follows the light distribution is reasonable *over this region*. Because of this the models constrain well the difference in the depth of the potential well, $\Delta\Phi$ ($\propto \Delta V_{esc}^2$), between different regions of the same galaxy, over the region where the luminous matter dominates. It is less clear how well the models constrain the absolute value of the potential, hence the difference in Φ between different galaxies.

To investigate this effect I examined a simple model of a galaxy with a dark halo. This model assumes that the stellar mass distribution follows a Hernquist

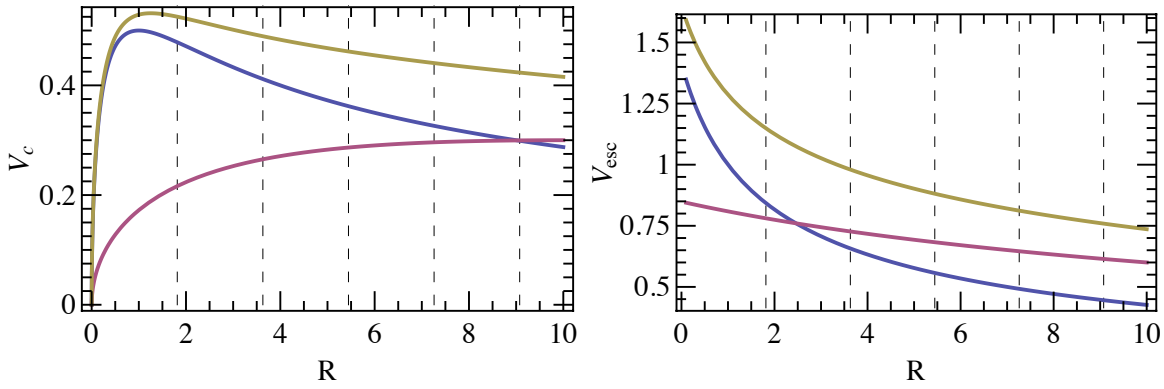

Figure 2.7: Circular velocity (left panel) and escape velocity (right panel) as a function of radius. The yellow line indicates the total value while the red and blue lines indicate the contributions due to dark and stellar mass respectively. The dashed vertical lines show the positions of 1, 2, 3, 4, and 5 R_e. The change in the gradient of V_{esc} between total and stellar contribution only over the region 0-1 R_e is 0.07 dex.

profile with scale radius $a = 1$ (Hernquist, 1990) given by:

$$\rho(r) = \frac{M}{2\pi}\frac{a}{r}\frac{1}{(r+a)^3} \tag{2.17}$$

The stellar distribution is then embedded in a dark matter halo also represented by a Hernquist profile but with $a = 10$. The Hernquist profile is similar to the more standard NFW profile of Navarro et al. (1996), however it has finite total mass. The mass of the stellar and dark matter distributions were scaled such that the dark halo contributed only 50 per cent of the mass within 5 R_e, consistent with observations (Weijmans et al., 2008). The V_{esc} calculated from this combined model (and the contribution of the luminous and dark components) is shown in Figure 2.7.

In the DM halo model the V_{esc} gradient within 1 R_e decreased by 0.07 dex, compared to the V_{esc} profile due to the luminous component only. This is only a small change in comparison to the error on the V_{esc} measurements, and so does not significantly affect the conclusions drawn later in this work. The variation in the absolute value of V_{esc} may be more significant, and it is important to bear this caveat in mind when evaluating the results discussed in the following two chapters.

The inclusion of a dark halo can cause the true value of V_{esc} to differ from the JAM model value by a constant offset within a single galaxy. This constant may vary on a galaxy-to-galaxy basis, due to dark halo properties that differ systematically as a function of, for example, galaxy mass. As an aside, it may be possible to use studies of this nature to constrain the variation of dark halo properties, however I do not explore this possibility in this work.

In an upcoming work Cappellari et al. (in preparation) will investigate the effect of including a cosmologically motivated dark halo component in the JAM models. Initial results confirm that the centres of luminous ETGs are dominated by luminous matter (with typical DM fractions within 1 R_e of 10-15 per cent) and that the offset in V_{esc} from models assuming constant M/L is small relative to the absolute values of V_{esc}, but is comparable to the measurement error on V_{esc} discussed above. This offset may contribute significantly to the observed scatter in the results discussed in the following two chapters, though I do not quantify this effect in this work.

2.9 Applying the process to large samples of galaxies

While the method described above is effective in determining the local gravitational potential in individual or small samples of galaxies, the amount of work required to fully model a large sample of galaxies in this way is prohibitively time consuming. To facilitate the dynamical modelling of large samples of galaxies I automated several of the more work-intensive stages in the process described above. Rather than describe the entire automated modelling process in full I will focus here only on the differences between the process described above and the improved, automated technique. The key differences are: use of SDSS *r*-band imaging (or equivalent outside the SDSS coverage), automatic optimisation of the axial ratios of the MGEs and automatically selecting the best fitting JAM model. I describe the first two improvements in detail

below.

HST coverage of ETGs in the nearby Universe is far from complete, particularly if one focuses on a single instrument or band. Wide-field ground-based photometric surveys such as the Sloan Digital Sky Survey (Abazajian et al., 2009) have much more complete coverage of the sky and more importantly the imaging type is of a consistent quality, band and depth. With uniform imaging data it is much easier to automate the MGE modelling process - there is no longer a need to match the photometric zeropoints and astrometry of multiple images. Additionally, the SDSS *ugriz* filter set is available at other facilities, allowing us to easily fill in holes in the SDSS coverage. While the SDSS imaging lacks the high spatial resolution of HST data (the SDSS resolution is 0.4 arcseconds with typical seeing ~ 1 arcsecond) and more importantly the depth of the MDM photometry, my tests showed that MGEs produced from SDSS (or equivalent) data alone were consistent with HST+MDM based MGEs within the errors. Figure. 2.8 shows the central regions of NGC3379, with MGEs from SDSS and HST+MDM data overlayed for comparison. In Figure 2.9 I show a more quantitative comparison of the two sets of MGEs, directly comparing the total r-band magnitude $\mathrm{M_r}$ and effective radius $\mathrm{R_e}$ measured from the MGEs. The SAURON MGEs were converted to r-band using the photometric transformation equations of Jester et al. (2005). The total magnitudes determined from the two sets of MGEs are consistent within the errors; the rms residuals from a 1:1 relation are 0.2 mags. For galaxies with $\mathrm{R}_e < 25$ arcsecs the R_es are also consistent, however for larger galaxies the R_es determined from the SAURON MGEs are consistently larger. This is likely due to the SDSS photometry being shallower than the MDM photometry.

The most important step in automating the dynamical modelling process was the optimisation of the choice of allowed axial ratios in the MGE models. For a typical ETG with featureless structure the MGE code selects an appropriate range of axial ratios without any user intervention. However, as described in Section

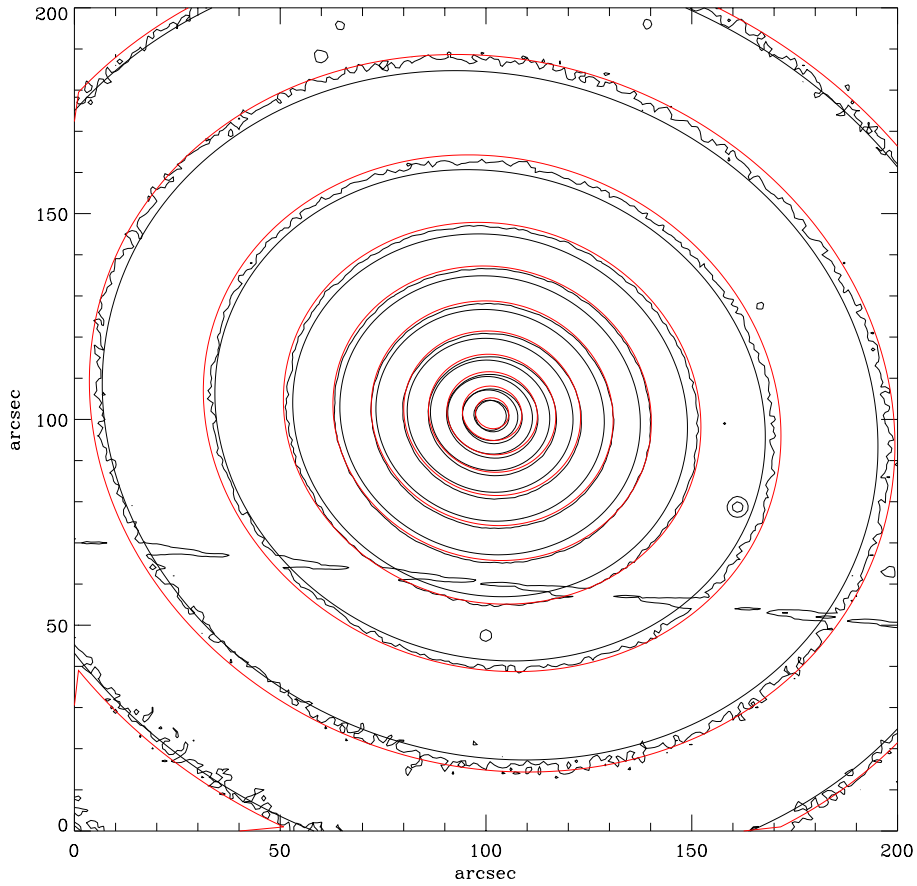

Figure 2.8: SDSS r-band photometry of the inner regions of NGC3379. The MGE determined from the HST+MDM data is overplotted in red and the MGE from SDSS data only is overplotted in black.

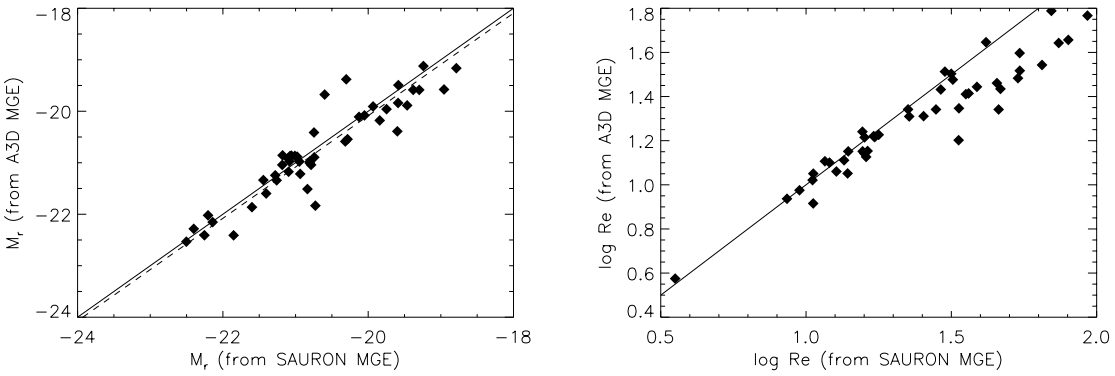

Figure 2.9: Comparison of the MGEs produced for the SAURON survey and the ATLAS^{3D} survey for the 47 galaxies in common between the two samples. Left panel: M_r from the SDSS MGE vs. that from the HST+MDM MGE. Right panel: R_e for the same data. Solid line shows a 1:1 relationship. Dashed line is a fit to the data. The magnitudes from the two MGEs are consistent within the errors. At small R_e the radii are consistent, however at large radii the SAURON MGEs yield R_es $\sim$ 30 per cent larger than the ATLAS^{3D} R_es. This is likely due to the deeper photometry used in the SAURON survey.

2.4.1, non-axisymmetric features complicate this process and q_{min} and q_{max} have to be manually constrained. Instead of this labour-intensive, trial-and-error process I implemented an iterative process of gradually restricting the range of allowed axial ratios. Initially q_{min} is raised from 0.05 in small steps until the χ^2 value of the resulting MGE model is 5 per cent larger than that of the previous iteration. Once the optimal q_{min} is determined the same procedure is repeated with q_{max}, decreasing from 1.0. Again, the optimal value for q_{max} is determined by stopping the iteration either when $q_{max} = q_{min}$ or when the χ^2 of the new MGE model in 10 per cent larger than the previous iteration. I found that a slightly larger tolerance was required for q_{max} than for q_{min} to avoid producing overly round galaxies. A step size in q of 0.05 was necessary for the resulting JAM models to accurately reproduce the inclinations of those galaxies where an independent determination of inclination was available (e.g. dust disks or clearly edge-on galaxies).

Chapter 3

Correlations of observational parameters with the local escape velocity

3.1 Overview

In this section I will describe the role the local escape velocity, V_{esc}, plays in low-redshift ETGs. I will begin by describing how I compare V_{esc} with other galaxy properties, as both globally averaged quantities and as local quantities measured at different positions within each galaxy. I will then describe the relationship between V_{esc} and directly observable quantities such as colours and line strength indices. Finally I will describe the use of Single Stellar Population (SSP) models to determine the more physically motivated SSP parameters: age, metallicity and alpha-enhancement and how these correlate with V_{esc}.

3.2 The SAURON sample

In Chapter 2 I described the SAURON IFU observations of the SAURON and ATLAS^{3D} samples, but avoided any discussion of the samples themselves. In this section I will describe the SAURON ETG sample which is used for all the analysis in this chapter. In Chapter 4 I describe the volume limited ATLAS^{3D} sample.

The SAURON sample was selected to give an overview of the local early-type population (Es, S0s and also Sa early-type spirals) - it is *representative* but not *complete*. The parent sample, from which the SAURON ETG sample was selected, was initially derived by considering all galaxies for which SAURON could measure stellar kinematics. This led to the following constraints:

- $-6^\circ \leq \delta \leq 64^\circ$
- $cz \leq 3000\text{kms}^{-1}$
- $M_B \leq -18$ magnitudes
- $|b| \geq 15^\circ$

The declination constraints arise from the latitude and pointing constraints of the WHT itself. The sample must lie more than 15° from the Galactic plane in order to avoid crowded fields and large Galactic extinctions. The requirement that all principal lines of interest fall within the SAURON wavelength coverage limits the sample to redshifts $cz \leq 3000\text{kms}^{-1}$. Finally, because of the instrumental spectral resolution, SAURON can only measure velocity dispersions $\sigma \geq 75\text{kms}^{-1}$, which corresponds approximately to a B-band magnitude of -18.

This sample was then subdivided by morphology and environment into elliptical (E), lenticular (S0) and early-type spiral (Sa) galaxies and cluster and field galaxies. Morphologies and the other galaxy parameters listed above were taken from the Lyon/Meudon Extragalactic DAtabase (LEDA, see Paturel et al., 2003). E and S0

galaxies were selected based on the LEDA morphological T-type (E: $T \leq -3.0$, S0: $-3.0 < T \leq -0.5$, Sa: $-0.5 < T \leq 1.5$).

A sample was selected by uniformly populating the luminosity-ellipticity plane within each of these six categories (E/S0/Sa and cluster/field). The ellipticity range is divided into bins of 0.2 and the luminosity range into bins of 1 magnitude between $M_B = -18$ to $M_B = -22$. From these criteria a final sample of 72 galaxies was selected, 36 'cluster' galaxies (12 E, 12 S0 and 12 Sa) and 36 'field' galaxies (12 E, 12 S0, 12 Sa). In this work I focus only on the ETGs (E and S0), giving a final sample of 48 nearby ETGs. For full details of the sample see de Zeeuw et al. (2002).

The kinematic measurements obtained from the SAURON IFU were described in the previous chapter in Section 2.5. As well as kinematic information these observations also yield information on the stellar population content of these galaxies. The SAURON spectral range covers three important spectral absorption features: Hβ, Fe5015 and Mgb at 4856, 5015 and 5176 Å respectively. The measurement of these absorption features is defined under the Lick/IDS system by Worthey et al. (1994). Spectral absorption features are closely related to the stellar population properties of ETGs, though that relationship is complex and will be discussed further in Section 3.5. As with the kinematic measurements, the absorption line strength measurements are presented as a map, giving the integrated line-of-sight line strength at a given spatial position within the galaxy on the sky. As well as the IFU observations the entire SAURON sample was observed with the 1.2m telescope at the Kitt Peak MDM observatory to provide wide-field F555W and F814W-band photometry. Additionally, all but one of the SAURON galaxies have archival HST imaging available.

3.3 Measuring profiles

In order to study the correlation between the local V_{esc} and other local galaxy properties those properties must be extracted over some common region and in a consistent fashion. The straightforward choice would be to compare parameters on a bin-by-bin basis, directly comparing the same physical positions within a galaxy. This works well for comparing the local V_{esc} with quantities computed directly from the SAURON data, as these quantities are computed from the same spatial bins. However, this scheme becomes problematic when considering non-SAURON derived quantities (such as the local colour), as defining identical apertures is complex. Additionally, the single-bin values can be affected by poor data quality or problems with the spectral fitting and so an average quantity computed within a larger aperture is desirable to minimise the effect of outlying values.

Because of these considerations I opted to evaluate all the quantities within radial annular apertures. In the SAURON sample I used a series of elliptical annuli, growing linearly in radius in steps of 1 arcsecond. The PA and ellipticity of each aperture was fixed to the global PA and ellipticity of the galaxy determined as described in the previous chapter. For all galaxies the central 2 arcseconds were excluded to avoid seeing effects and any emission from active galactic nuclei (AGN). The radius of the outer annulus was chosen to be the last aperture that encompassed at least 3 independent datapoints.

Profiles of all the quantities considered in the following section were formed by determining the median luminosity-weighted value measured within the elliptical apertures described above. The error on each data point is given by the quadratic sum of the mean measurement errors (determined as described in Kuntschner et al., 2006) and the rms scatter within the aperture:

$$\sigma_{\mathrm{Total}} = \sqrt{\sigma^2_{\mathrm{Aper}} + \sigma^2_{\mathrm{Meas}}} \tag{3.1}$$

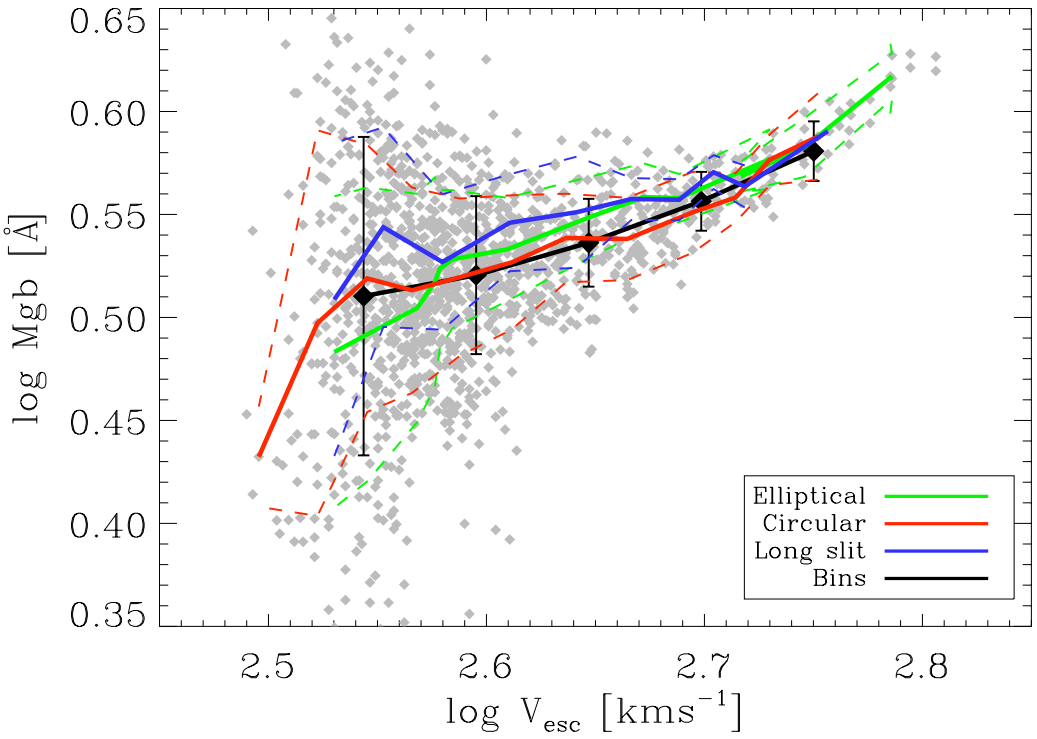

Figure 3.1: Comparison of Mgb-V_{esc} profiles measured in circular, elliptical and long slit apertures and for individual bins for NGC2549. The green line shows the elliptical aperture measurements, the red line circular apertures and the blue line a long slit along the major axis. The dashed lines show the corresponding 1-σ error envelope. The grey points show the individual bins. The black line shows the binned mean of these points and the error bars the scatter within each bin.

I found that matching the ellipticity of the extraction apertures to the global ellipticity minimised the rms scatter within an annulus and hence the total error on each data point.

3.3.1 Tests of profile robustness

In order to test the robustness of the profiles determined above I considered the effect of a series of different apertures on the measured profiles. I considered the extreme cases of purely circular apertures and longslit apertures aligned along the major axis, as these cases represent typical choices for previous studies of this kind. I also considered a direct bin-by-bin comparison. Circular apertures were chosen with

the same radii as the major axis of the elliptical apertures. The longslit aperture was chosen to have a width of 4 arcseconds, and radial divisions the same as the elliptical case. As above, the central 2 arcseconds was excluded and apertures were accreted until insufficient independent data points were available. The bin-by-bin comparison shows all points within the SAURON field of view, outside the central 2 arcseconds.

The results of this comparison for NGC2549 are shown in Figure 3.1. The solid red, green and blue lines show the profiles for the three choices of aperture; elliptical, circular and longslit respectively, with the 1-σ error envelope shown for each profile. The grey points show the individual bins, with the solid black line showing the running average of these points and the associated 1-σ errors. As can be seen the profile varies little between the four cases, the main difference being a variation in the size of the error. In the longslit case the large errors are due to only a limited number of datapoints contributing to the profile. In all cases the increasing errors at large radii (low V_{esc}) are due to decreased S/N in the raw data.

3.4 The Index-V_{esc} relations

I applied the technique described above to form profiles from the observed line strength maps of Mgb, Hβ and Fe5015 as well as the V_{esc} maps determined from the dynamical modelling described in the previous chapter. The results of this analysis for the SAURON sample are shown in Figure 3.2.

Each colour and symbol combination represents the profile for an individual galaxy. Each point within a single galaxy's profile indicates the values measured within a specific elliptical annulus. Galaxy centres lie towards the right of the plot as these are the regions with the highest V_{esc}. Mgb and Fe5015 are positively correlated with V_{esc}, while Hβ is negatively correlated. In all three cases the scatter increases significantly at lower values of V_{esc} (this phenomenoon will be discussed

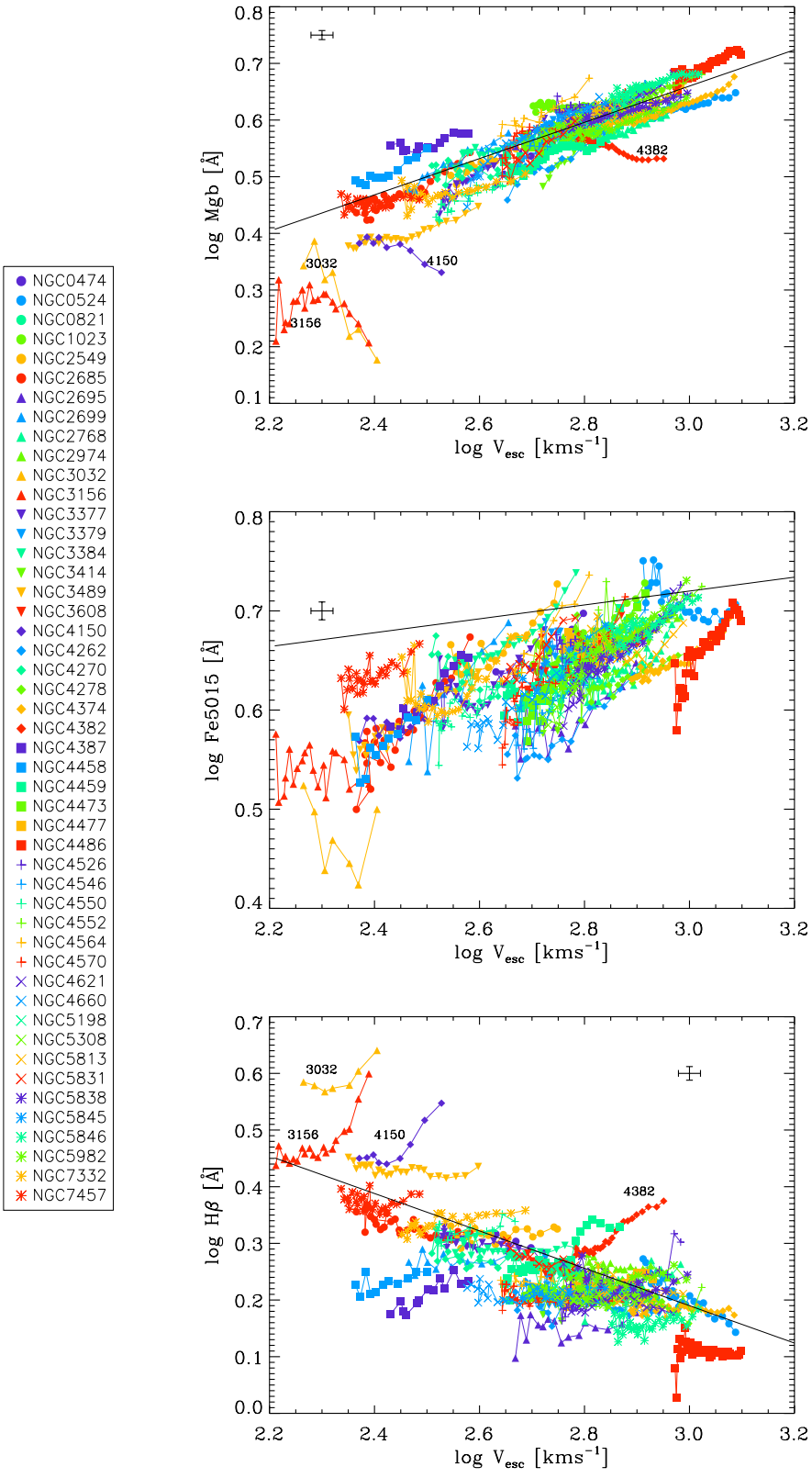

Figure 3.2: The Index-V_{esc} relations for the SAURON ETG sample. Each colour-symbol combination indicates a different galaxy profile. Galaxy centres lie to the right as these are the regions of the highest V_{esc}. The solid black lines show a fit to the central aperture relations.

further in the next chapter), though the relations are still present.

The solid black line in each figure shows the best fit to the 'global' relation determined from the values measured within $R_e/8$ circular apertures. These lines are determined by a robust linear least absolute deviation fit to the logarithm of the data points. The four outlying galaxies, labeled with their NGC numbers in the upper panel of Figure 3.2 were excluded from the fit. I identify these galaxies as outliers because their profiles exhibit qualitatively different behaviour to the other 44 galaxies - they show central dips in Mgb whereas the bulk of galaxies have profiles that smoothly increase with V_{esc}. The fit has the form: $\log \mathrm{Index} = a + b \log V_{esc}$:

$$\log \mathrm{Mgb} = (0.32 \pm 0.03) \log V_{esc} - (0.30 \pm 0.09); \sigma = 0.033 \tag{3.2}$$

$$\log \mathrm{Fe5105} = (0.07 \pm 0.03) \log V_{esc} + (0.51 \pm 0.09); \sigma = 0.033 \tag{3.3}$$

$$\log \mathrm{H}\beta = (-0.33 \pm 0.05) \log V_{esc} + (1.18 \pm 0.15); \sigma = 0.049 \tag{3.4}$$

Fitting to all the data from the profiles using the same fitting technique (again excluding the same four galaxies) gives the following values:

$$\log \mathrm{Mgb} = (0.35 \pm 0.01) \log V_{esc} - (0.41 \pm 0.03); \sigma = 0.027 \tag{3.5}$$

$$\log \mathrm{Fe5105} = (0.18 \pm 0.01) \log V_{esc} + (0.62 \pm 0.02); \sigma = 0.029 \tag{3.6}$$

$$\log \mathrm{H}\beta = (-0.21 \pm 0.01) \log V_{esc} + (0.82 \pm 0.02); \sigma = 0.040 \tag{3.7}$$

3.4.1 Scatter

All three Index-V_{esc} relations are tight, with scatter on the order of 5 per cent. The Mgb-V_{esc} relation is the tightest of the three, particularly at high values of V_{esc}. To understand how significant this tight scatter is as a constraint on galaxy evolution models it is important to compare to other similar relations, both from the SAURON

data itself and from the literature.

The obvious initial comparison is to the Index-σ relations from the SAURON data itself. Following the same method as described above I constructed Index-σ profiles for all 48 galaxies in the SAURON sample. Fitting to the Re/8 aperture values yields observed 1-σ dispersions of 0.028, 0.030 and 0.046 for the Mgb-, Fe5015- and Hβ-σ relations respectively. Fitting to all points in the profiles gives observed 1-σ dispersions of 0.033, 0.031 and 0.042. The values for the relations between galaxy centres only are very similar to those from the Index-V_{esc} relations; when considering galaxy centres only the V_{esc} and σ relations are equally as tight. However, when taking into account the behaviour within individual galaxies by fitting to the galaxy profiles, the scatter in the Mgb-σ relation increases over that in the V_{esc} relations.

The Mgb-σ relation between galaxy centres has been studied by several different groups in large samples of galaxies. To compare the scatter in the Mgb-V_{esc} relation to these literature values it was first necessary to move from measuring the observed scatter in the relation to determining the intrinsic scatter in the relation, i.e. the expected scatter after measurement errors are taken into account. To do this I performed fits to each of the observed correlations by minimising the χ^2 parameter using the FITEXY routine taken from the IDL[1] Astro-Library (Landsman, 1993), which is based on a similar routine by Press et al. (1992) and adding quadratically the intrinsic scatter to make $\chi^2/\nu = 1$, where ν is the number of degrees of freedom. For a discussion of the technique and its merits see Tremaine et al. (2002). Using this method I found an intrinsic scatter in the Mgb-V_{esc} relation determined from Re/8 aperture values of 4.1 per cent, rising to 5.6 per cent when including the entire profile for each galaxy. Colless et al. (1999) found an intrinsic scatter of 9 per cent in a sample of 490 ETGs. In a sample of 72 ETGs Kuntschner et al. (2001) found an intrinsic scatter of 7 per cent and in a sample of 98 ETGs Sánchez-Blázquez et al. (2006b) found an intrinsic scatter of 6 per cent. The scatter in the Mgb-V_{esc}

[1] http://www.ittvis.com/ProductServices/IDL.aspx

relation, both locally and globally is comparable to that in Mgb-σ relations from the literature between central values only.

It is also interesting to compare other relations connecting the stellar population properties of ETGs to their dynamical properties such as the red sequence of the colour-magnitude diagram. Bower et al. (1992) find an intrinsic scatter of 1.5 per cent in the colour-magnitude relation for a sample of Virgo and Coma cluster ETGs. Tremonti et al. (2004) use a sample of 51,000 galaxies to study the mass-metallicity relation and find an intrinsic scatter of approximately 4 per cent. Both these relations are based on measurements relating a global aperture measurement (mass and total magnitude) to a central aperture measurement (metallicity and colour). The Mgb-V_{esc} relation determined globally is comparable to these other relations as a constraint on galaxy evolution models, but it has the added benefit of also providing information on the internal behaviour of galaxies.

3.4.2 Comparison with previous results

The number of studies that have looked at the local Mg-σ and Mg-V_{esc} relations is surprisingly small given the well known tightness of the global relation. The two main studies in the area are Davies et al. (1993, hereafter DSP93) and Carollo & Danziger (1994, hereafter CD94). Both have much smaller samples than this work (8 galaxies and 5 galaxies with V_{esc} respectively). The DSP93 sample has four galaxies in common with the SAURON sample (NGC 3379, 4278, 4374 and 4486) for three of which DSP93 have determined V_{esc} (the exception is NGC 4374) whereas there are no galaxies in common with the CD94 sample. Both DSP93 and CD94 looked at the Mg_2-V_{esc} relation, rather than Mgb-V_{esc} relation. Mg_2 is a broader molecular index but is tightly correlated with the Mgb index. I converted their Mg_2 index values to Mgb using the relation from Jorgensen (1997):

$$\log \text{Mgb} \;=\; 1.57\ \text{Mg}_2 + 0.208 \tag{3.8}$$

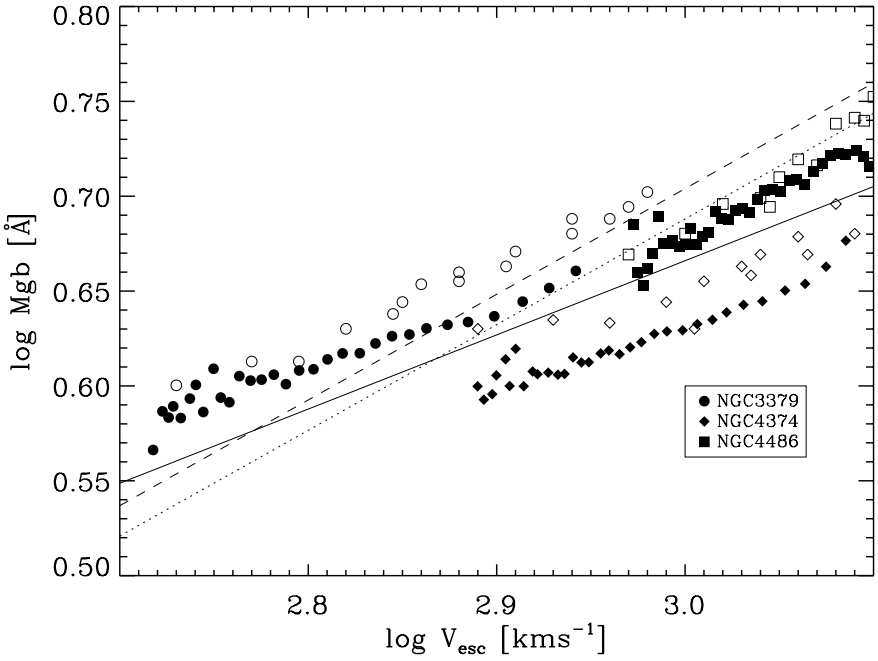

Figure 3.3: Comparison of the results of our sample with those galaxies we have in common with DSP93. The Mg_2 index values of DSP93 and CD94 were converted to Mgb index values using Equation 3.8. The open symbols are the values from DSP93 and the closed symbols are the results from this work. The solid line is the fit to the SAURON sample, the dotted line to the DSP93 sample and the dashed line the CD94 sample.

DSP93 and CD94 are also based upon long-slit spectroscopy rather than integral-field data. In order to fairly compare our data to the previous work I re-extracted the V_{esc}, σ and Mgb profiles using a rectangular aperture 2.5 arcseconds wide, (as used in the DSP93 observations) aligned with the major axis of the SAURON maps, and sampling linearly in distance along the slit from the centre of each galaxy.

For the three galaxies in common with the DSP93 sample I found reasonable agreement with my Mgb-V_{esc} result (see Figure 3.3). While the individual measurements are in broad agreement the slope for my sample is significantly different to that found by DSP93 and CD94. The larger range is V_{esc} covered by the SAURON sample provides a more accurate determination of this slope, despite similar measurement errors on the individual data points.

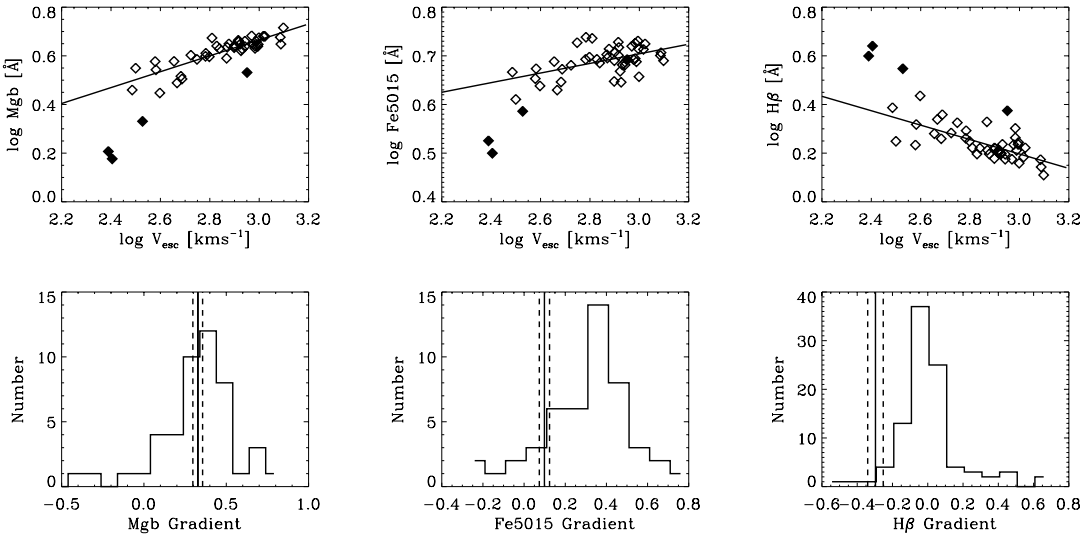

Figure 3.4: Upper row: Central ($R_e/8$) aperture measurements for the Index-V_{esc} relations. The four outlying galaxies are indicated in black. The solid line in each upper panel is a fit to the central aperture measurements excluding the outlying galaxies. Lower row: histogram of the individual galaxy gradients (determined from linear fits to each galaxy profile) for each index. The vertical solid and dashed lines show the global gradient and the 1-σ bounds on the global gradient respectively. For the Mgb-V_{esc} relation the distribution of galaxy gradients is consistent with the global gradient. For the Fe5015 and Hβ relations the distribution of individual galaxy gradients is significantly offset from the global relation.

3.4.3 Gradients

As discussed above the scatter in the Index-V_{esc} relations is comparable to that in the more widely used Index-σ relations, so why go to all the additional effort required to determine V_{esc} if it doesn't improve the results? The new insight comes from the behaviour of the relations within an individual galaxy, compared to this global behaviour. To study this behaviour I first performed a linear fit to each of the individual galaxy gradients, using the same fitting technique described above. To simplify the comparison I considered only the gradients and zero points determined for each individual galaxy. I then compared the distribution of individual galaxy gradients with the global gradient determined from the central values. This comparison is shown in Figure 3.4.

I found that in the case of the Mgb-V_{esc} relation the distribution of the local

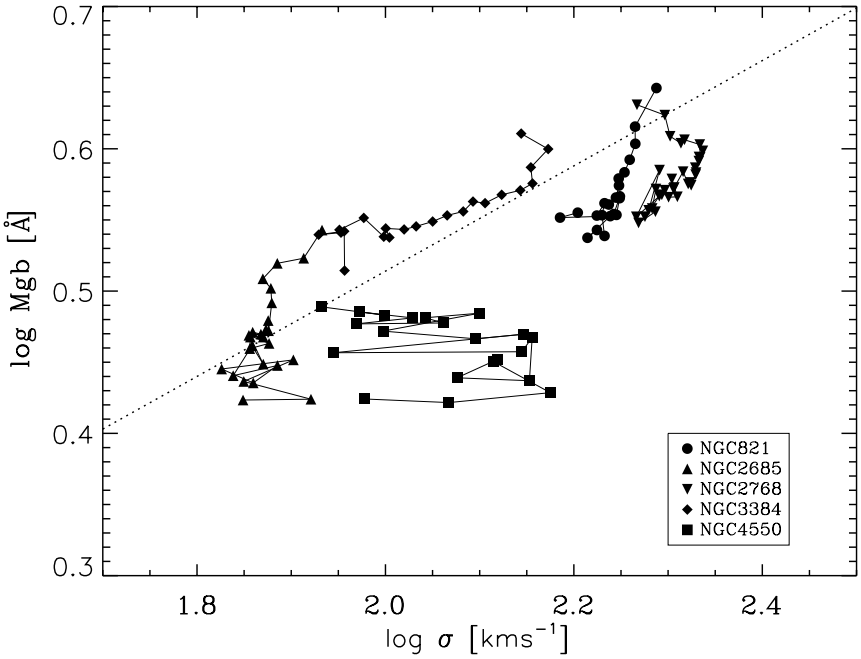

Figure 3.5: Mgb-σ profiles for a subset of the SAURON sample. While some galaxies are consistent with the global relation (the dotted line) many galaxies show complex, non-linear profiles. In many cases the gradient of the Mgb-σ profile has little physical meaning (see Figure 3.3 for comparison).

gradients is consistent with the global value. The relation between different galaxies is the same as that within individual galaxies. The Mgb-V_{esc} relation applies *both locally and globally*. The distribution of local gradients has the same mean as the global value. The distribution of local gradients is much broader; the typical error on the individual galaxy gradients is 0.04 and the width of the distribution is 0.2, implying an intrinsic scatter of 0.15. In contrast the error on the global gradient is only 0.03.

In the case of the Fe5015-V_{esc} relation the distribution of the local gradients is offset from the global gradient - the relation within individual galaxies is different to that between different galaxies. The individual galaxy gradients are typically steeper than the global gradient. The Hβ-V_{esc} gradients are typically flatter than the global relation - the distribution of individual galaxy gradients is consistent with a flat mean gradient.

The local and global behaviour shown by the Mgb-V_{esc} relation is the principal improvement over the Mgb-σ relation. Because of the complex behaviour in the σ profiles talking about an Mgb-σ gradient in the same way as an Mgb-V_{esc} gradient makes little sense (see Figure 3.5 for a few examples). The other advantage of V_{esc} over σ (as more fully discussed in Chapter 4) is that it is a direct measure of the local gravitational potential rather than a proxy (as σ is) and so should be more closely connected to the physical processes occurring in these galaxies.

While I found a tight relation between Mgb and V_{esc} both within individual galaxies and between different galaxies it is not obvious how to physically interpret this relation. While absorption line strength indices are closely related to the star formation history and stellar population properties of galaxies, those relations are complex. In Section 3.5 I use SSP models to convert the line strength index measurements into physical single stellar population equivalent parameters, which are, in principal, easier to interpret.

3.4.4 The Index-V_{esc} hyperplane

While the Mgb-V_{esc} relation has low scatter, there is still some scatter not accounted for by the measurement errors. In particular, at low V_{esc} several galaxies deviate significantly from the relation. These galaxies also have the highest values of Hβ in the sample, which suggests that the Mgb residuals may be correlated with Hβ. The residual, Δ Mgb ($= \log \mathrm{Mgb}_{\mathrm{obs}} - \log \mathrm{Mgb}_{\mathrm{fit}}$) is shown in Figure 3.6 plotted against $\log$ Hβ. The plot is dominated by a clump of points centred on zero residual, likely due to random scatter about the two relations, however there is a tail of points (highlighted in red) showing a correlation between Δ Mgb and Hβ. The solid black line is a fit to this tail of points and has the form:

$$\Delta \log \mathrm{Mgb} = (-0.36 \pm 0.05) \log \mathrm{H}\beta + (0.07 \pm 0.03) \tag{3.9}$$

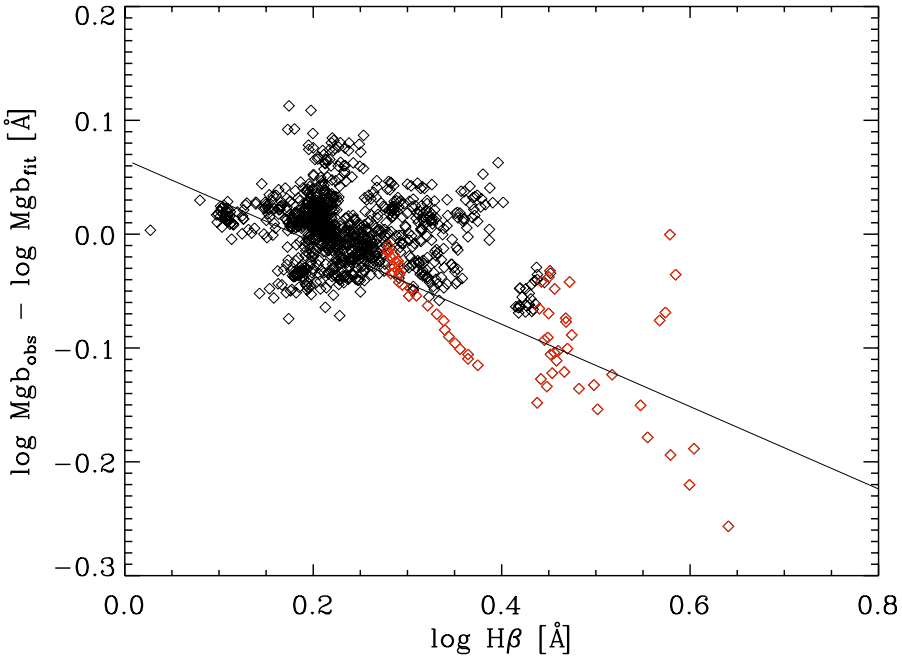

Figure 3.6: The residuals from the Mgb-V_{esc} relation plotted against Hβ. The majority of points are concentrated around zero residual. There is a significant tail of points (highlighted in red) with high Hβ and negative residuals. These points all belong to the outlier galaxies discussed in the text. The solid line is a fit to the red tail of points.

This correlation suggests that a combination of Mgb and Hβ should be more tightly correlated with V_{esc} than only the single index. Using Equation 3.9 I formed the 'corrected index' from the combination of Mgb and Hβ given by:

$$\text{Index} = \log \text{Mgb} + 0.36 \log \text{H}\beta - 0.07 \tag{3.10}$$

In Figure 3.7 I plot this corrected index against the local V_{esc} for all galaxies in the sample.

$$\begin{aligned} \log(V_{esc}/500\text{kms}^{-1}) = \quad & 0.16 + 3.57 \log(\text{Mgb}/4\text{Å}) \\ & +1.29 \log(\text{H}\beta/1.6\text{Å}) \end{aligned} \tag{3.11}$$

The linear relation fit to the central aperture values has a scatter of only $\sigma = 0.025$ in

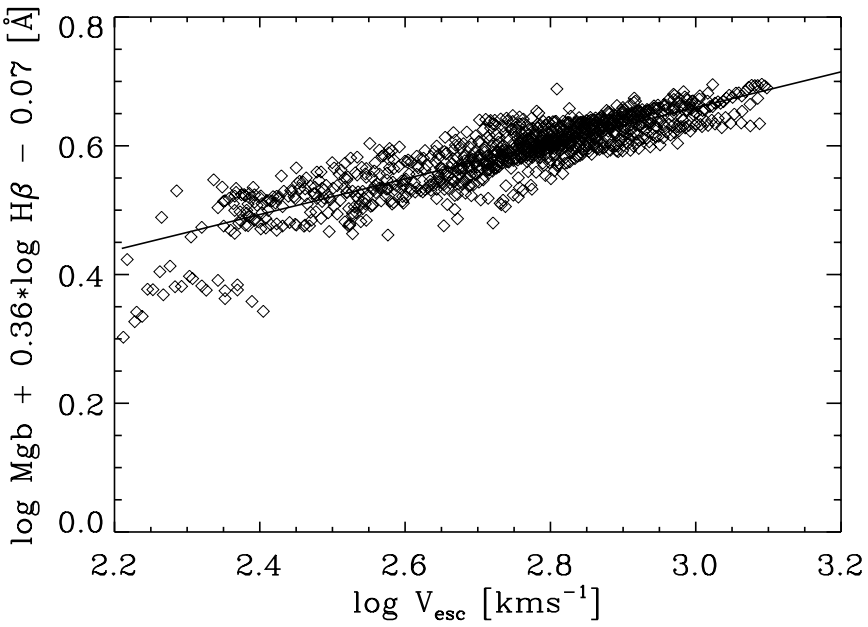

Figure 3.7: The Index-V_{esc} relation corrected using the relationship between the residuals and Hβ given in Equation 3.9. The remaining scatter in this relation is consistent with the measurement errors. Notice that while the correction is driven by the outlying galaxies with negative residuals galaxies with positive residuals in Figure 3.2 also move closer to the relation.

log V_{esc}, reducing the scatter by 22 per cent compared to the uncorrected Mgb-V_{esc} relation. This scatter is now consistent with the measurement errors. Even with the four galaxies with strongest Hβ removed, the reduction in scatter is significant; σ changes from 0.033 to 0.026, a reduction of 20 per cent. As a specific example, the two galaxies at low V_{esc} lying above the Mgb-V_{esc} relation fall on the relation after this correction is applied.

3.5 The Stellar Population-V_{esc} relations

To aid in interpreting the influence of V_{esc} in ETGs I turned to Single Stellar Population (SSP) equivalent ages (t), metallicities ([Z/H]) and alpha enhancements ([α/Fe]) using the SSP models of Schiavon (2007). Full details of this conversion are given in Kuntschner et al. (2010), but I will provide a brief description here. The SSP

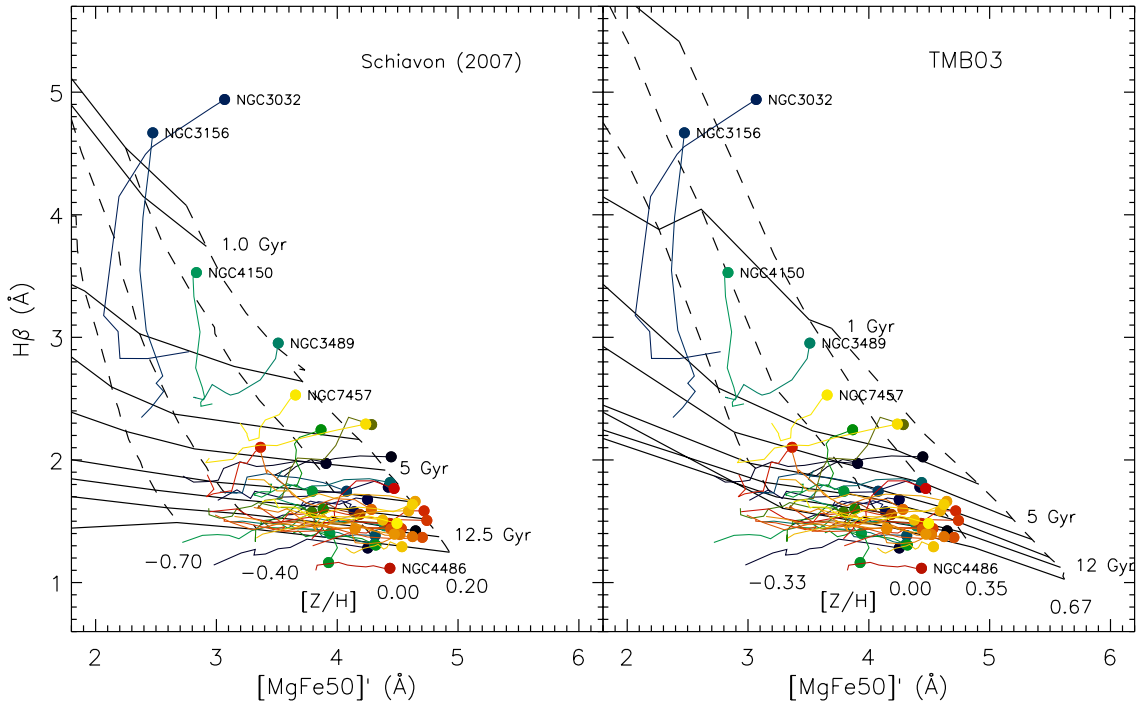

Figure 3.8: Hβ vs. a combination of Mgb and Fe5015 for the SAURON ETG sample. Individual galaxies are shown as the coloured lines. The SSP model grids are shown in black as contours of constant metallicity and age. Left panel shows the SSP models for Schiavon (2007). Right panel shows those for an alternate SSP scheme not used here. Taken from Kuntschner et al. (2010).

models treat each galaxy as a single stellar population with all the stars formed in a single, instantaneous burst with a single age, metallicity and chemical abundance pattern. Using model stellar isochrones and a library of stellar templates spanning a range of stellar ages and metallicities the observable line strength indices are derived for each model population. In the Schiavon (2007) models fitting functions are used to account for different levels of alpha-element enhancement as stellar libraries sampling nearby stars in our own Galaxy do not cover the range of abundance patterns observed in external galaxies. This is particularly important in ETGs that have likely experienced very different star formation histories to our own Galaxy.

While each of the observable indices is sensitive to the three SSP parameters to some degree Hβ is predominantly affected by the SSP age, whereas Mgb and Fe5015 are more strongly dependent on [Z/H] and [α/Fe]. This can be seen in Figure 3.8

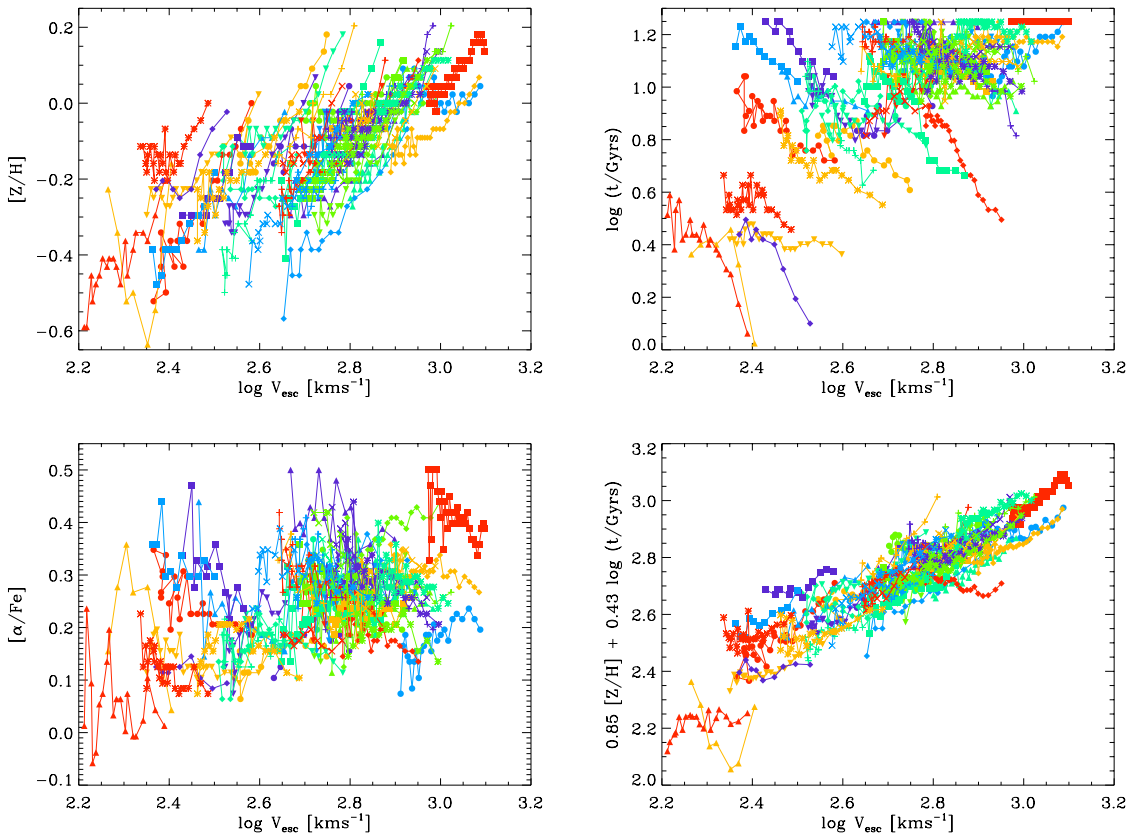

Figure 3.9: Upper panels and bottom left: the V_{esc} vs. [Z/H], Age and [α/Fe]. There is a strong correlation between [Z/H] and V_{esc}, though not as tight as with the individual line strength indices. There is a much weaker correlation with age and [α/Fe]. None of the figures exhibit the local and global correlation observed in the Mgb- and Fe5015-V_{esc} relations. The sharp cutoff at the top of the upper right and lower left figures is due to the limited range of the SSP model. Lower right panel: Edge-on view of the plane connecting [Z/H], age and V_{esc}, derived from a linear fit to the three variables. The relationship between the combination of these three variables is much tighter than in the other three panels. Colours and symbols are as described in Fig. 3.2.

(taken from Kuntschner et al., 2010), illustrating the relation between the observed indices and the SSP model grids and the location of the SAURON galaxies in this space. It is important to remember that these are not true ages, metallicities and alpha-enhancements but SSP equivalent values. While this assumption is clearly unrealistic and the precise values should not necessarily be trusted the relative values between galaxies are robust and allow the variation of these properties within the sample to be explored.

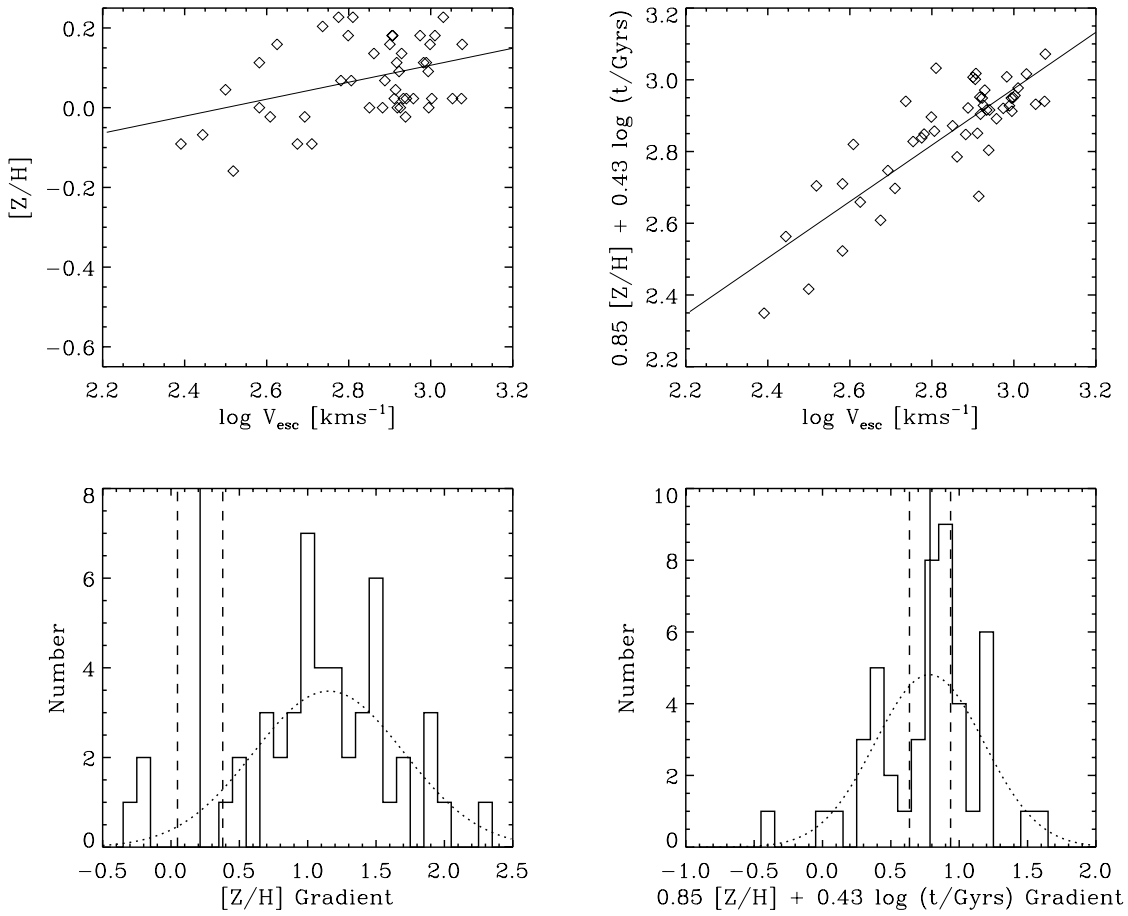

Figure 3.10: Upper row: central aperture measurements for the [Z/H]-V_{esc} and SSP*-V_{esc} relations. The solid line is a linear fit to the data in each case. Lower panel: Distribution of the individual galaxy gradients for the [Z/H]-V_{esc} and SSP*-V_{esc} relations. The solid vertical and dashed lines show the global gradient and the 1-σ bounds respectively. In the [Z/H] relation the distribution of individual galaxies gradients is significantly steeper than the global gradient. In the SSP* relation the individual galaxy gradients show the same local and global behaviour as the Mgb-V_{esc} relation.

For each bin in the SAURON maps a model grid was searched for the line strength indices most closely matching the observed values. Each combination of Mgb, Fe5015 and Hβ is associated with a unique combination of t, [Z/H] and [α/Fe] and these values were assigned to the given bin. Maps of t, [Z/H] and [α/Fe] were constructed in this way for each galaxy with the same binning as the indices, kinematics and V_{esc}. From these maps I measured SSP parameter profiles as described in Section 3.3.

Table 3.1: Principal components from the PCA analysis.

	V_{esc}'	Age'	[Z/H]'	[α/Fe]'	Eigen-value	% of variance
PC1	0.581	0.286	-0.214	-0.731	2.49	62
PC2	0.531	-0.388	-0.606	0.447	1.10	28
PC3	0.399	0.708	0.275	0.514	0.30	8
PC4	0.471	-0.516	0.715	-0.037	0.10	2

Notes: The primed variables are standardised versions of the corresponding variables with zero mean and unit variance.

In Figure 3.9 I show the three SSP-V_{esc} relations. As in Figure 3.2 each colour and symbol combination indicates the profile for an individual galaxy. There is much greater scatter in all three SSP cases than in the Index-V_{esc} relations. The [Z/H]-V_{esc} relation is the tightest of the three, with the t- and [α/Fe]-V_{esc} relations showing much larger scatter. The t and [α/Fe] values also suffer from boundary problems, where the observed indices lie outside the range covered by the SSP model grids. In this case the value at the edge of the model grid is selected and the relations appear to saturate. This is only an artifact of the SSP models and is not a physical effect.

As well as showing more scatter than the Index-V_{esc} relations the individual galaxy gradients show no connection with the global gradient. In the case of [Z/H] the local gradients are typically steeper than the global gradient (Figure 3.10). The t and [α/Fe] profiles are typically much less smooth and as mentioned above suffer from saturation of the SSP model grids and so their gradients have little physical meaning.

3.5.1 Principal Component Analysis

As discussed in Section 3.4.4 a combination of the observed line strength indices correlates more tightly with V_{esc} than any index on its own. Because of this I investigated whether this was also true of the SSP parameters. This investigation was also motivated by the work of Trager et al. (2000), who, in an analysis of the

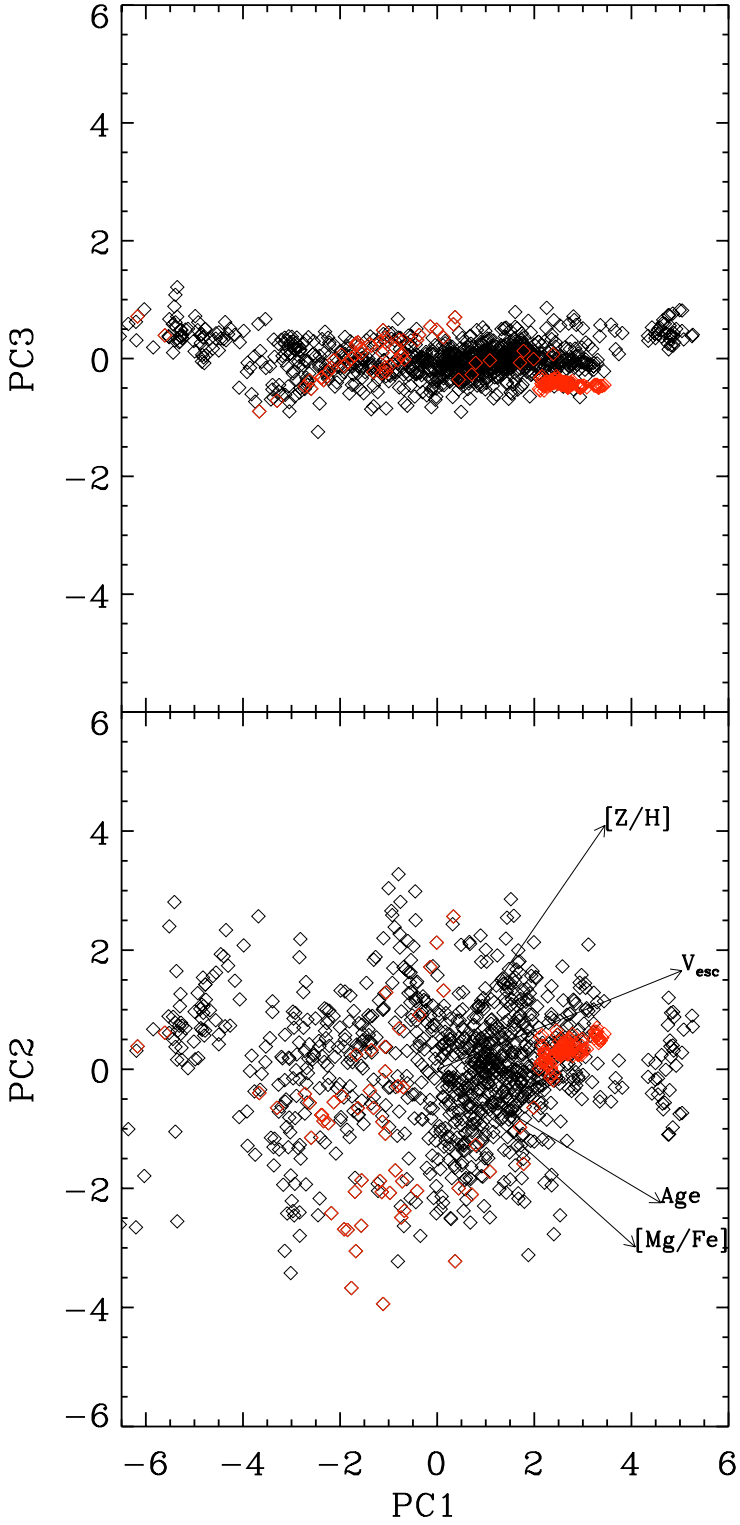

Figure 3.11: Edge-on (upper panel) and face-on views of the SSP-V_{esc} hyperplane. The axes are combinations of V_{esc}, [Z/H], [α/Fe] and t, given in Table 3.1. In the face-on view the directions of the uncombined variables are shown as arrows. The red points indicate the outlying galaxies which do not occupy any particular part of the hyperplane.

central age, metallicity, alpha-enhancement and σ of a sample of 39 nearby ETGs, found that in this four-dimensional space the galaxies are, to a good approximation, confined to a plane.

In order to test whether the same is true of the SAURON ETG sample I performed a Principal Component Analysis (PCA) of the four variables, t, [Z/H], [α/Fe] and V_{esc} for each individual bin. PCA is a statistical technique that finds orthogonal linear combinations of the input parameters (known as Principal Components, PCs) within a multi-dimensional dataset that maximise the variance along the smallest number of these components. An excellent description of the PCA technique and the interpretation of its output can be found in Faber (1973) and Francis & Wills (1999).

When I applied the PCA technique to the SAURON ETG sample I found that the first two PCs contain 90 per cent of the variance. Like the Trager et al. (2000) result, all the data points are, to a good approximation, confined to a plane. Figure 3.11 shows a face-on (lower panel) and edge-on (upper panel) projection of this plane. The projection of the input parameters in this coordinate system are shown as black arrows in the face-on view. The PCs are given in Table 3.1.

3.5.2 A single SSP-V_{esc} relation?

While PCA is a powerful tool in understanding one's data, the interpretation of its results can prove complicated. Trying to assign physical meaning to the PCs themselves is not necessarily the best approach. Instead, guided by the result that the data is confined to a plane, I fit a plane to the three parameters V_{esc}, t and [Z/H]. The best-fitting plane was determined by minimising the residuals normal to the plane. From this fit I defined a combined SSP parameter, that is given by:

$$\mathrm{SSP}* = 0.85 \left[\frac{\mathrm{Z}}{\mathrm{H}}\right] + 0.43 \log\left(\frac{t}{\mathrm{Gyrs}}\right) \tag{3.12}$$

This quantity is plotted against V_{esc} in the right panel of Figure 3.9. This relation is much tighter than any of the individual SSP parameter relations; the scatter is only 0.048, compared to 0.065 in the case of the [Z/H]-V_{esc} relation, with the t and α relations having much larger scatter. The intrinsic scatter in the SSP*-V_{esc} is consistent with that of the Mgb-V_{esc} relation; it also shows the same local and global behaviour. The lower right panel of Figure 3.10 shows the distribution of the individual galaxy gradients, $dSSP^{\star}/dV_{esc}$ and the global gradient determined from $R_e/8$ aperture measurements. The global gradient is 0.79 ± 0.08, while the mean of the distribution of individual galaxy gradients is 0.78 ± 0.40. The typical error on individual gradients is 0.11. The global gradient is consistent with the local gradient well within the errors. The local gradients again show a broader distribution, implying an intrinsic scatter of 32 per cent. This is not the case for [Z/H] alone; here the local gradients are significantly steeper than the global one. The specific combination of age and [Z/H] found depends weakly on the SSP model used, but the tightness of the plane and the local and global connection do not.

Chapter 4

Understanding the Mgb-V_{esc} relation

4.1 Overview

In the previous chapter I described the many galaxy properties that correlate with the local V_{esc}, and hence with the local gravitational potential Φ, observed in the SAURON sample of galaxies. In this chapter I make use of the much larger ATLAS^{3D} sample to further explore the role of V_{esc}. The Index-V_{esc} relations determined from the ATLAS^{3D} sample are fully consistent with those from the smaller SAURON sample. I begin by revisiting the Colour-V_{esc} relation first observed by Franx & Illingworth (1990) then move on to examine the distribution of galaxy properties on the V_{esc} relations described in the previous chapter. I focus on deviations from the Mgb-V_{esc} relation as this is the tightest relation with the smallest measurement errors, as well as displaying the local and global behaviour described in the previous chapter. I explore how these deviations depend on other properties of ETGs. I then go on to examine the underlying physical processes that drive the local and global behaviour of the Mgb-V_{esc} relation and how it fits into our current understanding of galaxy evolution.

4.1.1 The ATLAS^{3D} sample

Motivated by the many interesting results obtained from the SAURON survey, the ATLAS^{3D} survey was designed to expand the SAURON survey to a complete, volume-limited sample, greatly increasing the number of objects and most importantly allowing meaningful comparisons with cosmological simulations. The ATLAS^{3D} sample had similar observability constraints to the SAURON sample as it too was observed from the WHT. The parent sample of ATLAS^{3D} galaxies was selected from the Two Micron All-Sky redshift Survey (2MASS; Skrutskie et al., 2006) using the K_S-band luminosity from the extended source catalogue. The selection criteria for the parent sample were:

- $-6^\circ \leq \delta \leq 64^\circ$
- D $\leq$ 42 Mpc
- $M_K \leq -21.5$ magnitudes
- $|b| \geq 15^\circ$

This yielded a parent sample of 871 galaxies. For full details of the sample selection criteria (in particular the distance measurements and associated errors) see Cappellari et al. (2011a). The ATLAS^{3D} parent sample represents a *complete* sample of nearby galaxies. The ATLAS^{3D} sample was drawn from this parent sample by imposing a morphological selection criteria to select only ETGs. True colour red-green-blue SDSS *gri*-band images (available for 82 per cent of galaxies) or blue DSS2 *B*-band images (18 per cent of galaxies) were visually inspected for the presence of spiral arms (or in edge-on cases prominent dust lanes). This is consistent with the revised Hubble classification system outlined by Sandage (1961), where ETGs are defined as "nebulae... showing no spiral structure". Again, a more detailed discussion of the morphological selection can be found in Cappellari et al. (2011a).

After the morphological selection the final ATLAS^{3D} sample consisted of 260 nearby ETGs, morphologically selected to show no signs of spiral structure.

As well as the SAURON IFU observations the ATLAS^{3D} sample has a substantial set of complementary multi-wavelength observations. This includes archival SDSS *ugriz* photometry (Abazajian et al., 2009), or, where the galaxy does not fall within the SDSS survey area, *ugri* photometry from the Wide Field Camera (WFC) on the 2.5m Isaac Newton Telescope at the Roque de Los Muchachos Observatory on La Palma (see Scott et al., in preparation, for details of this photometry). The survey also includes full coverage from CO single dish observations (Young et al., 2011), and significant coverage from CO interferometry (Alatalo et al., in preparation), HI radio observations (Serra et al., in preparation), deep MegaCam optical photometry (Duc et al., in preparation) and Spitzer mid-IR imaging (Shapiro et al., in preparation).

When determining profiles of various parameters I changed to using elliptical apertures growing logarithmically in radius for the ATLAS^{3D} sample. Each subsequent elliptical annulus having an outer major-axis radius a factor $10^{0.1}$ larger than the previous aperture. This was done because the ATLAS^{3D} sample includes many faint, small galaxies and a larger aperture at large radius improves the S/N of the measurements. This change had no measurable effect on the profiles of galaxies in common between the two samples, though the error on data points at large radii was reduced. Unless otherwise mentioned the determination of V_{esc}, extraction of profiles and all other elements of the analysis, are as described in the previous two chapters.

4.2 The Colour-V_{esc} relations

The original study of the role of V_{esc} in ETGs by Franx & Illingworth (1990) looked at the connection with local colour rather than local line strength indices. As with absorption indices, the colours are closely related to the star formation history and

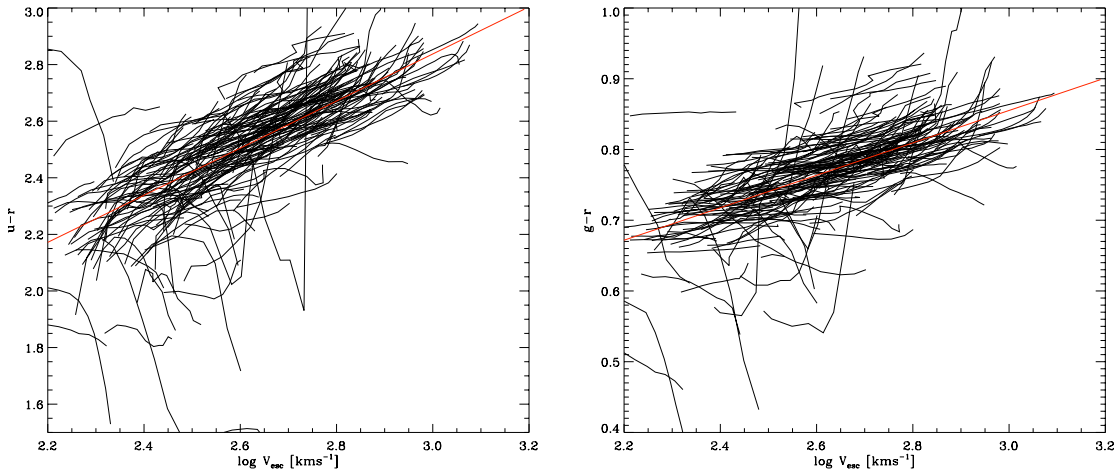

Figure 4.1: *u-r* and *g-r* vs. V_{esc} for a subset of the ATLAS^{3D} sample. Colour profiles were determined from the SDSS photometry from the identical apertures used to extract the V_{esc} profiles. The red line is a fit to R_e aperture measurements. The colour profiles are affected by saturation effects, dust and nearby stars. As with the Mgb-V_{esc} relation shown in the previous chapter there is a tight correlation with increasing scatter at low V_{esc}. This effect is more pronounced in the *u-r* relation than in the *g-r* relation.

stellar population properties of a galaxy, but again the relation is a complex one. Different colours are sensitive to different components of the stellar population, hence can be used as an additional tool to study the influence of the local V_{esc} in ETGs.

Because of the *ugriz* photometric coverage of the ATLAS^{3D} sample I revisited the work of Franx & Illingworth (1990) with a significantly larger sample (230 galaxies compared to 17) and with improved dynamical modelling, thanks to the SAURON IFU data and the JAM technique. I use only the 230 ATLAS^{3D} galaxies that have SDSS photometry available to eliminate any additional scatter due to zeropoint differences between the SDSS and INT observations.

Colour profiles for all galaxies were formed using the technique described in Section 3.3, with several modifications required because of the differences between the photometric images and the maps of IFU-based quantities. I formed colour maps from the sky-subtracted, dust-corrected, masked SDSS images. The median pixel value of the colour map within each elliptical aperture was assigned to the

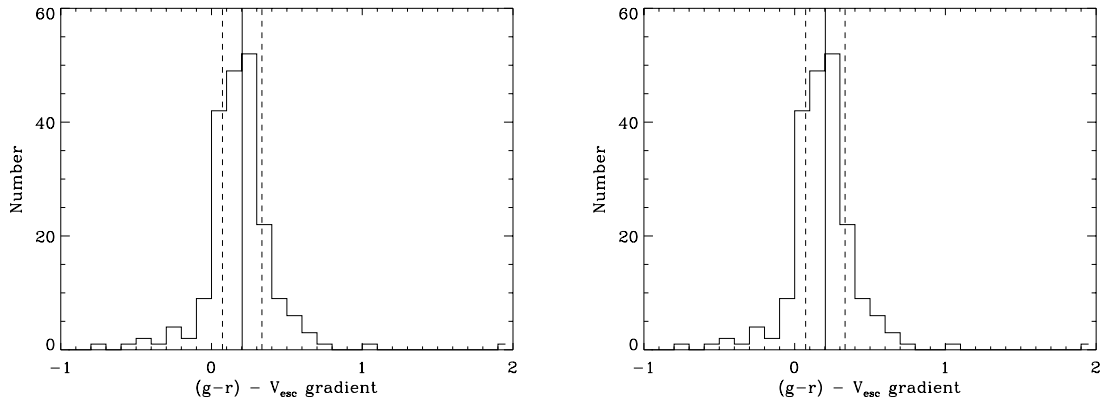

Figure 4.2: Distribution of the individual *g*-*r*- and *u*-*r*-V_{esc} gradients for a subset of the ATLAS^{3D} sample. The vertical solid and dashed lines show the global gradient and $1-\sigma$ bounds respectively. Both relations show the same global and local connection as the Mgb-V_{esc} relation in that the distribution of local gradients is consistent with the global gradient.

profile. The apertures were chosen to match those used for the SAURON maps, again excluding the central 2 arcseconds and growing to the same radius. The PA and ϵ used were the same as in the SAURON maps - perturbations such as bars or dust features that can significantly affect the photometric PA over the SAURON field of view were ignored.

Figure 4.1 shows the *g*-*r*- and *u*-*r*-V_{esc} profiles for the SDSS subset of the ATLAS^{3D} sample. I selected these colours as the *g*- and *r*- bands have the highest S/N and hence show the tightest relation, while the *u*-band is more sensitive to young populations. Each thin black line shows the profile for an individual galaxy, the red line shows a fit to the R_e aperture values. I found the same behaviour as in the Mgb - V_{esc} relation: a tight correlation with increasing scatter appearing at low V_{esc}. This increase in scatter is more evident with the *u*-*r* colour than with *g*-*r*. I also found the same local and global behaviour described above (see Figure 4.2), in that individual galaxy gradients are consistent with the global relation determined from central values. Fitting to the R_e aperture values for those galaxies with

$V_{esc}(Re/8) > 400 kms^{-1}$ I found that the colours are given by:

$$g - r = (0.26 \pm 0.03) \log V_{esc} + (0.08 \pm 0.05); \sigma = 0.04 \quad (4.1)$$

$$u - r = (0.80 \pm 0.08) \log V_{esc} + (0.47 \pm 0.14); \sigma = 0.12. \quad (4.2)$$

That I observe this local and global connection from both Mgb and the photometric colours suggests that this represents a fundamental process in galaxy formation rather than a 'conspiracy' of metallicity and age resulting in the unique behaviour of the Mgb index.

4.3 Deviation of galaxy gradients

The most striking deviations from the Index-V_{esc} relation are a population of galaxies at low V_{esc} which exhibit negative Mgb-V_{esc} gradients and steeply positive Hβ-V_{esc} gradients. These 'negative gradient' galaxies are also seen in the Colour-V_{esc} diagram, particularly in the u-r-V_{esc} relation. These galaxies are only found below $V_{esc} = 400$ kms^{-1}. For the moment I will put aside these galaxies with strong gradient deviations (I will discuss them in detail in Section 4.5) and instead look at the gradients of more regular galaxies. Selecting only galaxies with $dMgb/dV_{esc} > 0.0$, I examined the correlation of the local gradients with a wide range of other galaxy properties and found that these gradients do not depend on any other parameters. These include, but are not limited to: classification (both morphological and kinematic), V/σ, size, mass, luminosity, apparent flattening, central line strengths, age (when excluding negative gradient galaxies), gas content, and local environmental density.

4.4 Residuals from the Mgb-V_{esc} relation

Apart from deviations in their local gradients galaxies can also deviate from the Mgb-V_{esc} relation by being offset from the main relation. I quantify this deviation by determining the mean residual of each galaxy from the Mgb-V_{esc} relation, Δ Mgb:

$$\begin{aligned}\Delta\mathrm{Mgb} &= \log\langle \mathrm{Mgb_{obs}}\rangle - \log\langle \mathrm{Mgb_{fit}}\rangle \\ &= \log\langle \mathrm{Mgb_{obs}}\rangle - 0.35\log\langle \mathrm{V_{esc}}\rangle - 0.41. \end{aligned} \tag{4.3}$$

The key result to take from the Mgb-V_{esc} relation is that galaxies show the same behaviour both locally and globally. The Mgb-V_{esc} relation holds whether it is measured in a central aperture or in annuli. This scale-independent behaviour suggests that the Mgb-V_{esc} relation should hold at all points within the central regions of ETGs. It is easy to test this with IFU data by plotting the Mgb-V_{esc} relation for individual bins, completely ignoring any information as to which galaxies any given bin belonged to. The result of this analysis is shown in Figure 4.3. Because of the sheer number of individual bins in the ATLAS^{3D} data it is necessary to display this in a different fashion to the elliptical annuli data, with the contours reflecting the number of bins at any given point in the Mgb-V_{esc} plane. As usual the best-fitting global relation is overplotted as a solid red line, which follows the contours precisely.

The bin data are fully consistent with that determined from elliptical annuli. The overall behaviour of the relation is also the same, with significantly increasing scatter below $V_{esc} = 400\mathrm{kms}^{-1}$. This tight relation found even when considering individual bins allows us to go further than the globally-averaged mean residual described above and consider the residuals of individual bins from the Mgb-V_{esc}

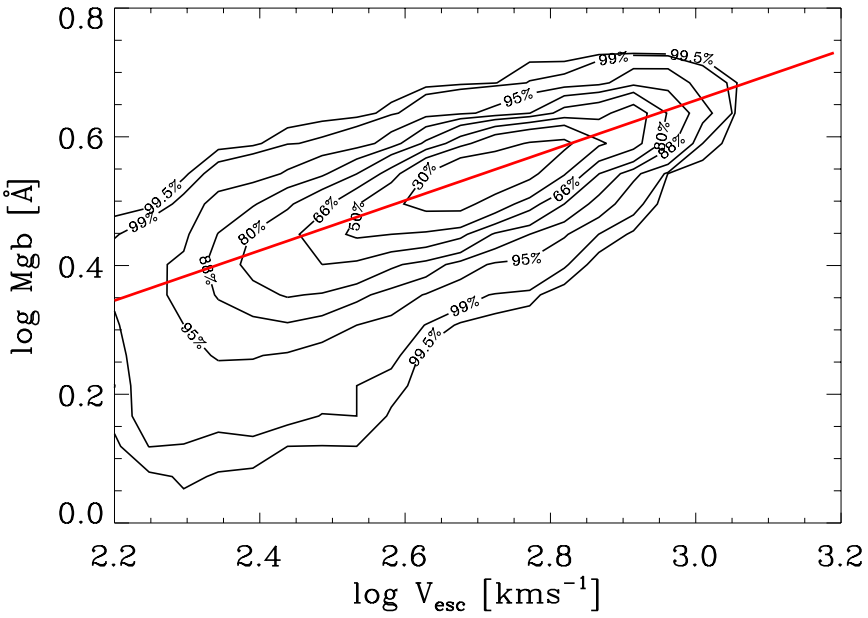

Figure 4.3: Mgb-V_{esc} relation determined from individual bins as opposed to averaging over elliptical annuli. The solid red line in each case shows the best-fitting relation to the central aperture measurements. In the Mgb-V_{esc} relation the contours of the individual bins follow the central relation.

relation. As above I define the bin-by-bin residuals, Δ_b Mgb:

$$\begin{aligned}\Delta_b\mathrm{Mgb} &= \log\langle\mathrm{Mgb}_{\mathrm{obs},b}\rangle - \log\langle\mathrm{Mgb}_{\mathrm{fit},b}\rangle \\ &= \log\langle\mathrm{Mgb}_{\mathrm{obs},b}\rangle - 0.35\log\langle\mathrm{V}_{\mathrm{esc},b}\rangle - 0.41 \qquad (4.4)\end{aligned}$$

where the subscripts b refer to quantities measured in individual bins, as opposed to the subscriptless values referring to the elliptical aperture measurements.

4.4.1 Mgb disks

While I use the same elliptical annuli to measure both the index and V_{esc} profiles, the index and V_{esc} maps often have somewhat different isocontour shapes. While some of this variation can be accounted for by measurement errors there are a number of cases where the isocontours of the Mgb and Fe5015 maps show a prominent disk-like structure. This effect is most pronounced in the Mgb maps. This issue was discussed

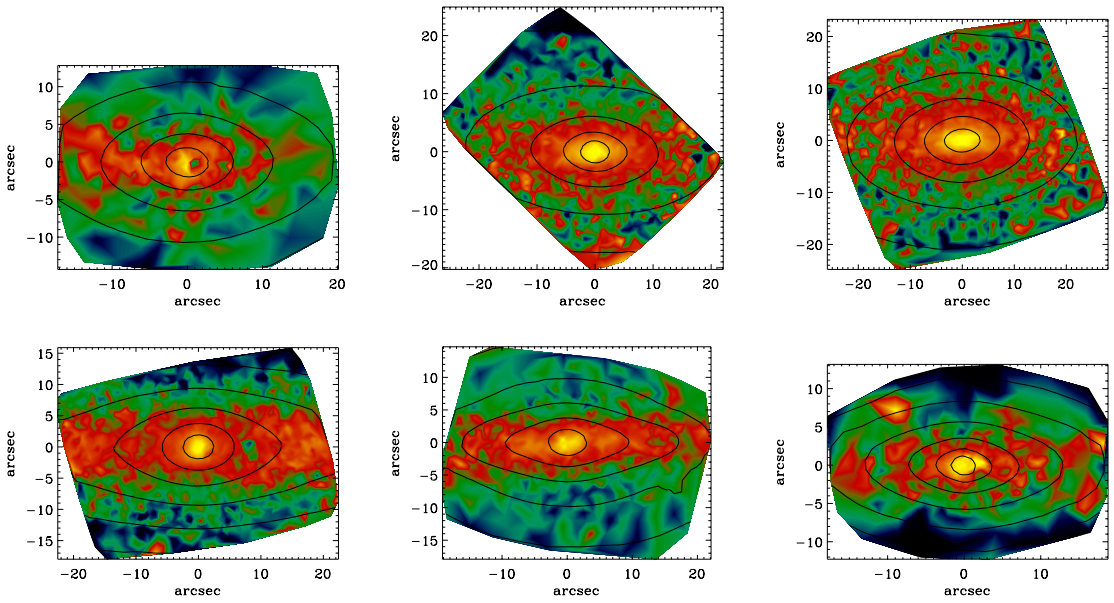

Figure 4.4: Examples of Mgb disk structures in the IFU maps. From top left the galaxies shown are: NGC2577, NGC3377, NGC4473, NGC4570, NGC4638 and NGC5611. High values of Mgb are indicated by yellow colours. The flux contours from the collapsed SAURON cubes are overplotted. The Mgb isocontours are flatter than the isophotes in each case.

briefly in Kuntschner et al. (2006) and Krajnović et al. (2008). Here I explore how these structures in the index maps affect the Mgb-V_{esc} relation.

I selected by eye a sample of 27 galaxies showing a prominent flattened Mgb component in the Mgb maps. A few examples of galaxies with flattened Mgb structures are shown in Figure 4.4. These galaxies do not occupy any particular region of the Index-V_{esc} diagrams, being indistinguishable from early-types that do not exhibit a flattened Mgb component (see the upper panel of Figure 4.5). However, these galaxies have steeper gradients than the typical early-type (as well as being steeper than the global relation) as shown in the lower panel of Figure 4.5. The shift in slope is small, only 1.5σ above the mean local gradient for the whole sample. When I exclude the negative gradient galaxies (as these are clearly a different population) a Kolmogorov-Smirnov test (KS-test) returns a probability of 0.17 that the two sets of gradients are drawn from the same distribution, which is inconclusive. However, these galaxies have residuals from the Mgb-V_{esc} relation consistent with the

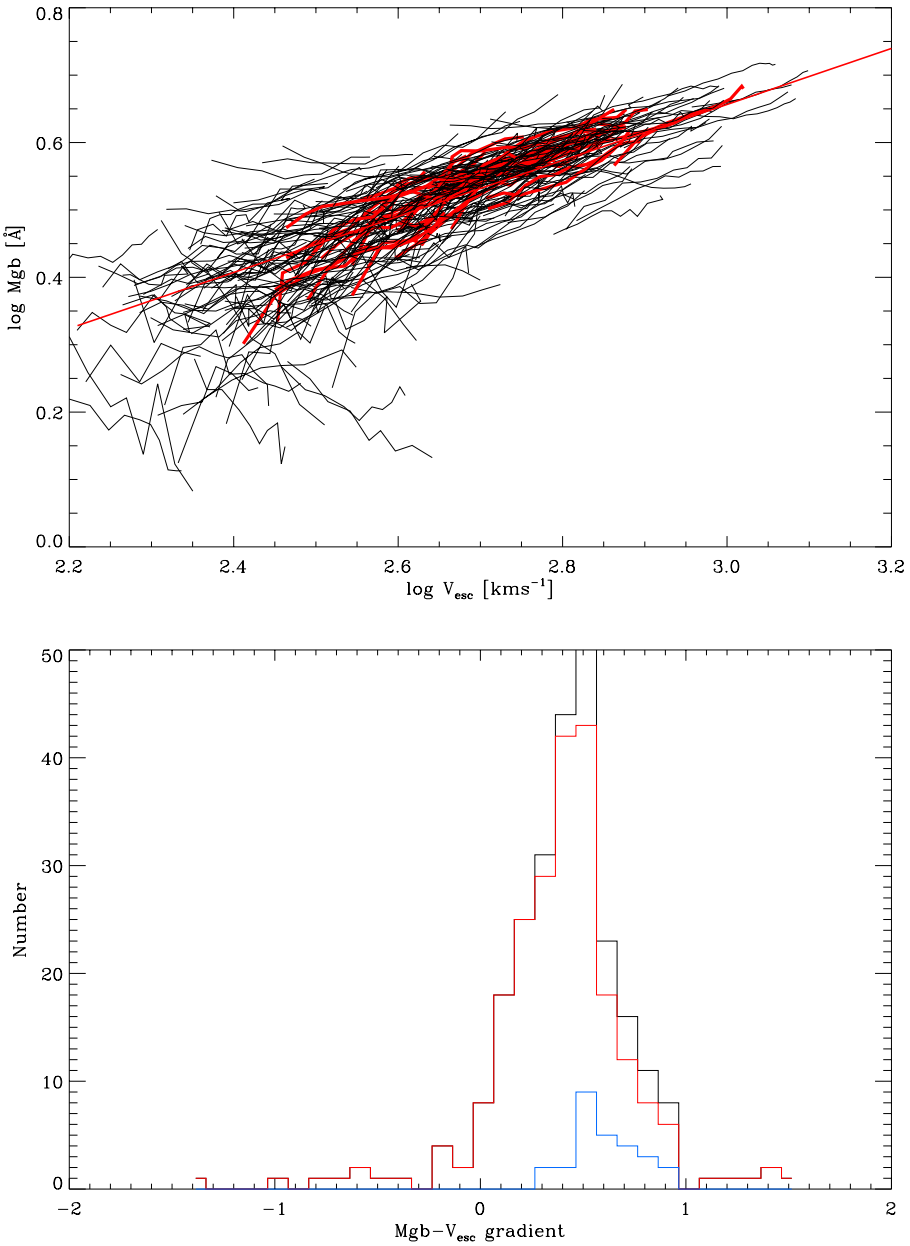

Figure 4.5: Upper panel: the Mgb-V_{esc} relation for the ATLAS^{3D} survey with those galaxies selected by eye as having Mgb disks highlighted in red. The solid red line indicates the central aperture relation. The Mgb disk galaxies appear typical of ATLAS^{3D} ETGs without Mgb disks. Lower panel: histogram of individual galaxy gradients with the Mgb disk and non-disk galaxies indicated in blue and red respectively. The Mgb disk galaxies are offset to slightly steeper gradients, though this is not statistically significant when the negative gradient galaxies are excluded.

full sample of galaxies. This suggests that the choice of elliptical apertures is robust against structure in the linestrength maps, though the enhanced Mgb disk structures observed in ETGs may prove to be interesting objects of study in themselves.

4.4.2 Morphologies and kinematics

As discussed in Chapter 1, there are several ways of dividing ETGs into different sub-classifications. The most common choice, based on the Hubble tuning fork diagram, is to divide early-types into elliptical and lenticular galaxies based on their optical morphologies. Using the RC3 classifications of de Vaucouleurs et al. (1991) there are 68 elliptical galaxies and 192 lenticular galaxies in the ATLAS^{3D} sample. An alternative classification, proposed by Emsellem et al. (2007) and Cappellari et al. (2007), divides ETGs based on their kinematic properties. Specifically, they propose two classes, fast rotators (FRs) and slow rotators (SRs) based on their specific angular momentum, λ_R. Fast rotators have predominantly rotation-dominated, disk-like kinematics whereas slow rotators are predominantly pressure supported. According to Emsellem et al. (2011) the ATLAS^{3D} sample contains 221 FRs and 39 SRs.

Blindly comparing subsamples using the traditional E/S0 classification does reveal a difference, but this is due to the S0 sub-sample being dominated by the low mass galaxies where the scatter about the relation is larger. When comparing galaxies of similar mass I found no difference between the two classes in terms of their Index-V_{esc} relations.

I also found no difference between the FR and SR samples, despite the very different kinematics (and likely origins) of the two classes. Looking in more detail, (Figure 4.6) I found that the residuals from the relation show no dependence on $\lambda_{Re}/\sqrt{\epsilon}$, the parameter used by Emsellem et al. (2011) to divide FRs from SRs. As far as the Mgb-V_{esc} relation is concerned all ETGs are alike, independent of their classification. It would be interesting to examine whether spiral galaxies also lie on the Mgb-V_{esc} relation, but spirals present a somewhat different challenge when it

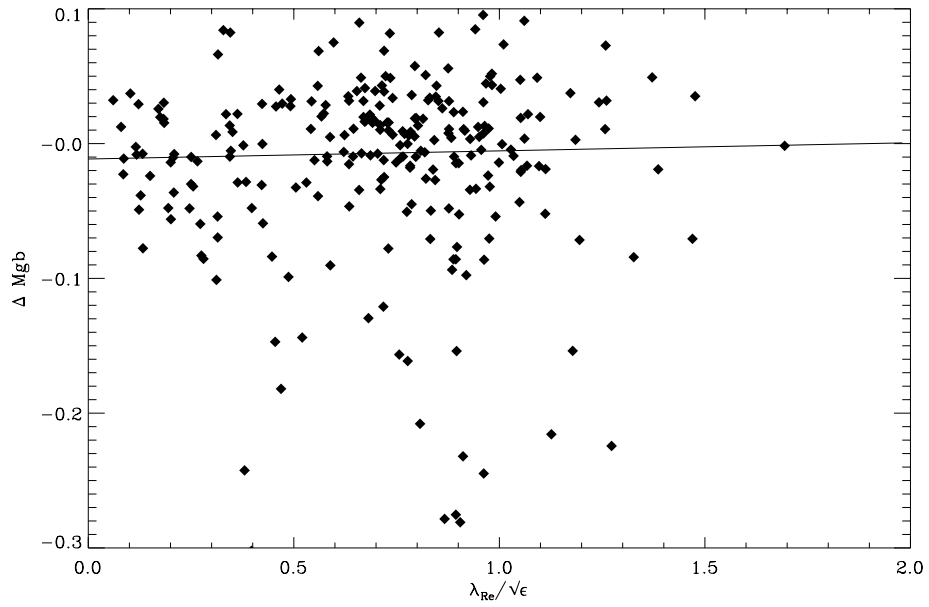

Figure 4.6: $\lambda_{\rm Re}/\sqrt{\epsilon}$, the specific angular momentum within an effective radius, R_e divided by $\sqrt{\epsilon}$, vs. ΔMgb. This is the criteria used by Emsellem et al. (2011) to differentiate between SRs and FRs. There is no trend of the residuals with $\lambda_{\rm Re}/\sqrt{\epsilon}$, further supporting the fact that the Mgb-$V_{\rm esc}$ relation is universal for both fast and slow rotators.

comes to measuring their line strengths because of the predominance of recent star formation.

4.4.3 Stellar population properties

In the previous chapter I demonstrated that the residuals from the Mgb-$V_{\rm esc}$ relation are correlated with the local Hβ, though it is important to note that much of this correlation is driven by the negative gradient galaxies. In this section I will discuss in greater detail the dependence of the residuals on the SSP parameters. In Figure 4.7 I show the dependence of Δ_b Mgb against t, [Z/H] and [α/Fe] for all individual bins.

There is a significant concentration of bins at both old ages and high values of [α/Fe]. This is due to the saturation of the SSP models when the edge of the model grids is reached and is not a true physical effect. The upper panel shows that for $t > 2$ Gyrs there is essentially no dependence of Δ Mgb on age. Below $t = 2$ Gyrs

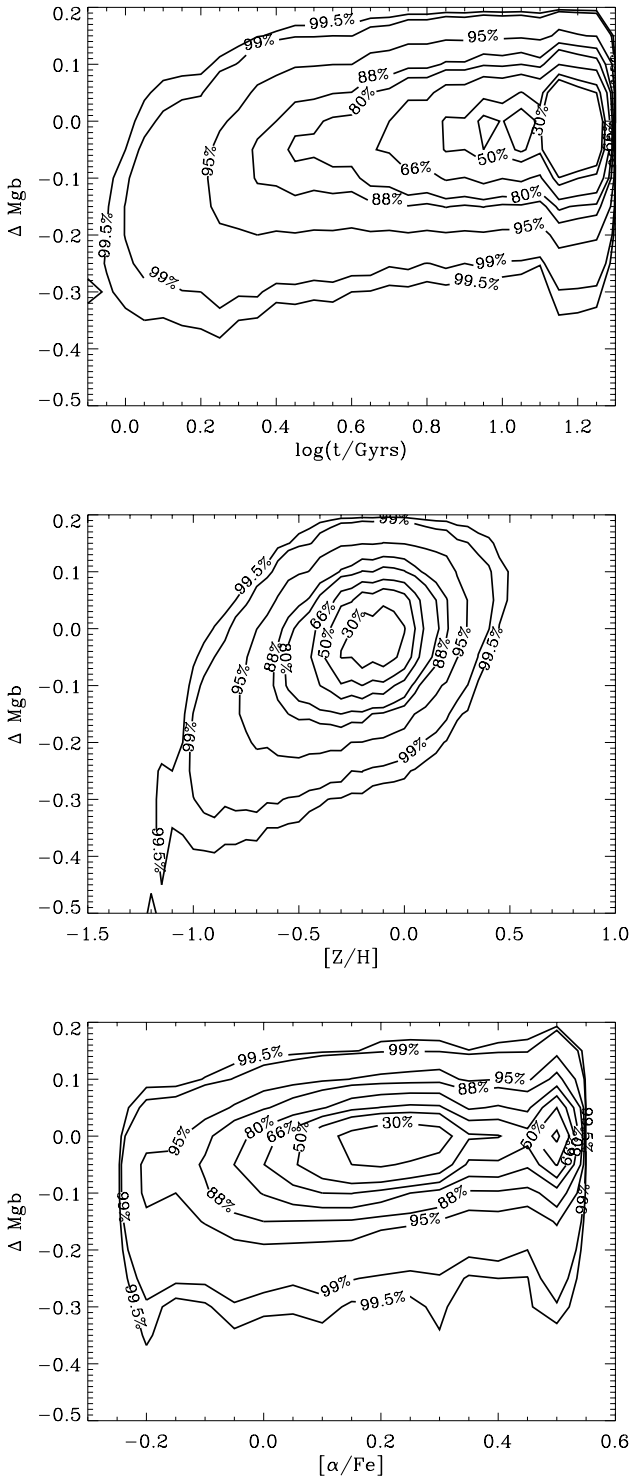

Figure 4.7: The residuals from the Mgb-V_{esc} relation for individual bins, Δ_b Mgb, against the SSP parameters. The contours are labeled with the total fraction of points they enclose. There is a concentration of points on the right hand side of the upper and lower panels due to saturation of the SSP model grids. In the t and [Z/H] panels there is no strong trend of the residuals until outlying points are considered, where metal poor and young bins have negative residuals. In the [α/Fe] panel there is a weak trend of increasing residuals with increasing α over the full range of values.

the residuals become predominantly negative. This is likely due to the negative gradient galaxies discussed in Section 4.5. The middle panel shows a similar trend, with the majority of points being clustered around ΔMgb = 0 and [Z/H] = -0.2. The contour enclosing 66 per cent of the points shows no trend of the residuals with [Z/H]. A small fraction of low metallicity points show strongly negative residuals, again likely due to the negative gradient galaxies. There is some suggestion of the opposite effect, with the highest metallicity galaxies having positive residuals, though the effect is weak.

In contrast the lower panel shows a clear but weak correlation of Δ_bMgb with [α/Fe]. The residuals are tightly correlated with α over the full range of enhancements found in the ATLAS^{3D} sample. The trend is weak; Δ_bMgb varies by only ~ 0.1 from $\alpha = -0.2$ to $\alpha = 0.5$. Compared to the scatter in the Mgb-V_{esc} relation this is a significant effect. Weak trends like this can be examined because of the large number of data points available when considering the bins independently; there are over 200,000 independent bins in the ATLAS^{3D} IFU data set. A linear fit to the Δ_bMgb - [α/Fe] data gives:

$$\Delta_b\text{Mgb} = (-0.040 \pm 0.004) + (0.144 \pm 0.008)[\alpha/\text{Fe}]_b. \tag{4.5}$$

4.4.4 Environment

Th ATLAS^{3D} sample covers a broad range of environmental densities, allowing it to be used to study trends of galaxy properties with environment. The simplest example of this is to divide the sample into those galaxies that are part of the Virgo cluster (the only dense environment in the sample) and those that are not. While this simple criterion divides the sample roughly into a dense and sparse environment a finer division of environments can also be revealing. In particular the Virgo/non-Virgo criterion fails to recognise non-Virgo galaxies in groups or the significant

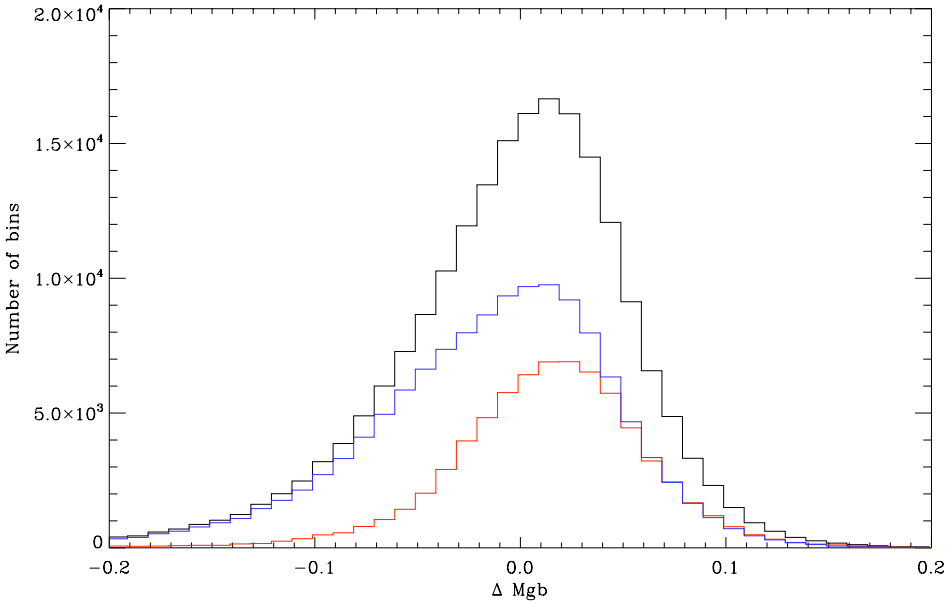

Figure 4.8: Histogram of the residuals from the Mgb-V_{esc} relation of individual bins. The black line shows the residuals for all bins, the red and blue histograms indicating bins beloning to Virgo and non-Virgo galaxies respectively. The Virgo bins are offset to positive residuals; at fixed V_{esc} individual bins in galaxies in the Virgo cluster have higher Mgb values than corresponding bins in the field.

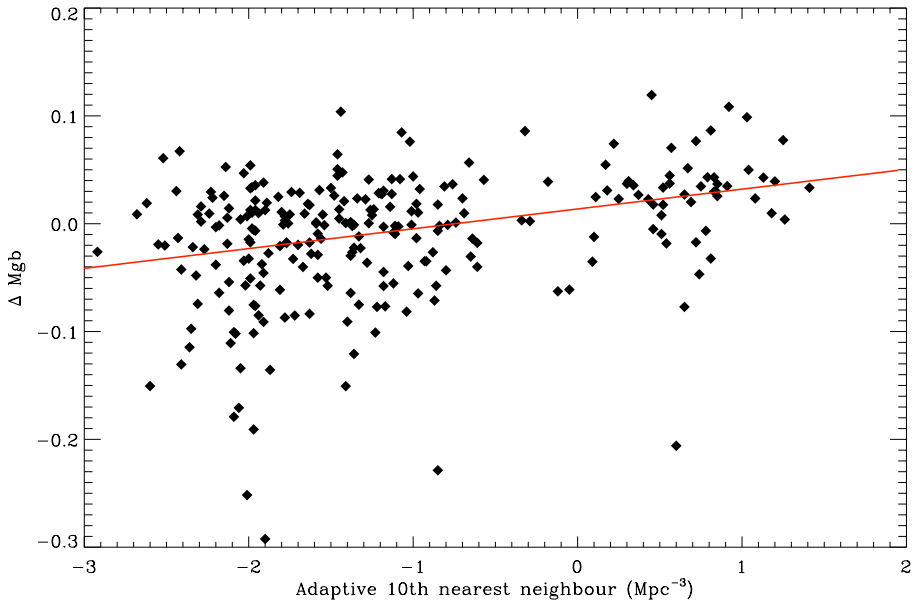

Figure 4.9: Environmental dependence of the Mgb-V_{esc} relation. The mean residual of each galaxy, Δ Mgb is shown against ρ_{10}, an estimator of the local volume density of galaxies. The solid red line is a linear fit to the data. Across all environments there is a trend for galaxies in denser environments to have positive residuals. Galaxies with $\rho_{10} > 0.0$ are all in the Virgo cluster.

variation in local environment between the outskirts and the core of the Virgo cluster itself.

The parent sample of the ATLAS^{3D} survey, described above, consists of all galaxies brighter than $M_K = -21.5$ within 42 Mpc, independent of morphological type. With this information it is possible to accurately characterise the local environmental density for the entire ATLAS^{3D} early-type sample. It is possible to characterise the local environmental density in a variety of ways: in terms of the number density of nearby galaxies or the total luminosity density, using a spherical volume around each galaxy or a cylindrical projection combined with a range in recession velocity. These indicators and the details of their measurement are described in Cappellari et al. (2011b). I made use of the environmental estimators ρ_{10} and Σ_3. ρ_{10} is defined as the volume number density in Mpc^{-3} of galaxies within a sphere whose radius is defined by the distance to the 10$^{\text{th}}$ nearest neighbour: $\rho_{10} = N_{gal}/(4/3\pi r_{10}^3)$. ρ_{10} probes the 'large-scale' local environment, however, as it makes use of a variety of different distance indicators it can be affected by inaccuracies in those distance estimators. Σ_3 is defined as the surface number density in Mpc^{-2} within a cylinder of radius r_3 and height $h = 600\text{kms}^{-1}$ centred on the galaxy which contains the three nearest neighbours: $\Sigma_3 = N_{gal}/(\pi r_3^2)$. Σ_3 is a measure of the local environment on finer scales and is based only on the heliocentric recession velocity as a distance indicator.

In Figure 4.8 I show the dependence of the residuals of all bins Δ_bMgb divided into Virgo and non-Virgo members. Here bins belonging to Virgo cluster galaxies (shown in red) are offset to positive residuals. Non-Virgo bins (shown in blue) follow the main relation and also contain the majority of the tail of negative residual bins. At fixed V_{esc}, a given point in a galaxy is enhanced in Mgb if it lies in the Virgo cluster. To examine this environmental effect in more detail I considered the dependence of the residuals from the Mgb-V_{esc} relation on the local environmental density estimators, ρ_{10} and Σ_3. This is shown in Figure 4.9 for ρ_{10}, the large-scale

measure of environment. The best fitting relation is shown in red. In both cases I found a trend that the residuals are more positive (i.e. that galaxies are enhanced in Mgb at a given V_{esc}) in higher density environments. The correlation is essentially the same for both environmental measures. The relations between Δ Mgb and ρ_{10} and Σ_3 are:

$$\Delta\text{Mgb} = (0.016 \pm 0.003) \log \rho_{10} + (0.010 \pm 0.002); \sigma = 0.048 \tag{4.6}$$

$$\Delta\text{Mgb} = (0.016 \pm 0.003) \log \Sigma_3 - (0.012 \pm 0.003); \sigma = 0.043. \tag{4.7}$$

4.4.5 Correlations with gas content

Along with the SAURON IFU data and optical imaging the ATLAS^{3D} survey also consists of a wide range of supporting multi-wavelength data including millimetre observations of carbon monoxide (CO) emission and radio observations of the neutral hydrogen (HI) emission. Details of these observations are given in Young et al. (2011) and Serra et al. (in preparation) respectively. These observations trace the cold molecular and neutral gas content of the ATLAS^{3D} sample. This cold gas is important because it is thought to provide the reservoir for future star formation. In particular the CO emission which traces the dense molecular gas is strongly correlated with recent and on-going star formation, both as an integrated quantity and spatially within individual galaxies. By measuring the flux of the CO and HI emission it is possible to not only identify galaxies that do contain cold gas but also to estimate the masses of these components. The CO observations cover the entire early-type sample, however the HI observations cover only a subset of the sample due to declination constraints on the observations. The dust content of galaxies is also closely related to star formation and the cold gas content. I described in Chapter 2 how the presence of dust is identified from optical photometry. The

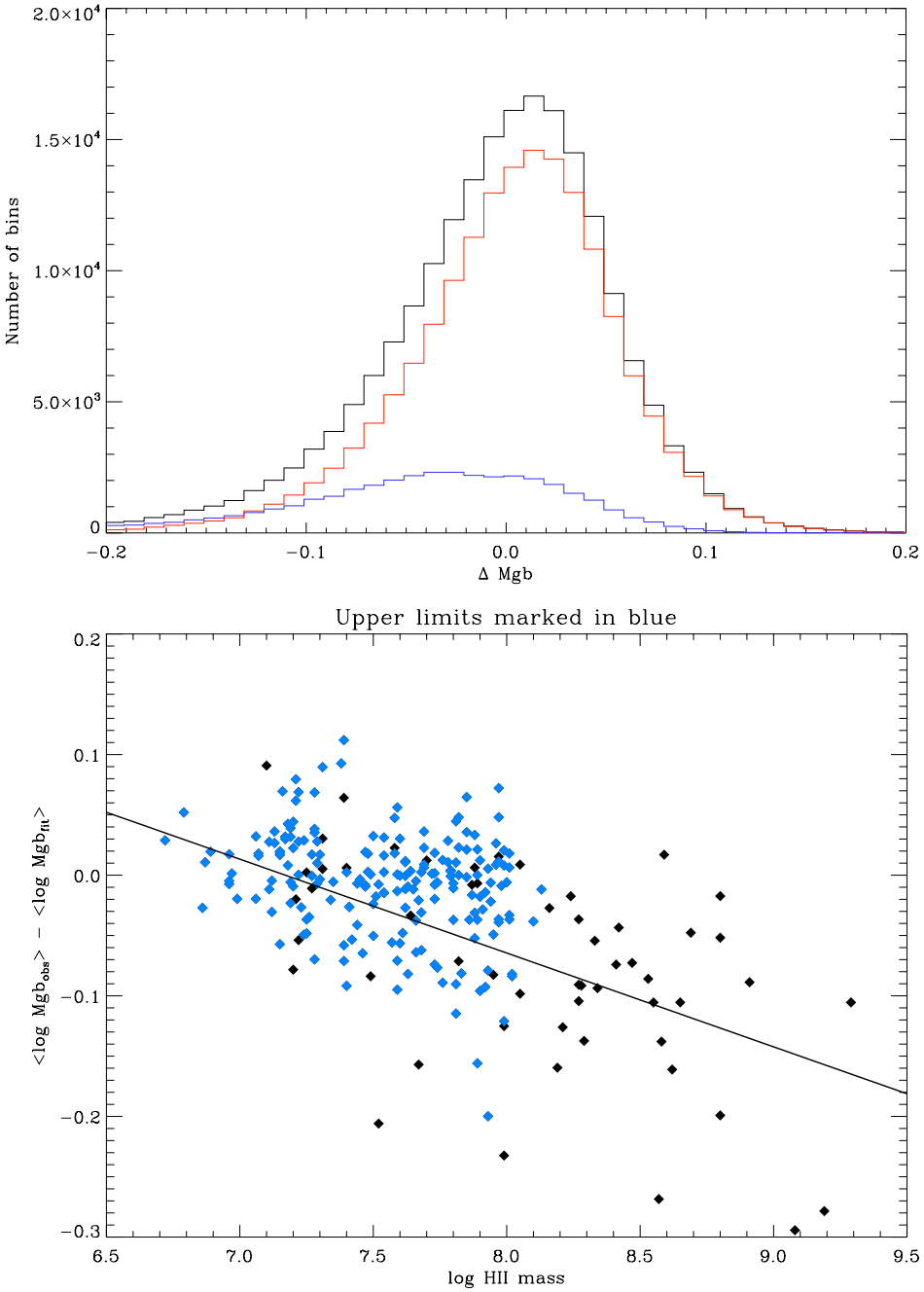

Figure 4.10: Upper panel: Histogram of the residuals from the Mgb-V_{esc} relation for individual bins. Black line shows all bins. Blue line shows bins from galaxies containing dust, identified from the SDSS images. Red line shows bins from galaxies with no dust visible in the SDSS images. Lower panel: Δ Mgb vs. molecular gas mass as inferred from the CO measurements. Black points indicate detections, blue points indicate upper limits from non-detections. Galaxies having large molecular gas masses have negative residuals from the Mgb-V_{esc} relation, or lower than average Mgb index at a given V_{esc}.

ATLAS^{3D} photometry is insufficient to constrain the dust masses, it only identifies those galaxies that do contain dust. These data provide significant information on the non-stellar baryonic content of the ETGs in the ATLAS^{3D} sample.

In the upper panel of Figure. 4.10 I show the residuals from the Mgb-V_{esc} relation for all bins, with bins belonging to galaxies containing significant amounts of dust shown in blue. The overlap between dusty and CO detected galaxies is significant, so it is reasonable to talk about the dusty and CO detected galaxies as a single group. As can be seen these galaxies are strongly biased towards having negative residuals; at a given V_{esc} a dusty (or CO detected) galaxy will typically have a weaker Mgb line strength than a dust-free (or non-detected) galaxy. I quantify this statement by plotting the residuals from the Mgb-V_{esc} relation against the HII molecular gas mass inferred from the CO measurements in the lower panel of Figure 4.10. There is a clear correlation between molecular gas mass and Δ Mgb, in the sense that at fixed V_{esc} galaxies with more molecular gas have weaker Mgb line strengths. While the ATLAS^{3D} HI sample is smaller it is also consistent with this picture, in that HI detected galaxies are generally found below the relation. The relationship between Δ Mgb and molecular gas mass is given by:

$$\Delta\mathrm{Mgb} = (0.059 \pm 0.007) \log \mathrm{H_2} + (0.434 \pm 0.021); \sigma = 0.051. \quad (4.8)$$

4.5 Negative gradient galaxies

In Chapter 3 I briefly noted a population of galaxies that have Mgb-V_{esc} profiles with negative gradients. These galaxies are only present below $V_{esc} = 400$ kms^{-1}, where they significantly increase the scatter in the relation. They have strongly positive Hβ-V_{esc} gradients, in contrast to the flat or shallow gradients exhibited by typical ETGs in the sample. They also exhibit negative colour-V_{esc} gradients, with the effect being more pronounced with the u-r colour than the g-r colour.

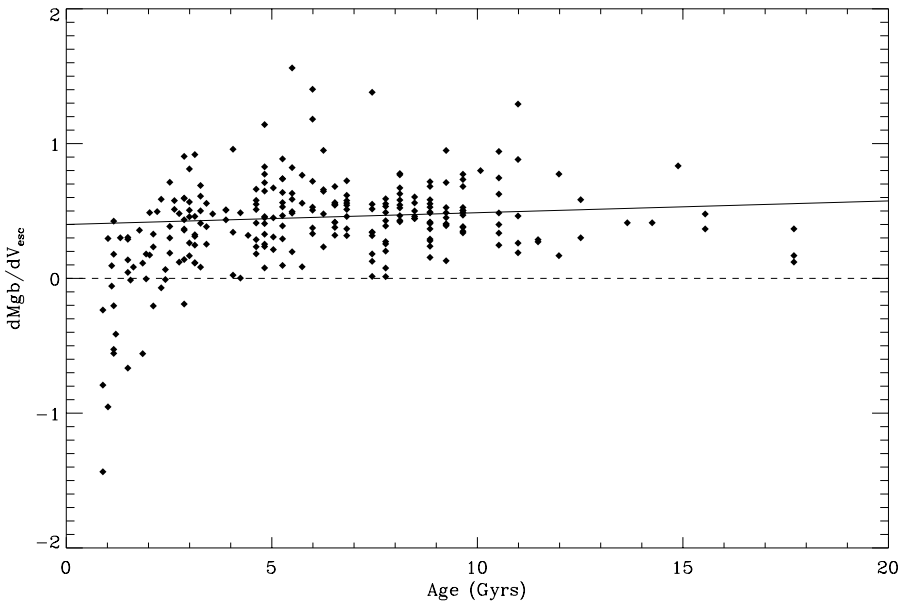

Figure 4.11: Mgb-V_{esc} gradient vs. central age, measured within an aperture with radius $R_e/8$. Negative gradient galaxies all have young central ages. Old galaxies (t $>$ 2 Gyrs) show no trend with age.

High values of Hβ and blue *u-r* colours are usually indicative of a young stellar population. This was confirmed by the SSP analysis, where I found that the negative-gradient galaxies have, on average, lower central SSP ages than the majority of the sample. All negative gradient galaxies have SSP equivalent ages less than 3 Gyrs (5 Gyrs) within an $R_e/8$ (R_e) aperture (Figure 4.11). In the case of NGC4150, a prominent negative gradient galaxy, Crockett et al. (2011) confirm the presence of a centrally concentrated $\sim$ 300 Myr population using HST UV and visible photometry. These galaxies also tend to be dusty and contain significant amounts of molecular gas, again indicative of recent star formation. 75 per cent of negative gradient galaxies were detected in CO, compared to 18 per cent of the normal galaxies. Similarly, 71 per cent of negative gradient galaxies contained dust identified in the *ugriz* photometry, compared to only 15 per cent of the normal galaxies.

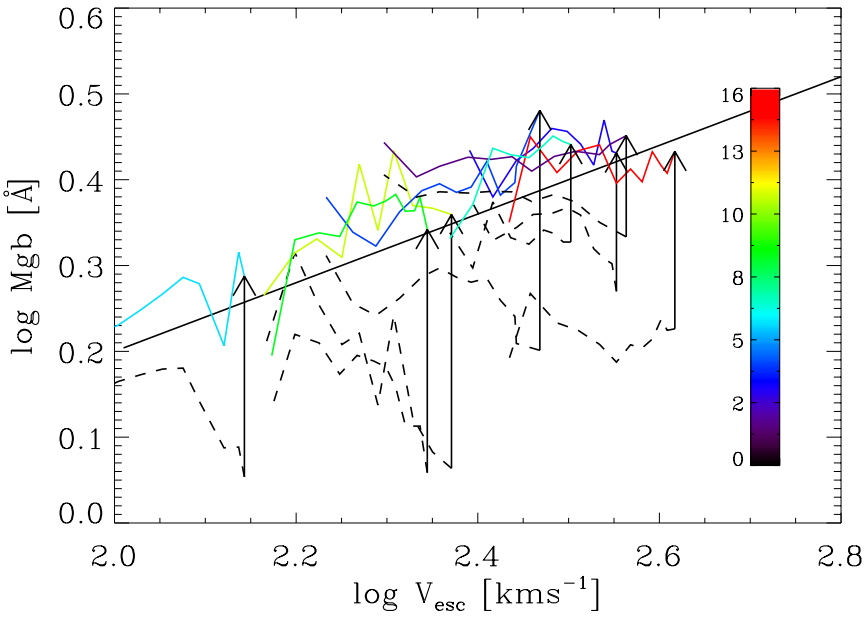

Figure 4.12: The effects of passively ageing negative gradient galaxies on the Mgb-V_{esc} relation. The technique used is fully described in the text. The dashed lines show the observed profiles and the coloured lines the profiles after passive ageing has returned them to the Mgb-V_{esc} relation (shown as the solid black line). The degree of ageing required to return a given galaxy to the relation is indicated by the colour of the profile, but is strongly dependent on the assumptions of the SSP modelling.

4.5.1 Passive ageing

These young cores typically represent a small (by mass fraction) perturbation on top of an underlying older population. As the galaxy ages and the younger population fades, reducing its contribution to the total luminosity of the galaxy, one might expect these galaxies to return to the Mgb-V_{esc} relation as the older population comes to dominate the light. I tested this idea by artificially ageing these negative gradient galaxies using the SSP models. I fixed the metallicity and alpha-enhancement of each bin to the values returned by the SSP models from the line strength observations. I then increased the age of each bin by an equal amount, and determined the new line strengths from the SSP models. From the new line strength maps I recalculated the Mgb-V_{esc} gradient for each galaxy. The ages were incremented until either the new Mgb-V_{esc} gradient was consistent with the observed global relation

or the boundary of the SSP model grids was reached.

This analysis is shown in Figure 4.12. As can be seen the negative gradient galaxies typically return to the relation after a few Gyrs of evolution, assuming no further star formation takes place. Of the 17 negative gradient galaxies in the sample, 10 returned to the Mgb-V_{esc} relation, however for 4 galaxies the gradients remained negative even after 12 Gyrs of passive artificial aging. For the remaining 3 galaxies their gradients become positive but without returning to the relation. The timescales for galaxies to return to the relation are likely shorter than those predicted by the SSP models, as the assumptions made in the SSP modelling mean the SSP ages are strongly influenced by even a small fraction of very young stars. With more sophisticated stellar population modelling, using more realistic star formation histories (for example, using a two-burst model would allow me to constrain the age and mass-fraction of the young population much more accurately) I would be able to properly test the idea that the main bulk of stars in these negative gradient galaxies do lie on the Mgb-V_{esc} relation.

4.6 The Mgb-V_{esc} relation from a dynamical perspective

In this and the previous chapter I have presented strong evidence that the Mgb-V_{esc} relation is both an empirically and physically interesting correlation to explore in the context of galaxy evolution. The global and local behaviour displayed by the Mgb-V_{esc} relation is its key improvement over other similar relations such as the Mgb-σ and mass-metallicity relations. One key question that I have not yet addressed is why the Mgb-V_{esc} relation alone displays this behaviour: why does the choice of V_{esc} on the x-axis result in this global and local connection while the related variable σ does not?

Both V_{esc} and σ are related to the mass distribution and gravitational potential

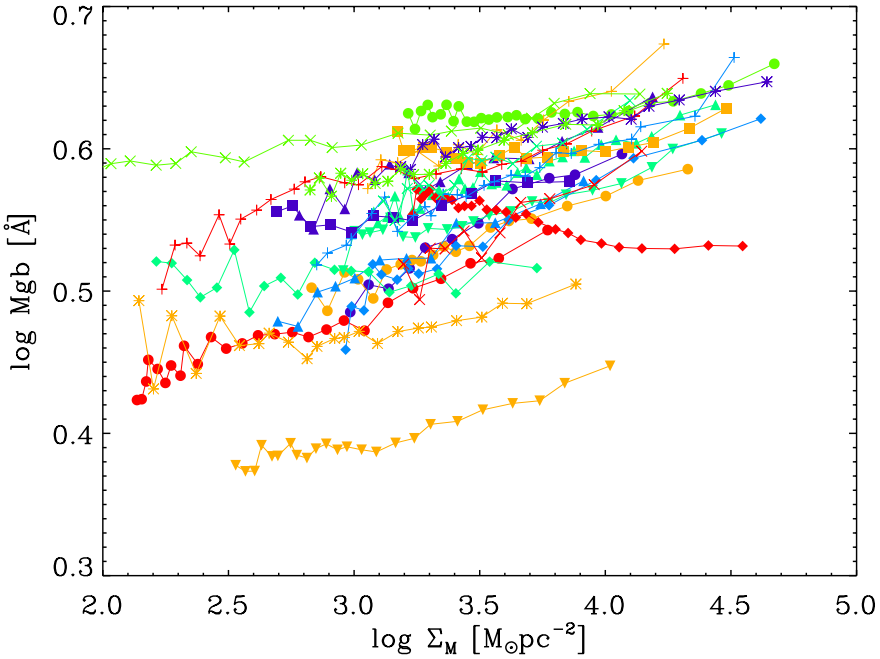

Figure 4.13: The Mgb-Σ_M relation for a subset of SAURON galaxies. Colours and symbols are as in Figure 3.2. The internal Mgb-Σ_M gradients of different galaxies are the same, however the offsets show no trend. There is a local connection between Mgb and Σ_M but no global connection.

of a galaxy. The local V_{esc} depends only on the mass distribution and is a direct measure of the gravitational potential. In contrast the local σ is less closely linked to the global mass distribution, depending also on the orbital structure. While σ produces tight global relations with Mgb and other galaxy properties these are not reproduced on the local level.

In contrast the surface mass density, Σ_M, is a dynamical variable that is purely local - Σ_M at any given point in an object has little connection to the total mass distribution of a galaxy. A point in the centre of a low-mass galaxy can have the same Σ_M as a point in the outer parts of a much more massive galaxy despite their hosts having very different masses. This local but not global behaviour is clear when we examine the Mgb-Σ_M relation, shown in Figure 4.13. Here we see local behaviour that is consistent within galaxies - the Mgb-Σ_M relation has the same slope in each object, however there is no overall relation because of the lack of a global connection.

It is interesting to ask if the local and global behaviour found in the Mgb-V_{esc} relation is unique, and given that the local and global connection breaks down with the other indices and the individual SSP parameters, is there a different combination of σ and Σ_M that does restore the connection? Fitting a plane to V_{esc}, σ and Σ_M I find:

$$\log V_{esc} = 0.642 \log \sigma + 0.118 \log \Sigma_M + 0.931, \sigma = 0.056. \quad (4.9)$$

Despite being able to find a tight relation between these variables (the scatter is 2 per cent) they do not reproduce the local and global connection of the Mgb-V_{esc} relation. This can be seen in the upper panel of Figure 4.14, where the distribution of local dlog(Mgb)/d(0.636 logσ + 0.125 logΣ_M) gradients (determined as before from a linear fit to the individual galaxy profiles) is shown with the global gradient determined from central aperture values as the dashed vertical line. The local gradients are offset to shallower values than the global gradient.

However, the local σ determined on a bin-by-bin basis may not be the correct variable to consider in this analysis. The central velocity dispersion, σ_0, is related to an object's total mass and shows a tight correlation with the central Mgb linestrength. This suggests that the combination of σ_0 as a 'global' variable and Σ_M as a 'local' variable may be better able to reproduce the global and local behaviour of the Mgb-V_{esc} relation. Fitting σ_0 and Σ_M to V_{esc} I find:

$$\log V_{esc} = 0.692 \log \sigma_0 + 0.153 \log \Sigma_M + 0.654. \quad (4.10)$$

This combination of variables does reproduce the global and local connection when plotted against Mgb. This is shown in the lower panel of Figure 4.14, where the distribution of local gradients does align with the global gradient. In Figure 4.15 I show the Mgb - σ_0 - Σ_M relation for all individual bins from the ATLAS^{3D} survey, where the contours are labelled to indicate the fraction of all bins enclosed

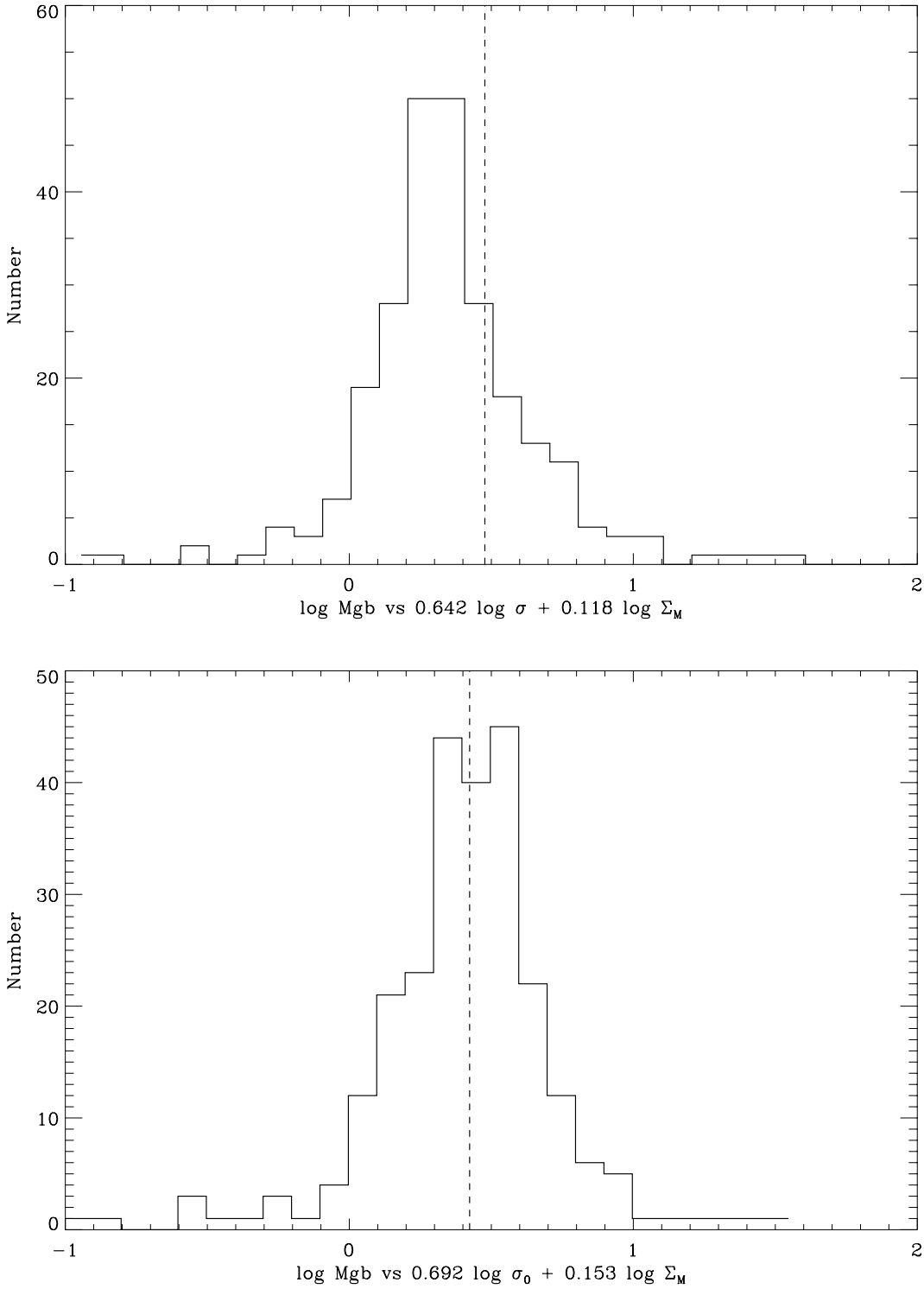

Figure 4.14: Upper panel: Histogram of individual galaxy gradients for log Mgb vs. 0.636 log σ + 0.125 log Σ_M, with the global gradient from central aperture measurements shown as the dashed vertical line. Lower panel: As upper panel except the local σ is replaced with the central σ_0 of the corresponding galaxy for each bin. When using σ the local and global connection is not reproduced - the local gradients are shallower than the global gradient. However, when using σ_0 the local and global behaviour is restored.

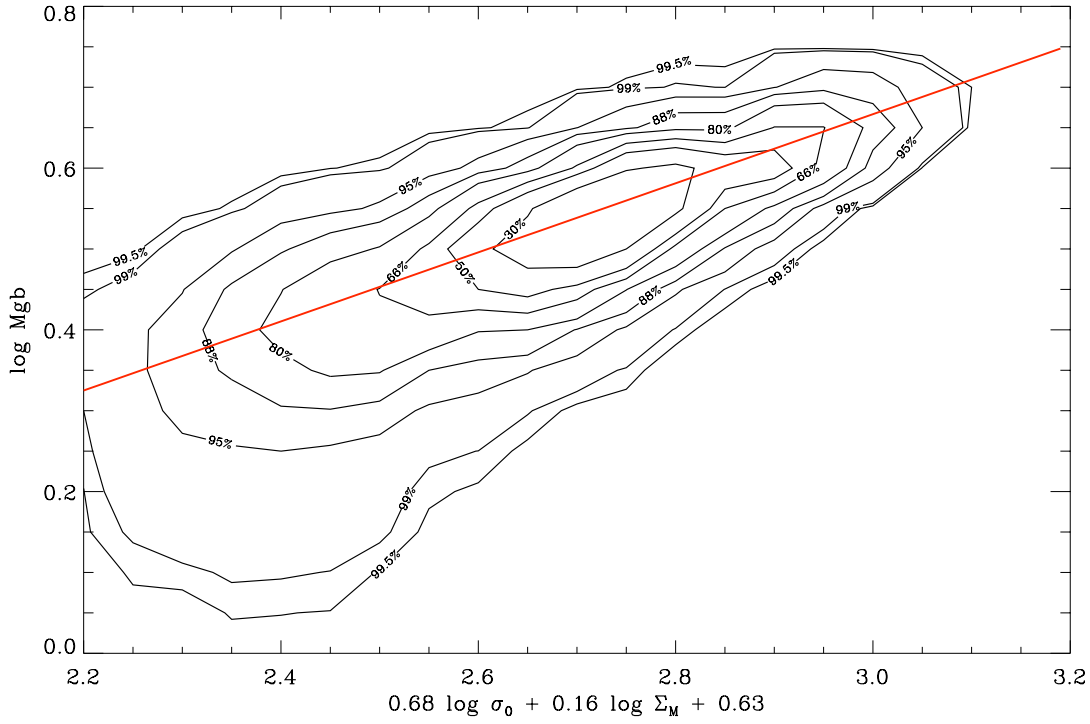

Figure 4.15: The Mgb-σ_0-Σ_M relation for all individual bins from the ATLAS^{3D} sample. The fraction of the total number of bins enclosed by a given contour is indicated on the plot. The global relation determined from central aperture measurements is shown in red.

by a given contour and the global relation determined from central aperture values is shown in red. Equation 4.10 is also consistent with the result of a planar fit to Mgb, σ_0 and Σ_M directly.

As an aside, this combination of σ_0 and Σ_M appears to serve as a proxy for V_{esc}, reproducing the key local and global connection. Σ_M can be determined from the surface brightness I and M/L, which can itself be determined from σ_0 using the relation between M/L and σ from Cappellari et al. (2006) and Scott et al. (2009). Additionally I showed in Section 4.2 that the local colour behaves similarly to Mgb in the V_{esc} relations. All three of these quantities, σ_0, I and the local colour can be determined for galaxies at higher redshifts than those accessible to high S/N IFU observations, potentially allowing the local and global behaviour to be studied out to cosmologically significant redshifts.

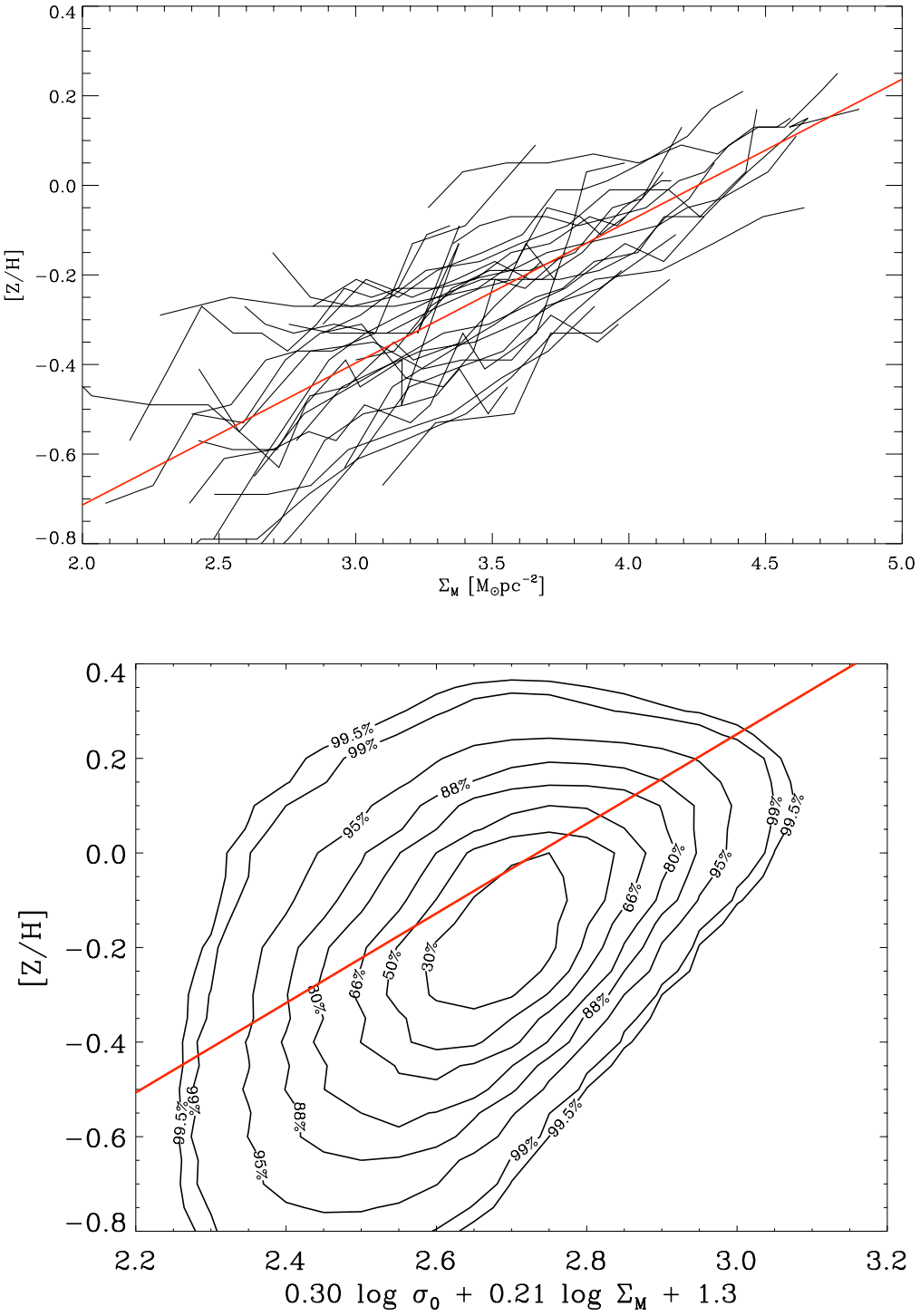

Figure 4.16: Upper panel: The [Z/H]-Σ_M relation for a subset of ATLAS^{3D} galaxies, with the global relation shown in red. Lower panel: contour plot showing the distribution of individual bins in the [Z/H] - σ_0-Σ_M plane. Each contour is labeled with the fraction of points it encloses. The global relation is shown in red and is shallower than the distribution of individual bins.

Having established σ_0-Σ_M as an alternative to V_{esc} in the Mgb-V_{esc} relation, can it perform the same role with any of the SSP-V_{esc} relations? In particular, the [Z/H]-V_{esc} relation shows a tight correlation globally and a narrow distribution of local gradients, though one that is offset from the global gradient. [Z/H] also correlates with Σ_M, however, the local gradients are shallower than the global gradient. This is shown in the upper panel of Figure 4.16 for a subset of ATLAS^{3D} galaxies. The combination of σ_0 and Σ_M given in Equation 4.10 functions essentially like V_{esc} so a different combination of these variables needs to be considered. A planar fit to [Z/H], σ_0 and Σ_M gives:

$$[\mathrm{Z/H}] = 0.305 \log \sigma_0 + 0.215 \log \Sigma_M - 1.620. \tag{4.11}$$

In the lower panel of Figure 4.16 I show the [Z/H]-σ-Σ_M relation for all individual bins from the ATLAS^{3D} survey, with the global relation overplotted in red. The distribution of individual bins is steeper than the global relation. Though this is the combination of σ_0 and Σ_M that has the smallest scatter against [Z/H] it does not reproduce the global and local connection; Mgb remains unique in showing this behaviour. No combination of σ_0 (or σ) and Σ_M reproduces the local and global behaviour for any of the indices or SSP parameters other than Mgb.

4.7 The Mgb-V_{esc} relation from a stellar population perspective

Having addressed the x-axis of the Mgb-V_{esc} relation in the previous section I now turn to the y-axis. Of the three Lick absorption indices in the SAURON spectral range it is only Mgb that exhibits the local and global behaviour; Fe5015 and Hβ do not (see Section 3.4.3). Fe5015 is a complicated index suffering from contamination by a nearby TiO molecular absorption feature and so is difficult to interpret. Hβ

is expected to behave differently from Mgb as it is predominantly an age indicator, whereas the other indices are more closely related to the metallicity. With only three indices available it is difficult to draw any firm conclusions. More significantly, the SSP-equivalent age, metallicity and alpha-enhancement also do not show this local and global connection. Is it coincidence that the particular relationship between t, [Z/H] and [α/Fe] that gives rise to the observed Mgb index does behave in this way, or is some fundamental process in ETG evolution determining the relation?

In Section 3.5 I determined a relationship between V_{esc}, [Z/H] and t that does reproduce the local and global behaviour of the Mgb-V_{esc} relation. It is interesting to ask if this relation is consistent with the observed Index-V_{esc} relations, in the sense that if I use the SSP models of Schiavon (2007) to express the SSP-V_{esc} relation as a constraint on the observed indices, are the observed relations reproduced? As the SSP-V_{esc} relation only constrains two of the three SSP parameters I imposed the additional constraint that [α/Fe] = 0.33, the mean value for the SAURON sample. This analysis is shown in Figure 4.17, where the index values allowed for a given V_{esc} are shown as the black diamonds, with lines of constant t and [Z/H] shown in red and blue respectively. The observed relations are shown in green. In the lower panel the region occupied by the observations is highlighted in grey.

By design the Mgb-V_{esc} relation produced in this way tightly follows the observations. In the case of Hβ the region allowed by the model (the grid of points) is well matched to the region occupied by the observations (shaded area). The regions at high and low V_{esc} predicted to be occupied by the models but lacking observed datapoints is likely due to the selection of the sample. The upper area where no observed datapoints are found is due to the fact that we do not find young, metal-rich galaxies in the sample, despite these being allowed by the SSP-V_{esc} constraint. Variations in t or [Z/H] alone move an object away from the relation, rather than along it as is the case with Mgb. In the case of Fe5015 the model predicts a tight correlation with V_{esc} but one that is somewhat steeper than the observed relation.

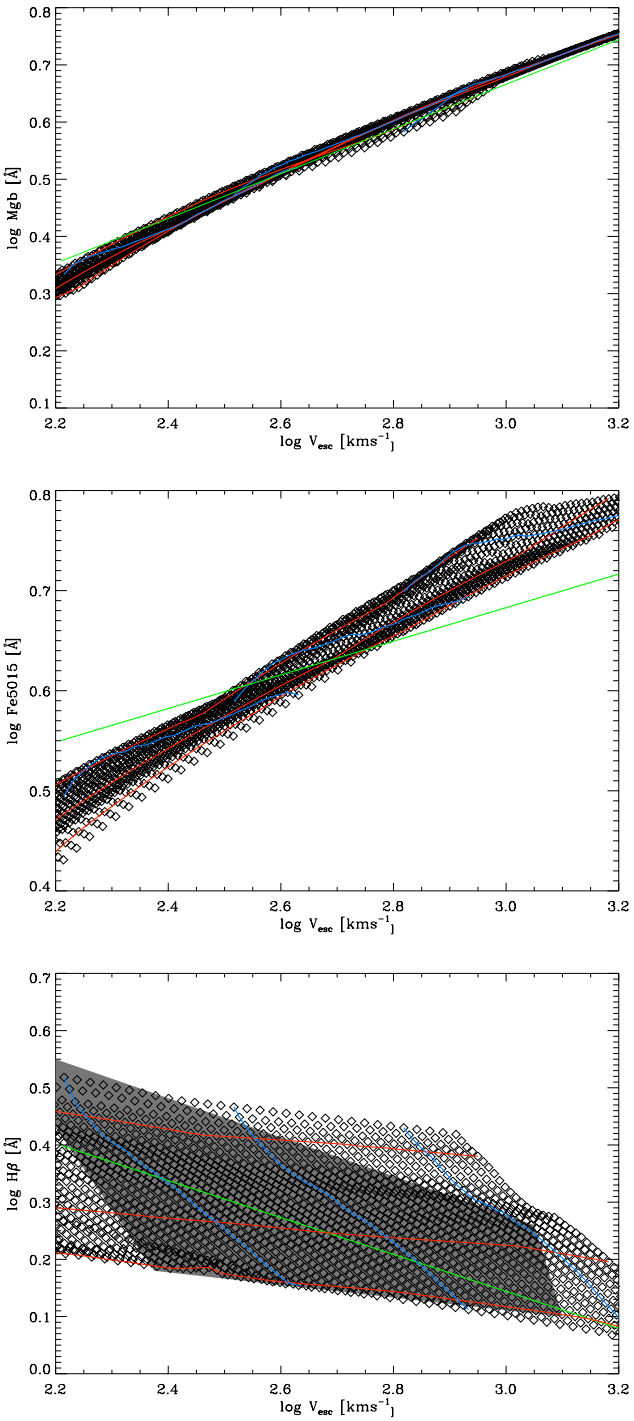

Figure 4.17: The Index-V_{esc} relations predicted by inverting the SSP models of Schiavon (2007) and applying the constraint of Equation 3.12 at constant $[\alpha/\mathrm{Fe}] = 0.33$. The grid of points show the predictions of the SSP model in each panel. The green line is the best fit to the observations from Section 3.4. The red and blue lines show lines of constant metallicity and age respectively. In the lower panel the grey shaded area indicates the approximate region occupied by the observations. With these constraints the SSP model is able to reproduce the observed Mgb and Hβ-V_{esc} relations, however the condition of fixed $[\alpha/\mathrm{Fe}]$ must be relaxed to reproduce the Fe5015-V_{esc} relation.

Allowing other values of [α/Fe] is required to match the observations; this is consistent with the SSP hyperplane having a small thickness. At low V_{esc} high values of [α/Fe] would be required to match the observations, whereas at high V_{esc} Fe would need to be enhanced relative to Mgb. It is clear that my SSP-V_{esc} analysis is consistent with the observed relations, however this does not bring us any closer to answering the question of whether the Mgb-V_{esc} relation is a coincidental one or arises from a fundamental process occurring in galaxy evolution.

One way to approach this issue is to examine which of the SSP parameters is driving the Mgb-V_{esc} relation. This is addressed in Figure 4.18, where the Mgb-V_{esc} relation is shown for a subset of all bins from the IFU observations of the ATLAS^{3D} sample with a fixed value of each of the SSP parameters. The coloured contours show the location of all IFU bins of a given t, [Z/H] or [α/Fe] in the Mgb-V_{esc} plane, with the solid line of the same colour showing the best fit to each subset of IFU bins. When binning by t or [α/Fe] I find that, except for the very youngest or α-deficient bins, all bins follow the Mgb-V_{esc} relation within the 1 σ errors. Bins at fixed t or [α/Fe] span the full range in V_{esc} of the sample, again except for the youngest bins. All bins with t $<$ 1.2 Gyrs lie below the relation; they are also only found at low V_{esc}, consistent with my findings for negative-gradients galaxies in Section 4.5. Bins with t $<$ 2.2 Gyrs also lie below the relation, though at higher V_{esc} this effect is less pronounced. All bins with t $>$ 2.2 Gyrs follow the Mgb-V_{esc} relation, even at $V_{esc} < 400 \mathrm{kms}^{-1}$. When binning by α, only bins with [α/Fe] < -0.06 show any significant deviations from the Mgb-V_{esc} relation, again only apparent at $V_{esc} < 400 \mathrm{kms}^{-1}$. There is a small but significant trend for the relation to be offset to higher values of Mgb as [α/Fe] increases. This picture is consistent with the results of the dependence of the residuals from the relation on the SSP parameters in Section 4.4.3.

The picture is very different when binning by [Z/H]. Bins of fixed [Z/H] only span a narrow range in V_{esc}. The low-[Z/H] bins are concentrated at low V_{esc} and lie below

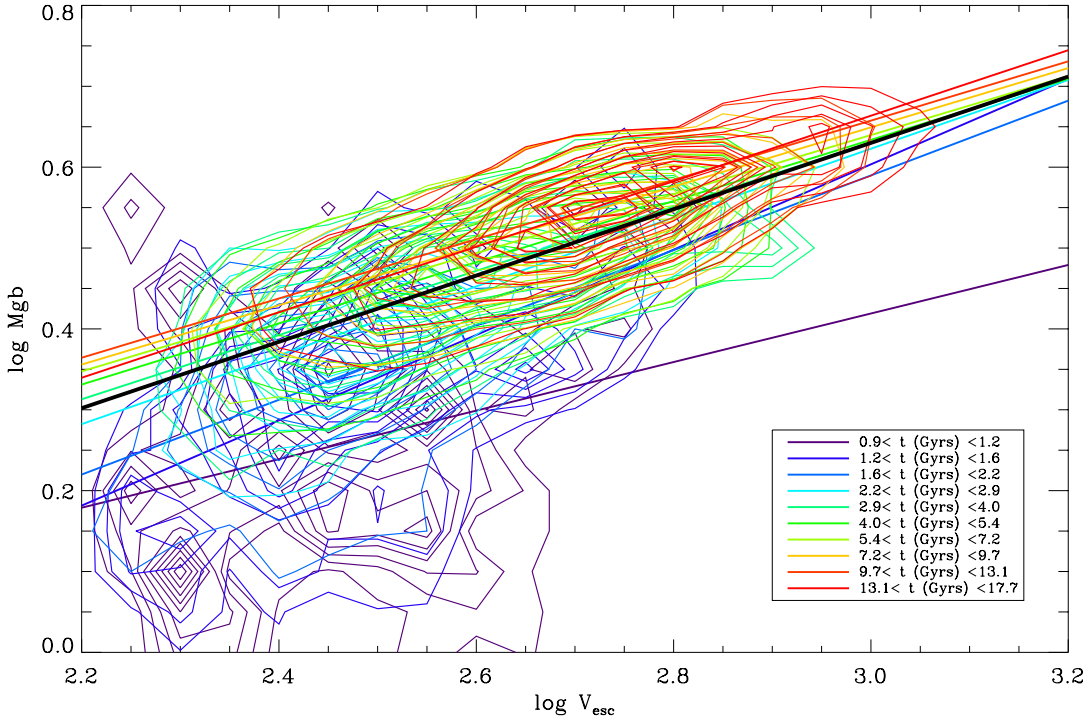

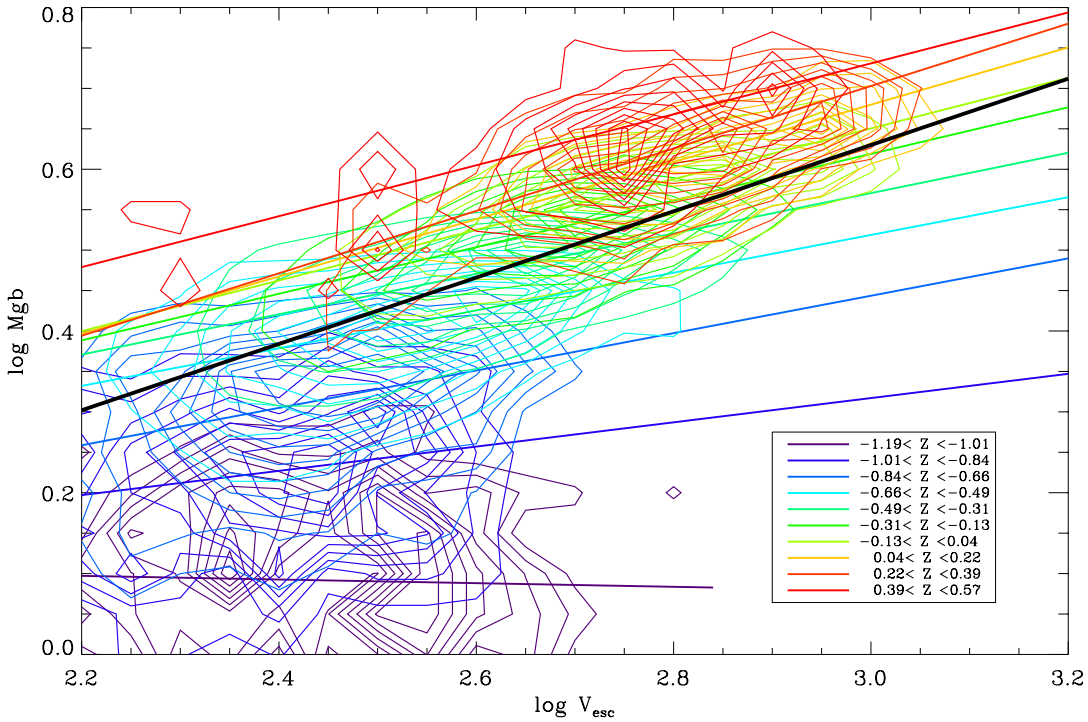

Figure 4.18 (Continued below)

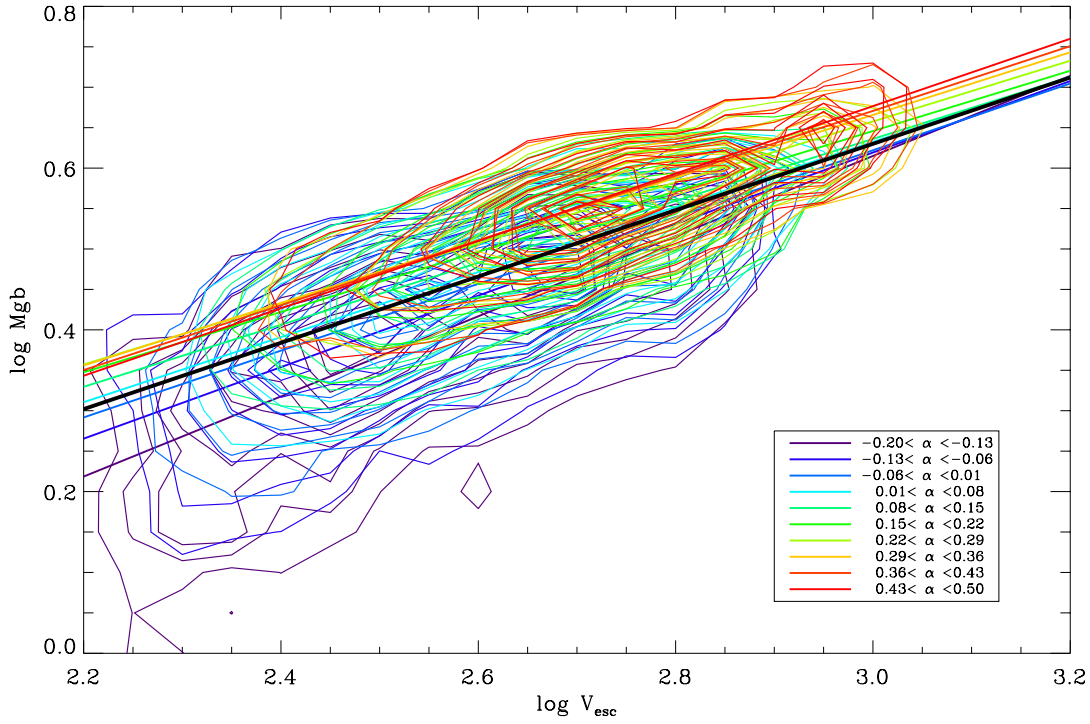

Figure 4.18: The Mgb-V_{esc} relation for all individual bins, divided into separate samples of constant age (upper panel), metallicity (middle panel) and α enhancement (lower panel). The coloured contours indicate the region occupied by the points with a given value of t, [Z/H] or [α/Fe]. The solid black line shows the global relation for all galaxies while the coloured lines are a fit to the fixed SSP subsets. The SSP values indicated by each colour are shown on the colour bar on each panel. The negative gradient galaxies stand out clearly at young ages and low metallicities. The relation shows the strongest dependence on [Z/H].

the Mgb-V_{esc} relation, in the region occupied by the negative gradient galaxies. The high-[Z/H] bins are concentrated at high V_{esc} and lie above the main Mgb-V_{esc} relation. When [Z/H] is fixed, the Mgb-V_{esc} relation disappears; for any fixed [Z/H] the relation is always shallower than the observed Mgb-V_{esc} relation. This is not surprising, given that the strength of the Mgb absorption index is predominantly determined by [Z/H], and so Mgb can vary little at fixed [Z/H]. The Mgb-V_{esc} relation is predominantly driven by the variation of [Z/H] with V_{esc}, which is again unsurprising given the tight mass-metallicity relation.

The mass-metallicity relation alone is not enough to explain the global and local behaviour of the Mgb-V_{esc} relation. The [Z/H]-V_{esc} relation does show a tight cor-

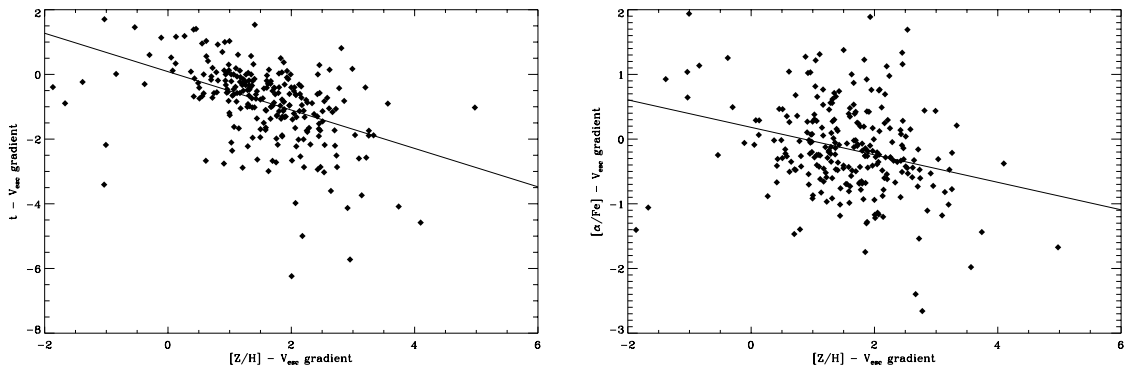

Figure 4.19: Anticorrelation of the [Z/H]-V_{esc} gradient with the t- and [α/Fe]-V_{esc} gradients. Solid lines are robust linear fits to all points.

relation between the two variables, however it does not show the local and global behaviour. When considering a combination of [Z/H] and t the scatter is reduced and the global and local behaviour reappears. The [Z/H]-V_{esc} gradients of individual galaxies are typically steeper than the global gradient, but combining this with t or α weakens the internal gradients to align with the global gradient. Plotting dZ/dlog(V_{esc}) against dlog(t)/dlog(V_{esc}) and dα/dlog(V_{esc}) in Figure 4.19, I found that the [Z/H]-V_{esc} gradients are anticorrelated with both the t-V_{esc} and [α/Fe]-V_{esc} gradients. It is this anticorrelation that leads to the weakening of individual galaxy gradients and restoration of the global and local connection in the SSP-V_{esc} relation.

Recognising that the SSP-V_{esc} relation arises from the anticorrelation of the gradients provides an important insight into the nature of the SSP-V_{esc} relation, however the most important question about the Mgb-V_{esc} and SSP-V_{esc} relations remains unanswered: what is the connection to the physical processes of galaxy formation? Three possibilities exist: first the unique global and local behaviour of the relations could be coincidence, a particular edge-on view of a higher-dimensional surface that really defines the behaviour of ETGs. Alternatively, the Mgb-V_{esc} relation could indicate a true physical connection between the SSP parameters and V_{esc}, however the true relationship is confused by the SSP modelling process and a simple connection between, for example, metallicity and V_{esc} exists. Finally, it may

be that the SSP-V_{esc} relation found in this work is the true physical relationship between the local gravitational potential and the stellar populations in ETGs and the relation is a fundamental property of the galaxy formation process. The existence of the Colour-V_{esc} relations suggests that something more significant than a coincidental projection is occurring, however further testing of the Mgb-V_{esc} relation is needed before this question can be answered. This testing should proceed in two principal directions: detailed hydrodynamical modelling of ETGs in a cosmological context and improved stellar population observations and modelling. The necessary ingredients (cosmological volumes, star formation and stellar population modelling, spatially resolved information on individual objects) exist for the hydrodynamical simulations to explore the Mgb-V_{esc} relation, however no single study has combined them all to examine internal absorption linestrength index gradients.

The most obvious (but probably most challenging) approach is to improve the stellar population models used to convert the observed indices to SSP equivalent parameters. Stellar population modelling is complex and draws from many areas of astrophysics, particularly the modelling of stellar atmospheres and the observations of large samples of high-resolution template spectra to calibrate the models. These template spectra are typically drawn from stars in the Solar neighbourhood, which have very different chemical compositions from that expected in ETGs. Some SSP models use synthetic template spectra to account for the expected alpha-enhancement, however they do not account for the chemical abundance patterns in detail. Improving this aspect of the stellar population models may allow us to disentangle which of the SSP equivalent parameters really drives the Mgb-V_{esc} relation.

The other option is to use alternate indices or different techniques to independently verify the SSP-V_{esc} relation. Increasing the number of Lick indices used in the SSP modelling will help to further constrain the models, particularly by adding in additional Fe lines that will better constrain the metallicity. I have observed a subset of SAURON galaxies with the Intermediate Dispersion Spectrograph (IDS)

on the INT telescope on La Palma, with a wavelength range of $\sim 3700 - 6900$ Å, including many more Lick indices (particularly Fe5270, Fe5335, Hγ, Hδ, NaD, and Ca4227) than the SAURON spectral range. The reduction and analysis of this data is ongoing but, when completed, will better constrain t, [Z/H] and [α/Fe] for a sample of 26 galaxies with measured V_{esc}. Using other SSP modelling techniques such as SED fitting will also provide an independent constraint, however the age-metallicity degeneracy is more pronounced with this technique than with Lick index fitting. The ideal solution would be to directly measure the resolved stellar populations of nearby ETGs, however this will not be possible for SAURON and ATLAS^{3D} galaxies until the advent of the next generation of Extremely Large Telescopes (ELTs).

4.8 Discussion

If, as I have argued above, the Mgb-V_{esc} relation does reveal a physically interesting connection in ETG formation the next stage is to understand how to exploit the relation to further our understanding of galaxy evolution. This can be achieved through two very different approaches: using the relation in a purely empirical way and using simulations to test how the relation could be put in place and evolve under different conditions. Having established the Mgb-V_{esc} relation as a tight observable correlation in the majority of ETGs, simply observing variations in the relation with different galaxy properties can reveal what parameters affect galaxy evolution, though not what physical process leads to a particular effect. There are several examples of this approach in this chapter including the variation of the Mgb-V_{esc} relation with environment and with molecular gas content and the breakdown of the relation for young stellar populations. Studying the relation in a broader range of environments, particularly high-density environments (as the Virgo cluster, the highest density environment in the ATLAS^{3D} is less dense than many other clusters) is important to confirm the environmental dependence found in this study. Studying

the redshift evolution of the relation would also be interesting, though determining V_{esc} for a sufficiently large sample of galaxies at higher redshifts is an observationally intensive task.

4.8.1 Hierarchical assembly

What effect will major mergers have on the Mgb-V_{esc} relation? In the ΛCDM paradigm massive ETGs are predominantly formed by hierarchical assembly; merging less massive galaxies together. Taking an extreme example, if two completely gas free, equal mass ETGs that both initially lie on the observed Mgb-V_{esc} relation merge, would one expect the resulting merger remnant to lie on the Mgb-V_{esc} relation? A naive initial answer would suggest no; by merging the two galaxies the mass distribution and hence the gravitational potential are significantly altered while the stellar population remains unchanged as there is no gas to form new stars. If this simple analysis is valid then it is possible to constrain the number of major, dry mergers a typical ETG has experienced using the observed intrinsic scatter of the Mgb-V_{esc} relation. However, the picture may be considerably more complicated than this simple analysis allows for, even in the case of a dry major merger. While the global potential of the galaxy must deepen as more mass is added, it is less clear how much, if at all, the local potential and individual star inhabits will be changed.. In support of this idea it has long been shown that the rank order of binding energies of the stars is preserved in a collissionless merger (White & Rees, 1978; Barnes, 1988).

A simple analytical model can be used to estimate what happens to V_{esc} during a 1:1 mass ratio major merger. The potential will change due to changes in the final mass and radius and due to the redistribution of the stellar material due to violent relaxation. Following a simple Virial estimate as in Naab et al. (2009) it can be shown that:

$$\frac{r_f}{r_i} = \frac{(1+\eta)}{(1+\eta\epsilon)}$$

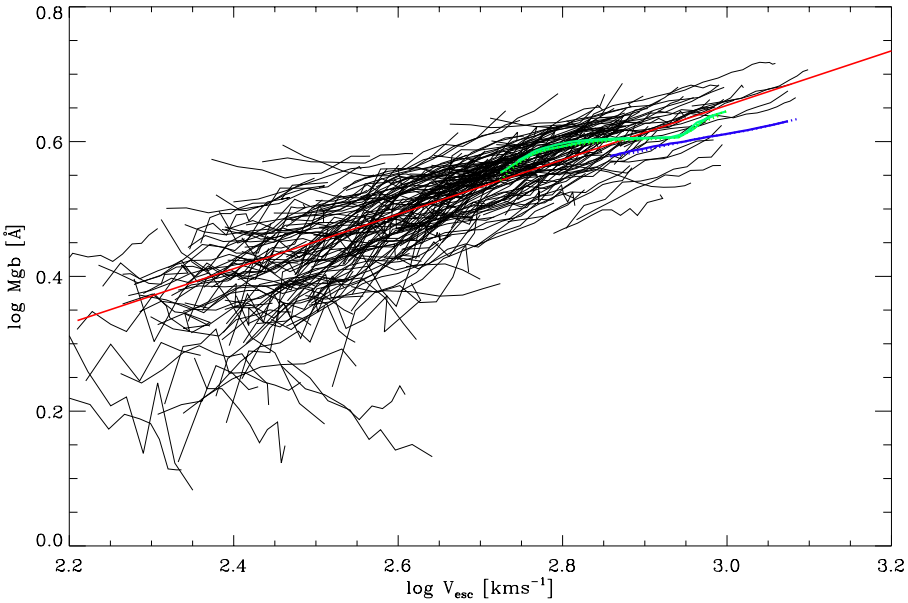

Figure 4.20: Effect of binary mergers on the Mgb-V_{esc} relation. The black lines show the data from the ATLAS^{3D} survey, with the best fitting central relation shown in red. The green lines show the Mgb-V_{esc} relation for the progenitor galaxies in the N-body simulation, 'observed' exactly as the data. The blue line shows the Mgb-V_{esc} relation for the merger remnant. The gradient and Mgb values remain unchanged however the merger remnant is shifted to higher V_{esc}

where the subscripts i and f denote initial and final quantities, η is the mass ratio of the merger, $\eta = M_f/M_i$ and ϵ is the ratio between the accreted and initial mean square speed, $\epsilon = \langle v_a^2 \rangle \,/\, \langle v_i^2 \rangle$. If the two progenitors are identical ($\eta = 2, \epsilon = 1$) there would be no change in radius but the mass of the remnant will double. This leads to a change in V_{esc} of:

$$\Delta V_{esc} = \frac{V_{esc,f}}{V_{esc,i}} \propto \left(\frac{r_i}{r_f} \frac{M_f}{M_i} \right)^{1/2} \propto \sqrt{\eta}.$$

For a 1:1 major merger this analytic estimate predicts V_{esc} will increase by a factor $\sqrt{2}$, or a shift of 0.15 in log V_{esc}. If the relaxation is not complete (Barnes, 1988; Hopkins et al., 2009) there will also be a change in the binding energy or final radii, affecting the change in V_{esc}.

Moving beyond the simple arguments outlined above requires the use of more

sophisticated modelling techniques, such as N-body simulations of major merger events. In collaboration with Maxime Bois as part of the ATLAS^{3D} project I have compared the results of such a simulation to the observed Mgb-V_{esc} relation. The simulation is fully described in Bois et al. (2010) and Bois et al. (in press). The results of the simulation are shown in Figure 4.20. The progenitors are shown in green, with the corresponding remnant shown in blue. The black lines show the observed ATLAS^{3D} sample and the solid red line is the best fitting observed relation as described in Section 3.4. The dry merger simulations confirm the naive prediction that Mgb remains essentially unchanged while the merger remnants are shifted to higher V_{esc} by an amount $\sim \Delta \log V_{esc} = 0.08$. This is broadly consistent with the analytic argument presented above.

The Mgb-V_{esc} gradients are largely preserved in the merger, in that the gradient of the remnant is the average of the progenitors' gradients. It is clear that dry major mergers move galaxies to the right of the relation, rather than along the relation. From this result two conclusions can be drawn. Firstly, massive ETGs cannot have been formed by dry major mergers of less massive present-day ETGs. To take a galaxy from the bottom left of the Mgb-V_{esc} diagram to the right side requires an increase in its $V_{esc,e}$ by ~ 0.4 due to major mergers. With no corresponding change in its Mgb_e, this hypothetical galaxy would have a value of log Mgb $\sim 3\sigma$ below the relation. Secondly, the observed scatter in the Mgb-V_{esc} relation can be used to constrain the number of major dry mergers a typical early-type galaxy can have undergone. Given an observed scatter in log Mgb of $\sigma = 0.04$ (corresponding to $\sigma = 0.12$ in V_{esc}), and a typical $\Delta \log V_{esc}$ of 0.08 per merger (from the simulation), a typical ETG can have experienced at most ~ 1.5 major dry mergers before destroying the relation, assuming zero intrinsic scatter. If the zero order relation, that followed by galaxies without any merging, has a non-zero intrinsic scatter, or other effects increase the scatter in the relation (e.g. minor mergers, environmental effects) then fewer mergers can be accommodated by the observed scatter. If the

relation was different (or not in place at all) at the typical formation redshifts of massive ETGs, around z $\sim$ 2, then the Mgb-V_{esc} relation observed locally cannot be used to constrain the typical number of mergers. Observing the evolution of the relation with redshift would be a significant constraint on the influence of mergers on ETGs. It is clear from the simulations that merging will always increase the scatter in the Mgb-V_{esc} relation, therefore the small observed scatter in the relation provides a significant challenge to a merger-driven scenario of galaxy formation. The small scatter suggests that most of the stars in local ETGs were formed in the galaxy when it was substantially the same mass as it is now. This result is consistent with the observations of high-redshift quasars (Fan et al., 2001a), which indicate the presence of supermassive black holes likely hosted by massive galaxies.

4.8.2 The wider context of galaxy evolution

From the above discussion and analysis it is clear that dry merging cannot have put the relation in place, therefore star formation of some form, triggered or otherwise, must be the underlying physical process that leads to the correlation of Mgb with V_{esc}. It is the star formation history of an object that establishes the properties of its stellar population, hence the Mgb-V_{esc} relation must indicate a connection between the SFH and the depth of the local gravitational potential. However, under the hierarchical assembly paradigm, the potential that we observe a galaxy in today may not be the potential that it was formed in. The dynamical formation of the galaxy happens at a later time than the typical formation epoch of the majority of the stars. A massive ETG is dynamically formed from pre-formed stellar constituents. However, again recognising the result of Barnes (1988) it is possible that the potential a star forms in does have a connection to the one we observe it in today. Even with this caveat, it is difficult to see how stars formed in entirely non-interacting halos of potentially very different masses that only merged at a much later time could be so tightly related to the final potential.

An alternative hypothesis to hierarchical assembly is that massive ETGs form predominantly in a single extended collapse and star formation episode. This scenario is known as monolithic collapse. In this scenario the dynamical formation of a galaxy occurs at the same time the stars are formed, hence the potential we observe a star in today *is* the potential it was born in (to a good approximation). The correlation of Mgb with V_{esc} in a monolithic collapse scenario has been studied by Pipino et al. (2010) and they find they are able to reproduce the observed Mgb-V_{esc} relation naturally in their chemical evolution models. While it is unlikely that real galaxies formed in a purely monolithic collapse, as massive ETGs typically formed at high redshift their formation may have been 'monolithic collapse-like'. By this I mean that even though they may have experienced multiple separate accretion and star formation episodes they must all have occurred in a relatively short period of time as the Universe was only a few Gyrs old at their formation redshift. This will result in the multiple episodes being well-approximated by a single extended formation episode, hence a monolithic collapse-like scenario. This is a similar scenario to that proposed for the formation of ETGs in rich clusters by Bower et al. (1998), based on the scatter of the colour-magnitude diagram.

The connection between the local gravitational potential and the stellar populations of local ETGs is only a problem if the stars formed in a potential different to the one they reside in today. Monolithic collapse is one scenario which avoids this issue, however it is not the only one. If the majority of an ETG's stellar mass forms in-situ (as opposed to being accreted), then a connection between stellar population properties and the local potential is also not surprising. This in-situ star formation can occur at early times (similar to monolithic collapse) or at late times due to cold accretion or due to triggered star formation in a gas-rich merger. Naab et al. (2007) have used cosmological simulations to study the fraction of a typical ETG's stellar mass that is formed in-situ compared to that which has been accreted, and find that for low mass ETGs, approximately 50 per cent of their stellar mass is formed in-situ,

falling to only 20 per cent for more massive ETGs. These findings are consistent with Khochfar & Silk (2006), who, using Semi-Analytic Models also find a fraction of 20 per cent of stellar mass is formed in-situ. This suggests that the majority of a typical ETG's stellar mass was formed in a potential different to the one we observe it in today, which is challenging to reconcile with the observed Mgb-V_{esc} relation.

Chapter 5

IFU Observations of Early-Type Galaxies in the Coma Cluster

5.1 Outline

In this section I describe the observation and data reduction of a sample of ETGs in the Coma cluster, the closest rich cluster in the nearby Universe. I first describe the SWIFT IFU, the instrument used to carry out the spectroscopic observations. I then outline the criteria used to select the sample and some of the basic properties of the chosen galaxies. The data reduction is described in detail, with particular focus on the wavelength calibration and sky subtraction steps. From the reduced IFU data I extract spatially resolved kinematics, both velocity and velocity dispersion, for all galaxies. The final v and σ maps are presented at the end of this chapter.

5.2 The SWIFT IFU

The integral field observations were carried out on the Oxford Short Wavelength Integral Field specTrograph (SWIFT) IFU (Tecza et al., 2006) at the 200" Hale Telescope at the Mount Palomar observatory in California. The observations were carried out over two runs on the 3rd and 4th of May 2009 and the 25th and 26th

March 2010. One additional galaxy was observed on the 5th June 2010. Details of the two runs are given in Table 5.1. SWIFT is an IFU operating in the i- and z-bands with a spectral range from 0.63-1.05 μm and instrumental resolution $\sim$ 1 Å ($\sim$ 30 kms^{-1}). The instrument is based on the image-slicing principal, with 22 image slices or 'slitlets' on each of two CCDs, known as the 'master' and 'slave'. Each CCD has a somewhat different wavelength response, with the master being on average 20 per cent more sensitive across all wavelengths. Other than the differing sensitivities the two CCDs are identical and function independently when acquiring data. Data from the two CCDs is combined into a full data cube in the data reduction process (see Section 5.5.2). For my observations I selected the largest available field of view of the instrument, 10 x 22 arcseconds, with a corresponding spatial scale of 0.235 arcseconds pixel^{-1}. SWIFT is a high-throughput instrument; the total throughput of the telescope, adaptive optics, instrument and atmospheric transmission profile is $\sim$ 40 per cent around 8500 Å, falling to $\sim$ 20 per cent at the limits of the spectral range. SWIFT is an ideal instrument to use to measure the kinematics of low redshift ETGs because of its high throughput, relatively large field-of-view and substantial wavelength coverage which includes several absorption and emission features, particularly the Calcium Triplet (CaT) at $\sim$ 8500 Å.

5.3 Sample Selection

Because of the limited amount of observing time available to use the SWIFT IFU at the Hale Telescope I was unable to observe all ETGs in the Coma cluster. Despite SWIFT's high efficiency IFU observations require significant amounts of time per object as the light is dispersed both spatially and spectrally and, for large, nearby objects like Coma cluster ETGs, only single objects can be observed in any given exposure. Several approaches are possible in selecting a sub-sample of galaxies from the full cluster sample, and the sample selection criteria must be carefully chosen

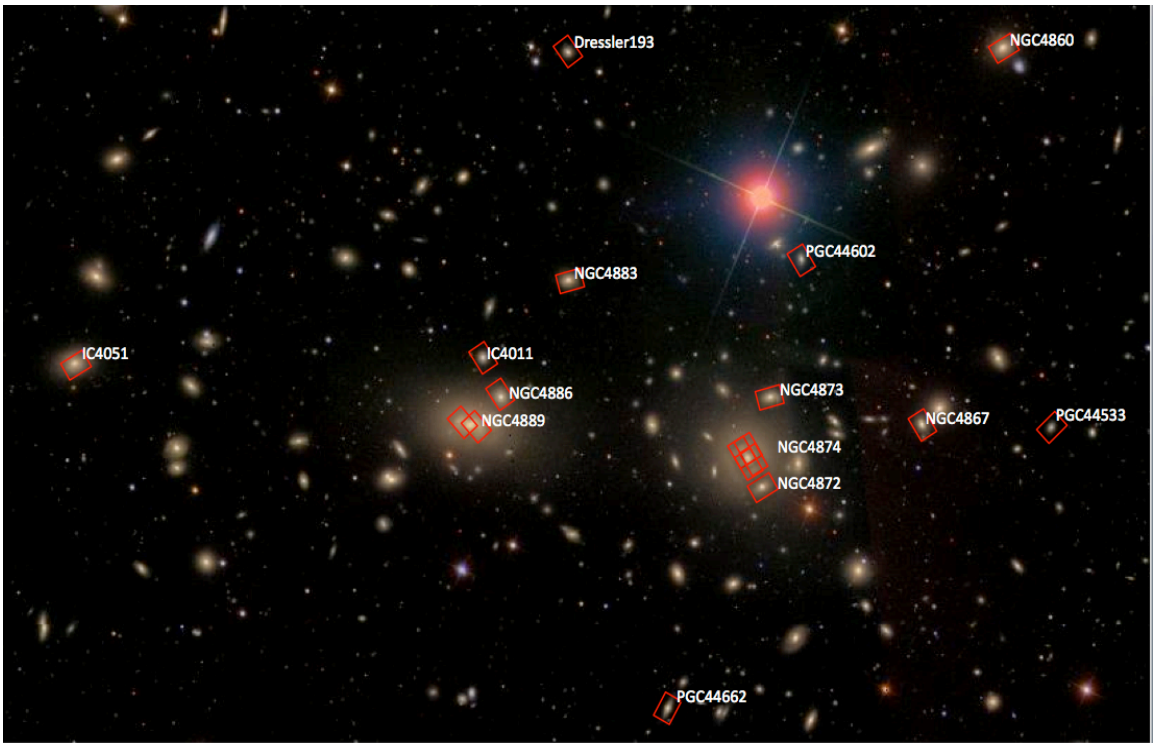

Figure 5.1: SDSS *gri* colour image of the Coma cluster. The SWIFT pointings are indicated in red, with the galaxy names indicated in white. The extent of the image is $\sim$ 30 by 40 arcminutes across.

to best serve the science goals of the survey. The two principal goals of this study (described in detail in the following chapter) are to study the Fundamental Plane and to characterise the specific angular momentum distribution of galaxies in a high-density environment. In the following paragraphs I will briefly discuss several alternative observing strategies and how these complement the science goals. The telescope time available allowed me to observe $\sim$15 galaxies. The catalogue of Scodeggio et al. (1998) contains 109 ETGs belonging to the Coma cluster.

Table 5.1: SWIFT observing runs

Run Number	Dates	Galaxies Observed	Notes
1	03/05/09 - 04/05/09	7	Substantial light leak
2	25/03/10 - 26/03/10	6	Ar arc lamp calibrations only
3	05/06/10	1	160 mas scale used

5.3.1 Sample selection methodology

One common approach is to observe all objects brighter (or more massive) than a given absolute luminosity (or mass) threshold. This threshold is chosen based on the observing time available; the number of objects above the threshold times the observing time required for each object should be equal to the total available observing time. This approach has the advantage that the sample selected is complete above the chosen threshold, allowing statistical analysis and comparison to cosmological simulations. The disadvantage of this approach is that only high-mass galaxies are observed and no information is obtained on low- and intermediate-mass galaxies which dominate the mass function of the cluster. The distribution of the observed sample is very different to that of the full cluster. This approach has severe limitations when studying the FP as it samples only a very narrow range in velocity dispersion leading to large errors in the determination of FP parameters.

An alternate approach is to match the luminosity (or mass) function of the sample to that of the cluster. If the cluster contains two hundred faint galaxies and one hundred bright galaxies the observed sample should preserve this proportion by observing, for example, twenty faint galaxies and ten bright galaxies. The principal advantage of this approach is that the observed sample should be representative of the galaxy population of the entire cluster and that the full range of luminosities (or masses) is sampled. The disadvantage of this approach is that the luminosity function is heavily dominated by faint, low velocity dispersion galaxies. Given the relatively small fraction of ETGs able to be observed in the cluster this would lead to a sample containing very few high mass galaxies. This would again result in the range of velocity dispersions being poorly sampled giving a poor determination of the FP. Additionally I expect that slow rotating galaxies, which only make up a small fraction of the ETG population, are predominantly found at higher masses so in order to explore the FR/SR fraction a reasonable number of high-mass galaxies are required.

The third approach is to evenly sample the range of galaxy masses or luminosities found in the cluster. In this approach the full range of masses is divided into several logarithmically spaced bins in mass and an equal number of objects is chosen from each bin. The advantage of this approach is that the range of velocity dispersions is well sampled, leading to the most robust determination of the FP, given the potentially available data. This sample selection also provides some leverage to probe the FR/SR fraction providing information on both high- and low-mass galaxies. The disadvantage is that the sample is not representative of the distribution of ETG properties in the cluster, having a disproportionate number of high-mass galaxies. However, because this sample provides information across the full range of masses it is possible to infer the distribution of properties across the full cluster. The main caveat to this statement is that the uncertainty in inferred properties will be a function of mass as the sample will be more incomplete at low masses than at high masses. It is this approach that I used to select the sample of ETGs for observation with SWIFT.

5.3.2 The sample

Having decided on the approach to selecting the sample I now describe the sample selection criteria and the resulting sample of galaxies selected for observation. I opted to use central velocity dispersion to select the sample, which is a reasonable proxy for mass. Mass is a derived quantity, not a directly observed one and so any selection based directly on mass would be affected by the different methods used to derive the masses. As no large sample of Coma ETGs with consistent mass determinations is available in the literature this could bias the final sample. Luminosity could also have been used in selecting the sample, but is dependent on population effects and the difficulty of subtracting background light in the core of the cluster. A velocity dispersion based selection provides the cleanest, most robust way of selecting the sample and is directly applicable to studies of the FP.

Table 5.2: Galaxies selected from σ bins

Lower bound on σ (kms^{-1})	Upper bound on σ (kms^{-1})	Galaxies
-	105	PGC44533, PGC44602
105	124	Dressler193, IC4011
124	149	NGC4886, PGC44662
149	180	NGC4873, NGC4883
180	215	NGC4872, NGC4874
215	255	IC4051,NGC4867
255	-	NGC4860, NGC4889

I made use of the ETG catalogue of Scodeggio et al. (1998) in selecting the SWIFT Coma sample. The catalogue contains 109 ETGs (as classified in de Vaucouleurs et al., 1991) with velocity dispersion measurements, redshift determinations and photometry. Coma cluster ETGs in the Scodeggio catalogue span a range in velocity dispersion from 85 to 414 kms^{-1}. Given the dominance of low-mass galaxies and the observing time constraint of selecting ~ 15 galaxies I divided the Coma parent sample into seven logarithmically spaced bins in velocity dispersion. From each bin I arbitrarily selected two galaxies to observe. The velocity dispersion bins and the objects selected are given in Table 5.2.

Table 5.3: Calibration data taken each night

Calibration	No.	Time (s)	Comments
Bias	5	0.0	Shutter closed
Dark	3	*	One set per calibration or science exposure
Arc	3	0.5	Argon and/or neon arc lamp
Flat	3	3.0	Halogen lamp
Vertical Trace	3	5.0	Halogen lamp with vertical mask
Horizontal Trace	3	5.0	Halogen lamp with horizontal mask

* Exposure times of dark frames were chosen to match the corresponding set of calibration or science exposures

5.4 Observations

The observations were carried out in natural seeing, however SWIFT is mounted on the telescope behind the adaptive optics system; even when the AO is not utilised the light from the telescope must first pass through the AO system before reaching SWIFT. The AO dichroic used significantly reduces the flux below 7500 Å that reaches SWIFT. At the beginning and end of each night a series of bias, dark, flat field and arc lamp calibration exposures were taken. Additionally, at the beginning of each run a series of vertical and horizontal line trace exposures were taken. A list of the calibration data required for each night with typical exposure times is given in Table 5.3.

Individual exposures were initially limited to 15 minute integrations to reduce the number of cosmic rays in the thick semiconducting substrate of the SWIFT CCDs. After an initial analysis of the data from the first run this limit was extended to 20 minutes for individual integrations as the incidence of cosmic rays was manageable. Individual integrations were stacked to give an average signal-to-noise ratio of at least 60 within an aperture of 1 Re. For galaxies with $R_e \geq 5$ arcseconds separate sky exposures were taken between each science exposure. For galaxies with $R_e < 5$ arcseconds an 'A-B' sequence was used, placing the galaxy in alternate halves of the field-of-view in order to use the 'sky' region in frame A to sky subtract the object region in frame B and vice-a-versa. The sky coordinates, total exposure time, number of pointings and *I*-band magnitude from Scodeggio et al. (1998) for each object are given in Table 5.4.

5.5 SWIFT data reduction

Reducing IFU data is considerably more complicated than standard spectroscopic reduction because of the need to accurately reconstruct the two dimensional on-sky image from the slitlets as arranged on the CCD. I made use of the dedicated

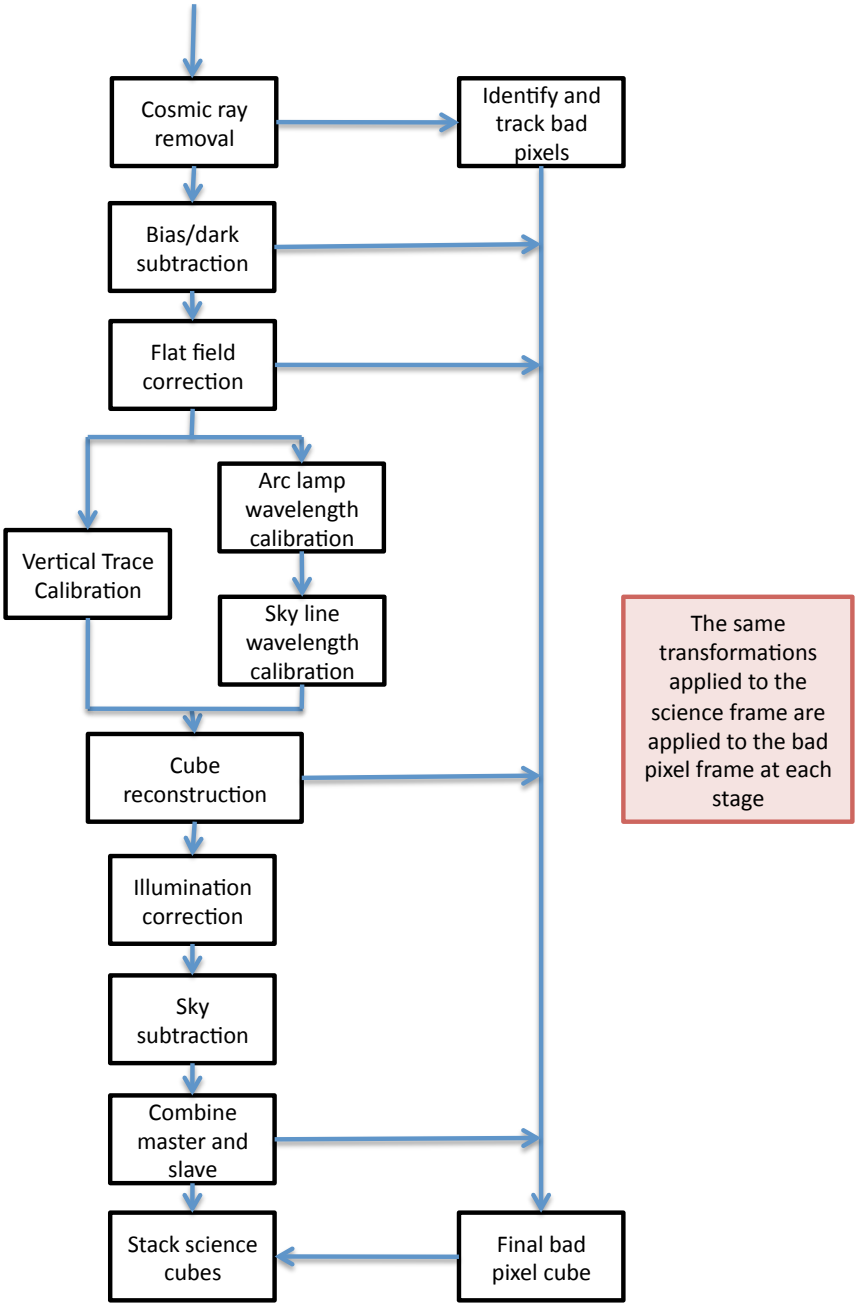

Figure 5.2: Schematic outlining the reduction of SWIFT Integral Field Spectrograph data beginning with raw science observations and ending with sky-subtracted, science-quality stacked data cubes

Table 5.4: Observations of the galaxies in the SWIFT Coma ETG sample

Object	Scodeggio Designation	M_I (mag)	RA (hh mm ss)	Dec (dd mm ss)	Exposure Time (min)	Pointings
PGC445533	A221256	-19.93	12 59 00.1	27 58 03	60	1
NGC4860	A221259	-22.15	12 59 03.9	28 07 25	30	1
NGC4867	A221277	-21.31	12 59 15.3	27 58 14	40	1
PGC44602	A221295	-19.76	12 59 28.7	28 02 26	60	1
NGC4873	A221303	-21.08	12 59 32.8	27 59 01	60	1
NGC4872	A221304	-21.03	12 59 34.1	27 56 48	30	1
PGC44662	A221332	–20.86	12 59 46.1	27 51 26	40	1
Dressler193	A221343	-20.15	12 59 55.1	28 07 41	60	1
NGC4883	A221345	-21.39	12 59 56.0	28 02 05	45	1
NGC4886	A221354	-21.55	13 00 04.7	27 59 23	60	1
IC4011	A221362	-20.30	13 00 06.7	28 00 24	60	1
NGC4874	UGC8103	-25.18	12 59 35.9	27 57 43	80	4
NGC4889	UGC8110	-24.88	12 57 43.7	28 14 54	30	1†
IC4051	UGC8129	-22.48	13 00 54.7	28 00 34	40	1

Notes: M_I taken from Scodeggio et al. (1998). Pointings refers to widely separated (> 5") exposures on sky. All single-pointing galaxy exposures were dithered to minimise the effect of bad pixels
† Two pointings were observed for NGC4889 however both exposures for one pointing suffered from significant extinction (> 4 mags) due to cloud cover.

swift pipeline implemented in *iraf* and written by Ryan Houghton. The entire data reduction scheme is summarised in schematic form in Figure 5.2 and I will describe each stage in more detail below. Some of the early steps must be applied to the calibration frames before they can be used later in the reduction scheme. Examples of raw science and calibration frames are shown in Figure 5.3. On a raw frame the spatial coordinate varies along the x′-axis (along a row) and the spectral coordinate varies along the y′-axis (along a column).

5.5.1 Initial reduction steps

Cosmic rays were first identified and removed in one of two ways. For calibration frames, where multiple identical exposures were taken, cosmic rays were identified

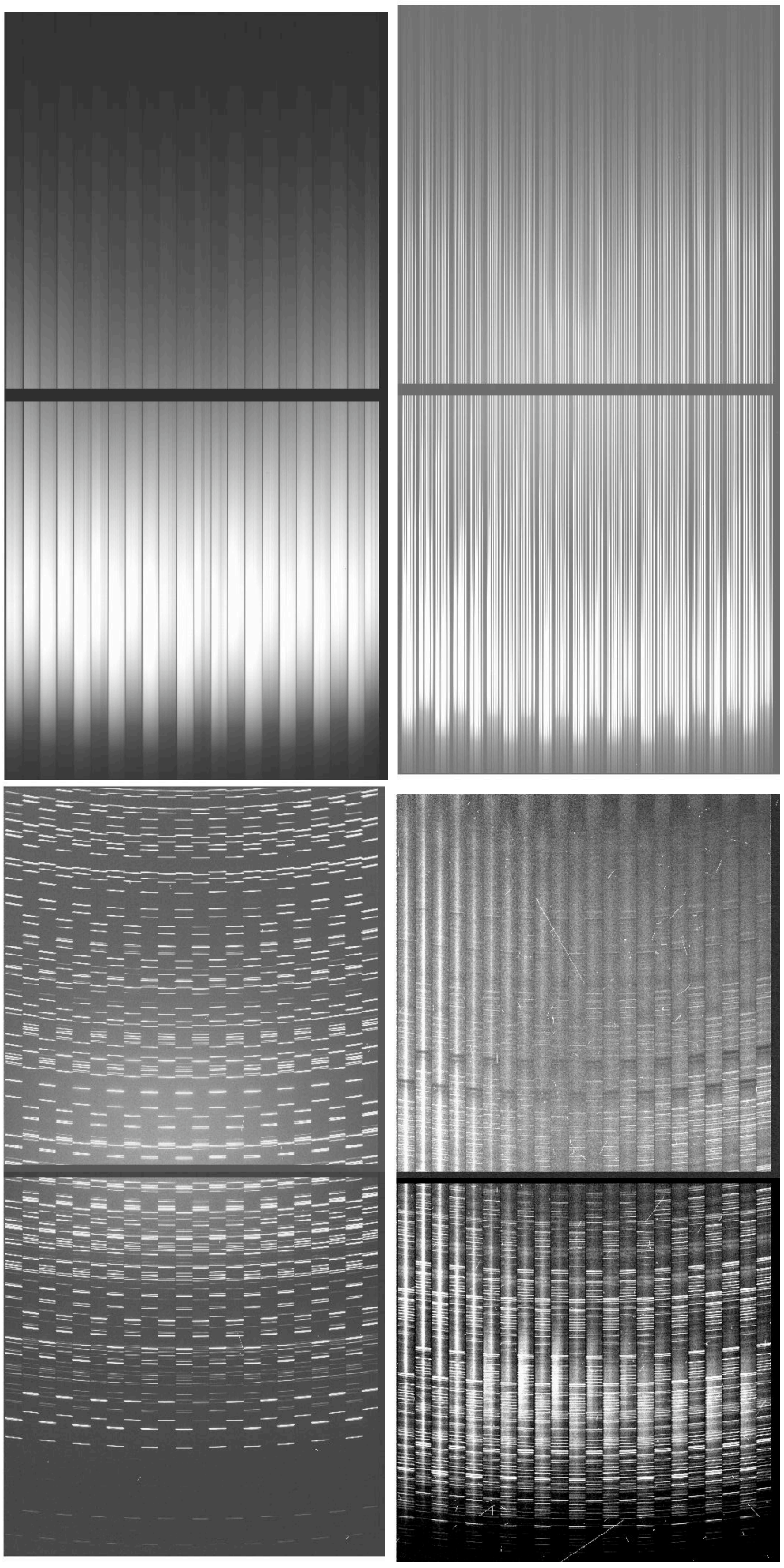

Figure 5.3: Raw SWIFT data. a) Halogen lamp (or flat) frame. b) Vertical trace frame. c) Arc lamp frame. d) Science observation frame

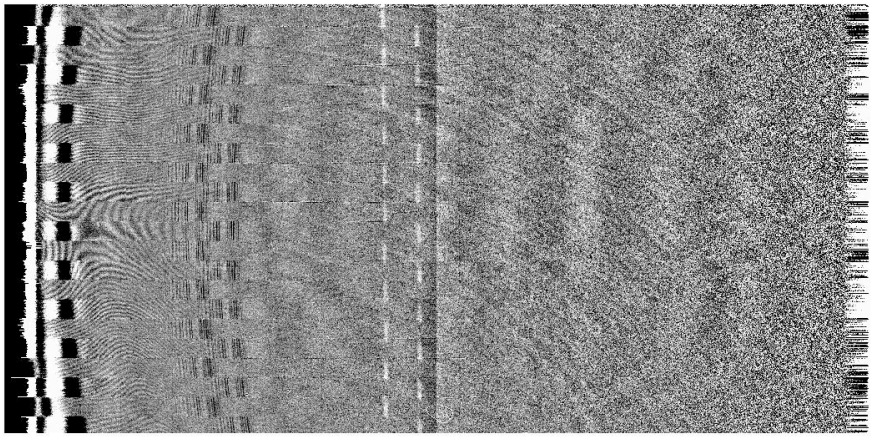

Figure 5.4: Flat field frame, normalized to a mean of 1.0. Bright regions have higher than average flux and dark areas lower than average. The regions at the left and right of the CCD are not exposed.

and corrected by applying a pixel sigma-clipping and mean combining scheme to all frames. I rejected the highest and lowest values for a given pixel across the set of exposures and formed a single high S/N frame by averaging over the remaining pixel values. This approach was typically used for all dark, arc, lamp and vertical trace calibration frames. The rms residuals determined by bootstrapping were $\sim$ 0.7 per cent. Where multiple identical exposures were not available I used the *iraf* implementation of LACosmic (van Dokkum, 2001) to iteratively identify cosmic rays and replace those pixels with NaN values. Values above a threshold of 3σ from a fit to the observations were rejected. LACosmic was iterated until no further cosmics were identified. The locations of cosmic rays were also tracked by the bad pixel mask, the use of which is described in Section 5.5.4.

The next step was to either subtract the bias level or a dark frame from all exposures. For data from the first observing run I opted to subtract dark frames matched in exposure time to each science or calibration exposure because of the discovery of a significant light leak in the instrument. As the dark frames also include the bias level no additional bias subtraction was required. In the later observing run the light leak was eliminated and subtracting a constant bias value, determined from an unexposed overscan region, was sufficient.

A flat field correction was applied to all exposures to account for pixel-to-pixel variations in the CCD sensitivities. The differing wavelength sensitivities of the two CCDs were also normalised to a common level at this stage. A flat-field frame was produced by dividing each row of a halogen lamp exposure (typically known as a lamp flat or simply flat: panel a) of Figure 5.3) by the median lamp spectrum (formed by collapsing the raw frames along the spatial direction). The resulting flat-field frame was then normalised, which is shown in Figure 5.4. Each science frame was then divided by the flat-field frame. At this stage an illumination frame (which is used to correct for non-uniform illumination of the CCDs) was also extracted from the lamp flat, however this correction was not applied until a later stage in the reduction process. Twilight flats were not taken and dark sky frames had too few counts for an accurate illumination correction cube to be produced.

5.5.2 Production of data cubes

In order to produce finished data cubes two transformations must be applied to the raw science exposures: one from the x′-axis to the on-sky x and y spatial coordinate system and the other from the y′-axis to a properly calibrated wavelength scale. The *swift* pipeline calculates these two transformations from the vertical trace and arc lamp calibration frames respectively and then applies the two transformations in series. Both transformations require the interpolation of pixel values from the (x′,y′) CCD coordinate system to the (x,y,z) data cube coordinate system.

The vertical trace frames consist of halogen lamp exposures where a mask has been placed in the focal plane (i.e. before the image slicer when the light is still in the on-sky coordinate system) consisting of six narrow slits aligned perpendicular to the slitlets (see panel b) of Figure 5.3). By tracing the positions of these vertical slits on the CCD and aligning a given trace across all slitlets it is possible to reconstruct the original (x,y) coordinates of each pixel for each x′. The typical rms residuals from the fit to the vertical trace frames were 0.1 pixels, increasing at both ends of the

SWIFT spectral range. Cubes of the vertical trace frames were visually inspected to identify any misalignment in the transformation.

The wavelength transformation was initially determined from an arc lamp exposure (panel c) of Figure 5.3. In the first observing run both argon and neon arc lamps were used to produce ~ 80 bright arc lines across the full SWIFT wavelength range. In the later run only the argon arc lamp was available, resulting in a reduced number of arc lines (~ 50) available for calibration, particularly at shorter wavelengths. The wavelength calibration was performed independently for each slitlet using the *iraf* task *autoidentify*, which automatically matches the positions of arc lines on the CCD to wavelength values contained in a list of arc lines determined from laboratory measurements (see the SWIFT pipeline manual for details of the arc lamp line lists). After identifying arc lines a smooth function is fit to the pixel coordinates and wavelengths providing a transformation from pixel coordinates to wavelength coordinates for each spaxel. Wavelength calibrated arc frames were inspected to ensure a consistent solution across the entire CCD had been achieved. Residuals between the arc line positions and the wavelength solution were ~ 2 Å.

A second wavelength calibration step was applied to the science observations, making use of the bright night sky lines in the SWIFT wavelength range. The night sky line atlas of Hanuschik (2003) was used to match to the observed sky lines and determine an improved wavelength solution. During the development of the pipeline it was found that flexure effects introduce a small ($\sim 0.1 - 1.0$ Å) difference between the arc lamp wavelength calibration and the true wavelength scale of the science exposures. This offset is a non-linear function of wavelength and also varies with spatial coordinate. Re-calibrating the wavelength solution using the sky lines present in the science frame corrects for this offset providing a wavelength solution accurate to ~ 0.05 Å across the entire frame. The accuracy of the wavelength calibration was determined by comparing the calibrated wavelengths of the observed lines to corresponding lines in the sky line list. The initial arc lamp based calibration was

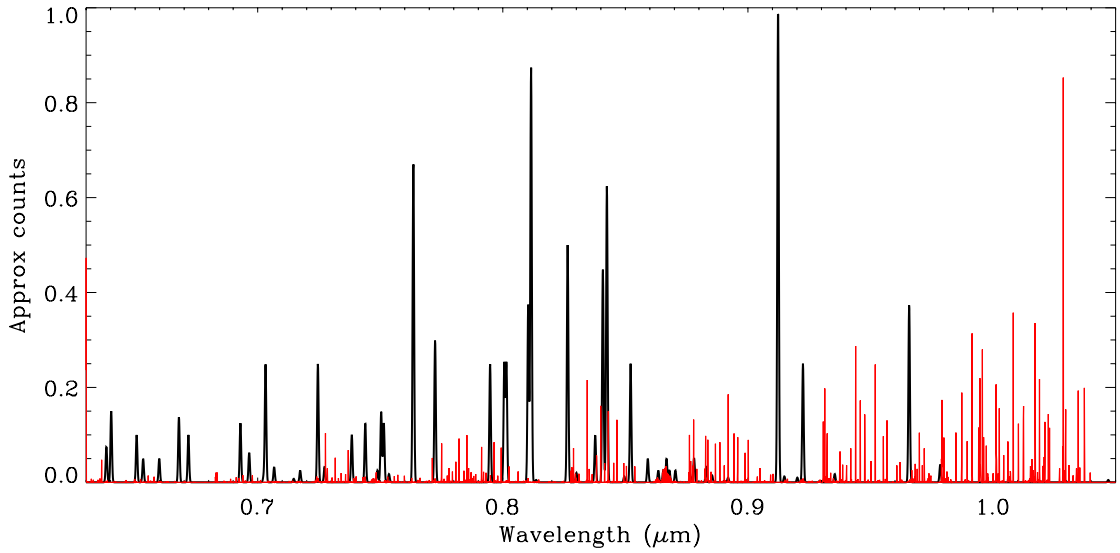

Figure 5.5: Spectra used for wavelength calibration. A combined argon and neon arc lamp spectrum is shown in black. The night sky emission lines are shown in red. The two spectra are normalised to the same peak flux level. The ~ 70 brightest night sky lines are used in the second wavelength calibration. Note the increase in sky lines at long wavelengths – this makes accurate sky subtraction beyond ~ 0.92 μm challenging. A weaker group of sky lines between 0.85 and 0.9 μm are the main source of residuals in the SWIFT kinematic analysis.

required to provide an approximate solution in order to accurately identify the sky lines, which have much lower S/N than the arc lines. Figure 5.5 shows an argon and neon arc lamp spectrum and a night sky spectrum observed with SWIFT used for the wavelength calibration.

Once the vertical trace based spatial transformation and accurate sky spectrum based wavelength transformation have been determined, the two-dimensional science frames were transformed into a three-dimensional data cubes. The 22 slitlets were extracted and corrected for curvature using the transformation determined from the vertical trace frame, fixing the x coordinate of the data cube. This resulted in 22 two-dimensional long slit spectra. Next each spectrum was put on a common wavelength scale based on the accurate wavelength calibration from the sky lines, fixing the z coordinate of the data cube. Finally the 22 wavelength calibrated long

slit spectra were arranged together, according to the slitlet identification from the vertical trace data, fixing the y coordinate of the data cube. The errors on this process were derived from the trace and wavelength calibration steps; this gave spatial accuracies of 0.1 pixels and spectral accuracies of 0.05 Å (1/20th of a pixel). The same transformations were applied to the illumination frame described in Section 5.5.1, resulting in an illumination cube. The science data cubes were divided by the illumination cube to produce the final illumination corrected data cubes.

5.5.3 Sky subtraction

As can be seen in the sky spectrum in Figure 5.5 there are many bright night sky lines in the SWIFT spectral range. This is useful for determining an accurate wavelength calibration, however when seeking to extract kinematics from the observations removing these sky lines is extremely important. The flux in a bright sky line can be several orders of magnitude greater than that in the absorption features of interest, therefore accurate sky subtraction is vital; accuracies of 1 per cent are desireable for extracting kinematic information. The brightness of the continuum component and the sky lines varies with time, so for non-simultaneous sky subtraction the sky continuum and line fluxes must be scaled independently. Additionally, the relative ratios of sky lines also vary with time, however according to Davies (2007) groups of lines due to similar vibrational or rotational transitions which have constant flux ratios can be identified. In most cases all the lines in a sufficiently narrow wavelength range satisfy this condition, so by considering only a small spectral region around a feature of interest it is possible to avoid the problem of varying line ratios.

A high S/N sky spectrum was produced by binning all spaxels in a pure sky data cube. Using the sky line list, regions containing a sky line were initially masked and the remaining spectrum median-smoothed to minimise the effect of noise and any unmasked faint lines. This left a smoothly varying sky continuum spectrum. The sky continuum was fitted with a smooth, low-order polynomial as a function

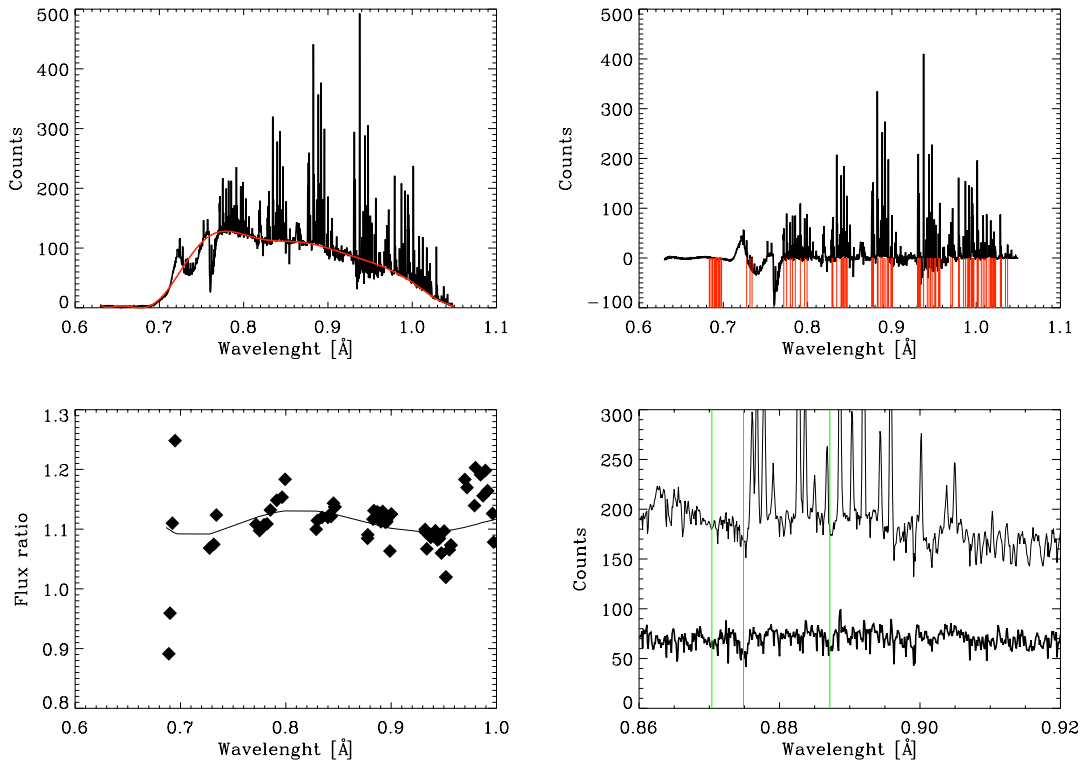

Figure 5.6: Upper left: Sky spectrum with polynomial fit to the sky continuum performed on a spatially collapsed sky cube overplotted in red. Upper right: Sky line spectrum produced by subtracting the fitted sky continuum from the spatially collapsed sky cube. Positions of prominent sky lines are indicated by red markers. Lower left: Flux ratio of sky lines in the science and sky frame, determined from a Gaussian fit to each line. Solid line is a polynomial fit to all the line ratios. Lower right: Raw unsubtracted science spectrum (upper) and sky-subtracted science spectrum. Green lines indicate the approximate position of the CaT lines.

of wavelength. This fitted sky continuum spectrum was replicated in each spaxel, producing a sky continuum cube. This sky continuum cube was subtracted from the sky cube to produce a sky line cube. On the object frame I identified spaxels dominated by sky flux at large radii from the centre of the object. Sky lines were again masked using the sky line list and the sky continuum cube was scaled and subtracted from the object cube such that the total continuum flux tends to zero at large radii. This left a sky continuum subtracted object cube, containing night sky lines as well as flux from the object of interest.

I isolated a small wavelength range around the features of interest (typically 8500 - 9000 Å in the case of the CaT absorption lines) and produced a sky line

dominated, high S/N spectrum by binning all spaxels at large radii. The same wavelength range was extracted from the sky line cube. There are ~ 10 bright sky lines in this spectral range. I fit a Gaussian to each of these bright sky lines in both the object and sky line cubes to determine the total flux in each line. The flux ratio between sky and object frame was determined for each line. Finally, the sky line cube was scaled by the mean line flux ratio and subtracted from the object cube to produce sky subtracted science data cubes. A similar procedure was applied to sky subtract objects observed with the nod-on-IFU technique. The various stages of the sky subtraction process are illustrated in Figure 5.6. The sky continuum subtraction was accurate to better than 1 per cent, determined from spectral regions away from bright sky lines. The sky line subtraction was accurate to ~ 2 per cent, determined by comparing the mean residuals around the bright sky lines to the residual noise in the continuum parts of the spectrum. The sky line residuals are somewhat larger than desired for accurate kinematic information to be extracted. While kinematics can still be determined care must be taken in identifying residuals in the regions around bright sky lines.

Up to this stage the master and slave frames have been treated separately; sky subtraction was the final step that requires this. At this stage I combined the master and slave cubes from a given exposure into a single data cube. This data cube has the full spectral and spatial dimensions of the SWIFT coverage; 10.34 x 21.62 arcseconds and 0.63-1.05 μm. This was the final stage in the main data reduction process.

5.5.4 Bad pixel correction and exposure stacking

Throughout the entire data reduction process the propagation of bad pixels was tracked. The initial determination of bad pixels combined static bad pixel maps (one each for the master and slave frame) with bad pixels flagged during the cosmic ray identification process. At this stage a raw bad pixel frame was created, with

'good' pixels identified with zeros and bad pixels flagged with ones. This raw bad pixel frame was treated in an identical fashion to the science data frames, resulting in a bad pixel cube for each science data cube. The reduction process 'smeared out' the bad pixels such that pixels in the data cube had a value between zero and one encoding their degree of 'badness'. This information was used when combining multiple exposures into the final data products.

The first step in stacking multiple exposures was to accurately identify the object centre in each frame. I did this by collapsing each cube in the spectral direction to form a broad band image. On this image I used the weighted first moments of the luminosity distribution to determine the object centre to an accuracy of 0.1 spaxels; this was repeated on each science cube. With this information the extent of the final stacked data cube can be determined, along with the final location of every pixel from the individual exposures in this final data cube. Science cubes were only aligned to an accuracy of 0.5 spaxels; finer interpolation was not possible due to hardware limitations. 0.5 spaxels corresponds to an accuracy $\sim$ 0.1 arcsecs, or approximately 10 per cent of the seeing.

At this stage I returned to the bad pixel cubes and flagged any pixel with a value greater than 0.001. This typically flagged only 0.01 per cent of pixels in each cube. Any flagged pixel was rejected and replaced with a NaN value. The positions of these flagged pixels in the final stacked data cube was also tracked. The stacked data cube was created by adding corresponding pixels from the individual data cubes. Each pixel in the stacked data cube was then scaled by the number of pixels contributing to it; this preserved the relative flux between pixels while maximising the S/N in each pixel. At this stage the final data products were complete and the kinematic analysis can begin.

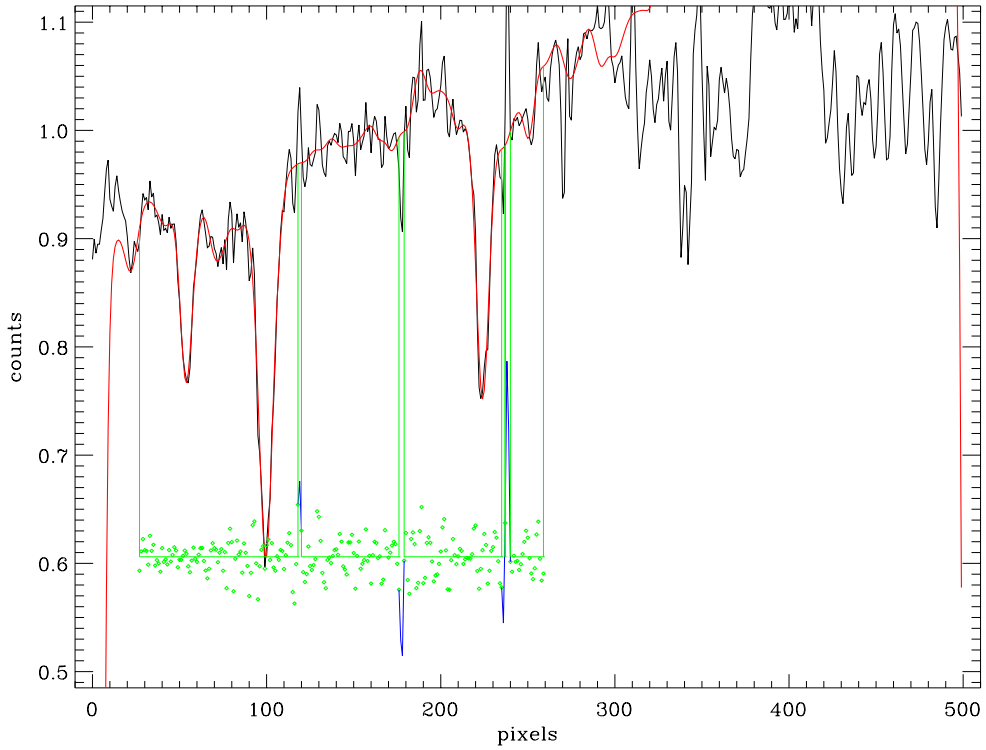

Figure 5.7: Central aperture spectrum for IC4011(black line) and pPXF fit to the observations (red line). The green points show the residuals between the observed spectrum and the pPXF fit. The fit was carried out over the region inside the green lines, excluding the residuals indicated in blue.

5.6 Kinematic extraction

The principal goal of these IFU observations of Coma cluster ETGs is to determine the kinematic structure of these objects. In order to extract the kinematic information from the spectroscopic data cubes I again made use of the penalized PiXel Fitting (pPXF) code of Cappellari & Emsellem (2004). pPXF uses a library of stellar spectra to produce a template spectrum for the galaxy and convolves this with a line of sight velocity distribution (LOSVD) to best match the observations. For fitting the CaT absorption features I used the stellar spectra library of Cenarro et al. (2001), which contains $\sim$ 700 spectra of stars covering a broad range in age and metallicity.

5.6.1 Template spectrum

pPXF was initially used to produce a single template spectrum for each galaxy. I extracted a high S/N spectrum from a 3 arcsecond circular aperture centred on each object. Using an approximate redshift from the Scodeggio et al. (1998) catalogue I matched the wavelength range of the template spectra to the rest frame wavelength of the central galaxy spectra. The Coma cluster is at a redshift of approximately $z = 0.02$, which at ~ 8500 Å shifts the CaT lines by ~ 150 Å. After matching the template and galaxy spectra pPXF produced a single best-fitting template spectrum by scaling and combining ~ 20 of the stellar template spectra and convolving with the LOSVD. I limited the LOSVD to the first two moments of the velocity distribution, v and σ. Additionally a second-order additive and multiplicative polynomial component was included in the fit. Any residuals from cosmic rays or inaccurate sky subtraction were cleaned at this stage by rejecting data points greater than three sigma from the fitted spectrum and repeating the fit. Only a single rejection iteration was required to produce stable kinematic measurements. Very large sky residuals were masked from the fitting process. An example of this process is shown in Figure 5.7, which shows the central aperture spectrum for IC4011 and the corresponding pPXF fit. The unconvolved template spectrum was fixed and used to determine the spatially resolved kinematics. This method was used because the spatially resolved spectra are much lower S/N than the central aperture spectrum and so fixing the template while only allowing the LOSVD to vary produces a more robust determination of the kinematics.

5.6.2 Voronoi binning and spatially resolved kinematics

As the object flux (hence the S/N) decreases rapidly with radius it was necessary to spatially bin the data to determine reliable kinematics at large radii. The goal was to achieve constant S/N in all bins across the entire field of view; by necessity

this required bins at large radii to be much bigger than those in the centre of the object. I made use of the Voronoi binning technique of Cappellari & Copin (2003) to achieve this. The Voronoi technique accretes additional pixels onto a bin until a given S/N is reached, starting from the highest S/N pixels. The technique iterates until the optimal use is made of all pixels, resulting in irregularly gridded bins with constant S/N. The S/N of each spaxel is determined by subtracting a median-smoothed version of the data from the observed spectrum and determining the rms of the residuals between the smoothed and raw spectra. I selected a S/N threshold of 40 as the best compromise between extracting robust kinematics from each bin and giving good spatial coverage of each galaxy. Spaxels with a S/N < 2 are excluded from the Voronoi binning.

Once the Voronoi binning scheme had been devised for each galaxy the spectrum for each bin was formed by co-adding the spectra from each of the contributing spaxels. For each bin pPXF determined the best-fitting LOSVD by convolving the previously determined global template spectrum with the LOSVD to reproduce the observed spectrum. At this stage I included only a linear additive component and no multiplicative component due to the reduced S/N of the spatially resolved data. The LOSVD was again restricted to the first two moments of the velocity distribution.

5.6.3 Flux, velocity and velocity dispersion maps

pPXF returned the velocity and velocity dispersion for each bin. I computed the surface brightness of each bin by dividing the mean flux in the bin by the number of spaxels contributing to the bin. This information is displayed in Figure 5.8, showing the flux, velocity and velocity dispersion maps for each galaxy. Flux maps are displayed with a logarithmic scale. Velocity maps are displayed after subtracting the mean velocity of each galaxy. Contours of constant flux are overplotted on the velocity and velocity dispersion maps. The galaxies show a range of kinematic types, which I will discuss in the next chapter. Here I will briefly discuss the maps from

the point of view of the data reduction.

The maps appear to be of varying quality, with some galaxies showing apparently large fluctuations, particularly in σ. Much of this effect is down to the visual impression: the very large bins in the outer parts of all galaxies serve to overemphasise the azimuthal variation. The maps are displayed without any interpolation, (which is often used when publishing spatially binned IFU maps) to accurately represent the information present. v and σtypically vary by 10-15 per cent, consistent with the measurement errors. There is a larger variance at large radii as, despite the Voronoi binning procedure, bins in these regions typically have lower S/N than those in the centres of each object. 9/14 of the maps have variations consistent with the measurement errors determined by the pPXF fitting procedure. In the remaining maps prominent outlying bins do exist, beyond what would be expected from the measurement errors. These bad v and σ measurements are due to over- or under-subtracted sky lines and occur particularly in the outer bins where the sky line flux can be up to 100 times the object flux. These bins were excluded from the analysis discussed in the following chapter. In the case of Dressler193, the quality of the data was too poor to allow a reliable determination of the spatially resolved v and σ, however the maps are presented for completeness.

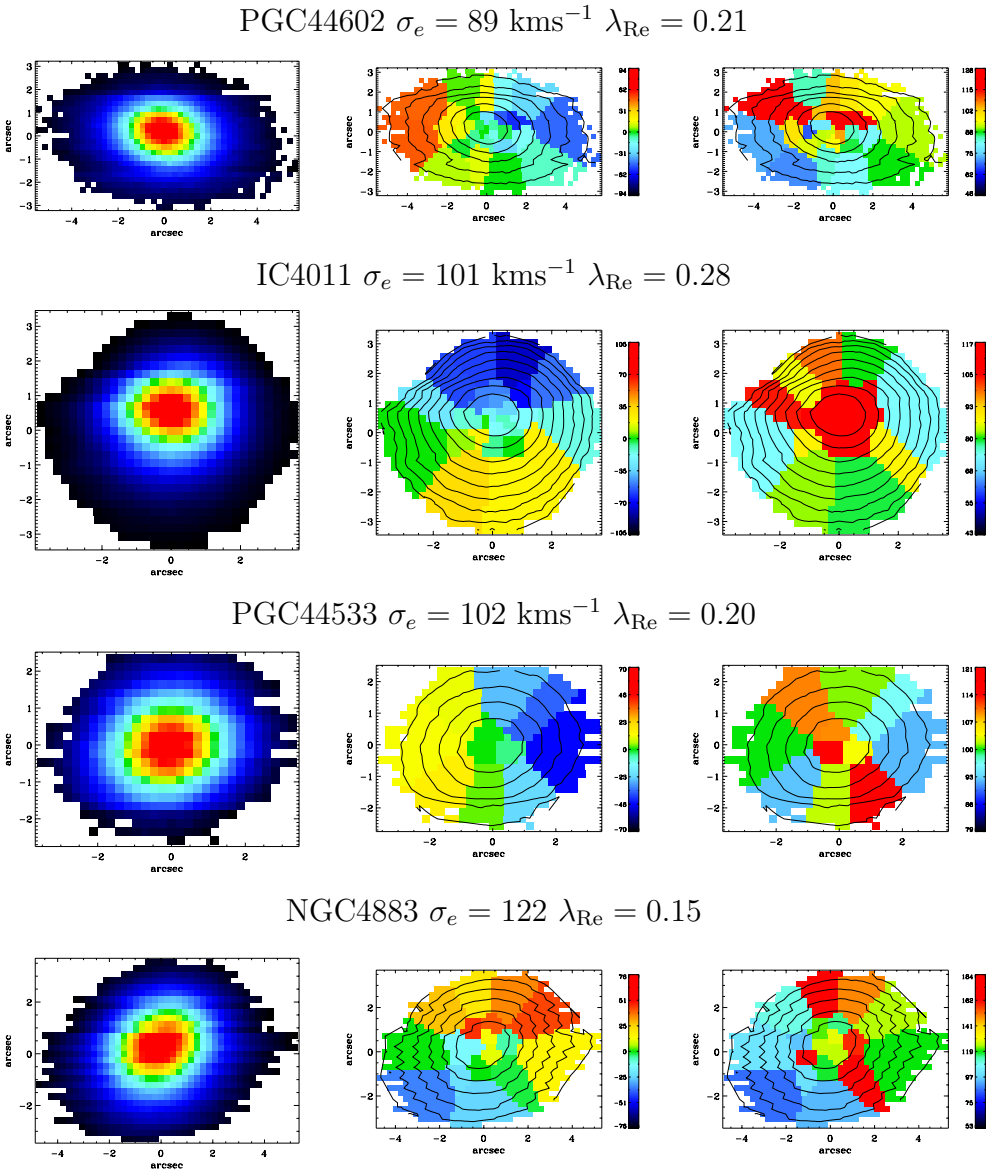

Figure 5.8: Flux (left column), velocity (centre column) and velocity dispersion (right column) maps. In the v and σ maps the flux contours are shown overplotted. The values of v and σ associated with a given colour are indicated in the colour bar in each panel. The objects are shown in order of increasing σ_e. The determination of σ_e and $\lambda_{\rm Re}$ is described in the following chapter.

Dressler193 $\sigma_e = 126$ kms^{-1} $\lambda_{\rm Re} = 0.11$

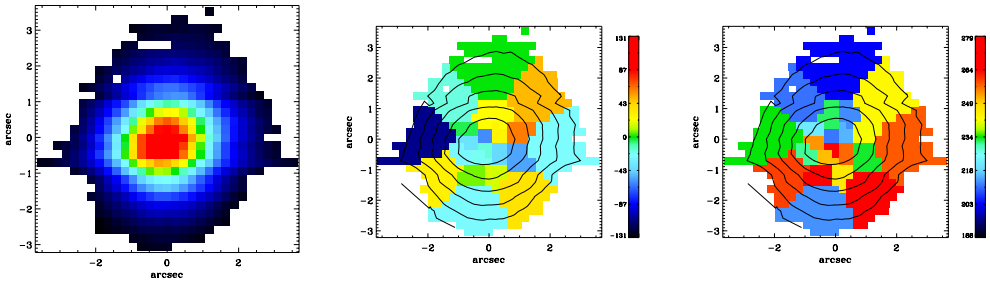

NGC4886 $\sigma_e = 129$ kms^{-1} $\lambda_{\rm Re} = 0.06$

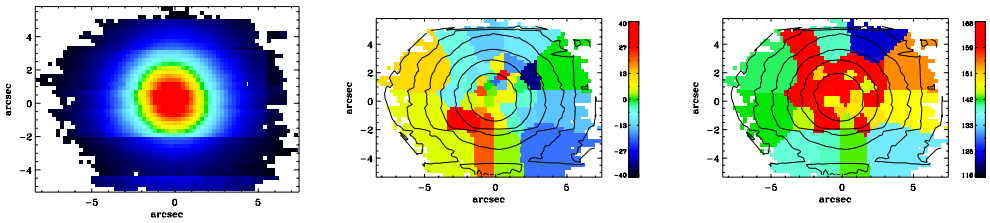

PGC44662 $\sigma_e = 130$ kms^{-1} $\lambda_{\rm Re} = 0.22$

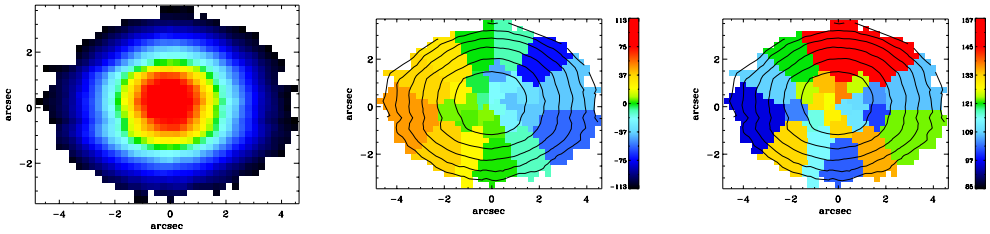

NGC4873 $\sigma_e = 153$ kms^{-1} $\lambda_{\rm Re} = 0.17$

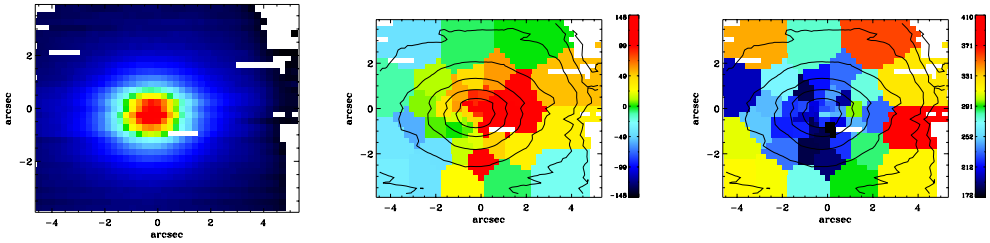

NGC4860 $\sigma_e = 178$ $\lambda_{\rm Re} = 0.10$

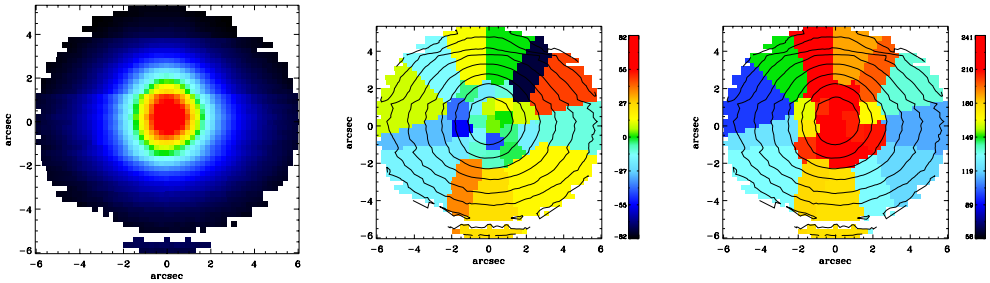

Figure 5.8 (continued)

NGC4867 $\sigma_e = 206$ kms^{-1} $\lambda_{\rm Re} = 0.20$

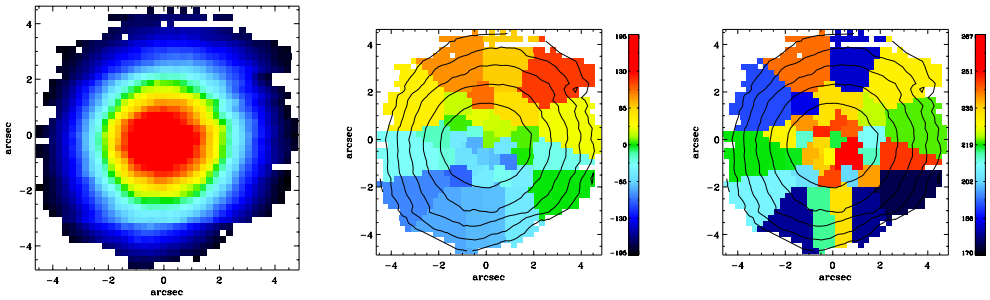

NGC4874 $\sigma_e = 214$ kms^{-1} $\lambda_{\rm Re} = 0.08$

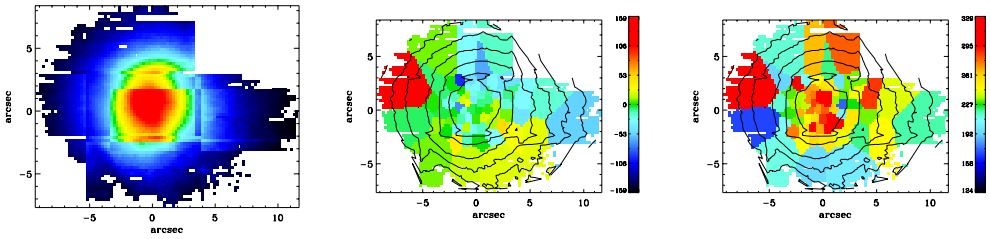

NGC4872 $\sigma_e = 215$ kms^{-1} $\lambda_{\rm Re} = 0.34$

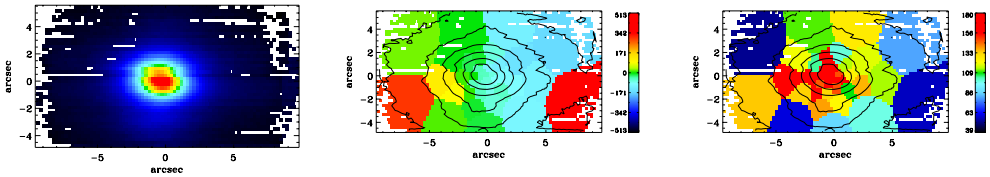

IC4051 $\sigma_e = 249$ kms^{-1} $\lambda_{\rm Re} = 0.04$

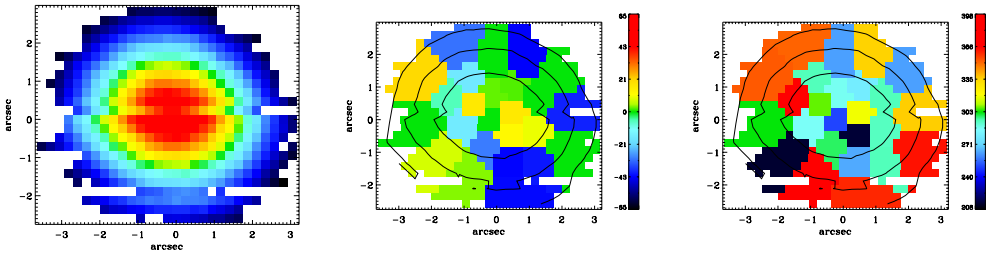

NGC4889 $\sigma_e = 393$ kms^{-1} $\lambda_{\rm Re} = 0.11$

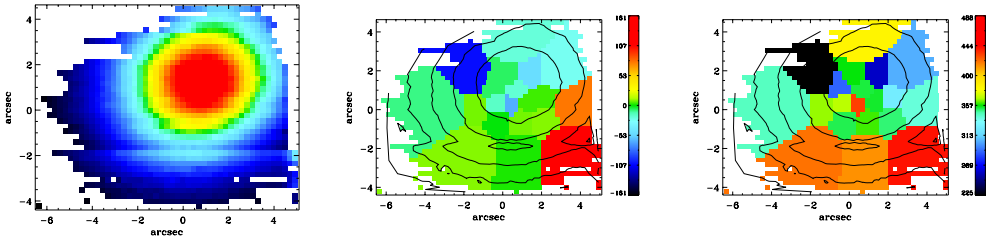

Figure 5.8 (continued)

Chapter 6

Dynamical properties of Early-Type Galaxies in the Coma Cluster

6.1 Photometric observations

IFU observations alone are not sufficient to fully constrain the dynamical properties of ETGs; they must be complemented by broad-band imaging as well. While collapsing an IFU data cube along the spectral dimension gives some information about the broad-band light distribution in an object this information is generally inferior to that obtained from imaging. The imaging data is typically deeper, covers a much larger field-of-view (which is particularly important when studying nearby ETGs because of their large apparent R_es) and, if multiple bands are available, covers a much broader wavelength range. Imaging is necessary to determine important photometric quantities such as ϵ, R_e and the mean surface brightness within that radius, $\langle I_e \rangle$. Photometry out to at least several R_e is necessary to constrain the JAM models described in Chapter 2 which I intend to apply to the SWIFT Coma ETG sample.

Instead of obtaining new imaging observations of my sample I made use of archival data from several sources. The sample was originally selected with the Coma Legacy Survey in mind, however the failure of the Advanced Camera for Surveys (ACS) instrument on the HST prevented the complete sample being observed. See Hammer et al. (2010) for details of the Coma galaxies successfully observed by the Coma ACS Legacy Survey. Because of the incomplete HST coverage of my sample I turned to the SDSS photometry described in Chapter 2 which I had previously used successfully for the ATLAS^{3D} survey. The entire Coma cluster falls within the SDSS survey volume and has been observed in all 5 SDSS filters. The comparison between MGEs derived from HST and ground-based photometry versus purely SDSS photometry (Section 2.9) suggests that the SDSS-based MGE models are sufficient for my purposes.

6.1.1 Determining R_e and I_e

Accurately determining the R_e and I_e is a difficult process. Several alternative approaches exist such as Sérsic profile fitting (Graham & Driver, 2005) or curve-of-growth fitting (for example, Cappellari et al., 2006). Measuring these values is also dependent on accurately subtracting the night sky background and any other background light due to, for example, nearby stars or galaxies or, in the case of clusters such as Coma, the intracluster light. Comparing R_es (and other global parameters) between different samples determined using different techniques is fraught with systematic effects.

I made use of the curve of growth technique to determine R_e and I_e from the SDSS photometry. The curve of growth is the relation between the integrated counts within a given circular aperture and the radius of that aperture. Before determining this for each object I first carefully subtracted the sky background from each image. R_e and $\langle I_e \rangle$ are very sensitive to inaccurate sky subtraction so great care was taken at this stage. The curve of growth was determined directly from the sky-subtracted

images. I then fit an $R^{1/4}$ growth curve to the observations over the range 2" $\leq r \leq 5R_{e,\mathrm{lit}}$, where $R_{e,\mathrm{lit}}$ is the literature value for the effective radius taken from Scodeggio et al. (1998). This excludes the central region which may be affected by saturation, the PSF and any nuclear emission and restricts the fit to the region where the object's light dominates over the sky background flux. The effective radius and total counts were then computed from the $R^{1/4}$ fit. The total counts were then converted to a surface brightness, $\langle I_e \rangle$, using the standard SDSS photometric calibrations.

In addition to the widely used curve-of-growth fitting technique described above I also determined R_e and I_e directly from MGE models of sample galaxies. This technique is described in Cappellari et al. (2009). The MGE models were constructed as described in Chapter 2, using the automated techniques described at the end of that chapter. Special care was taken in masking nearby objects and subtracting the sky and intracluster light due to the dense nature of the core of the Coma cluster. The R_es were measured firstly by 'circularising' each MGE model - setting the axial ratios of all Gaussian components to 1 while preserving their flux. The total luminosity of each MGE model was computed using:

$$L_{\mathrm{TOT}} = \sum_{j=1}^{n} 2\pi I_j \sigma_j^2. \tag{6.1}$$

Here σ_j is the width of the Gaussian components in the MGE model, *not* the velocity dispersion as is the case in the majority of this chapter. Next the light enclosed at a given radius r was determined by summing over the contribution of each Gaussian component out to that radius. R_e is then the value of r which encloses $L_{\mathrm{TOT}}/2$. $\langle I_e \rangle$ is then given by: $\langle I_e \rangle = \frac{L_{\mathrm{TOT}}/2}{\pi R_e^2}$. As expected the two techniques agree well, with a scatter of 16 per cent in R_e and 3 per cent in $\langle I_e \rangle$. From here onwards, R_e and $\langle I_e \rangle$ refer to values determined from the curve of growth fit using only SDSS photometry. These values are given in Table 6.1.

Errors on R_e and $\langle I_e \rangle$ were estimated by varying the sky level by 0.5, 1, 3 and 5

times the rms noise in the sky. Typical errors of ~ 10 per cent were found. While R_e and $\langle I_e \rangle$ are very sensitive to the accuracy of the sky subtraction the combination of R_e and I_e which appears in the FP is more stable.

6.1.2 Determining ϵ

One of the most important photometric parameters to determine is the ellipticity, ϵ. As well as being important in determining the aperture for spectroscopic measurements such as σ_e and λ_R, it also is directly involved in determining whether a galaxy is a fast- or slow-rotator (see Section 6.4). I determined the ellipticity as described in Krajnović et al. (2011), using the IDL routine *find_galaxy*[1]. The second moments of the luminosity distribution, I_{xx}, I_{yy} and I_{xy}, were determined for all pixels belonging to the galaxy above a fixed brightness, the level being chosen such that the pixels selected encompass a region with radius 1 R_e or matching the extent of the IFU observations, whichever is the smaller. From the second moments the ellipticity was determined by:

$$\begin{aligned} a^2 &= \frac{I_{xx}+I_{yy}}{2} + \sqrt{\left(\frac{I_{xx}-I_{yy}}{2}\right) + I_{xy}^2} \\ b^2 &= \frac{I_{xx}+I_{yy}}{2} - \sqrt{\left(\frac{I_{xx}-I_{yy}}{2}\right) + I_{xy}^2} \\ \epsilon &= 1 - b/a \end{aligned} \tag{6.2}$$

The ellipticities measured within this aperture, ϵ_e are given in Table 6.1. No allowance was made for the effect of seeing on the observed ellipticity, however the aperture within which ϵ_e was determined was in all cases at least 8 times larger than the full-width at half-maximum of the PSF, limiting the influence of the PSF on the measured ϵ.

[1]Available as part of the MGE package of Cappellari et al. (2002).

Table 6.1: Photometric and spectroscopic parameters of the SWIFT Coma ETG sample

Name	R_e (arcsec)	μ_e, r (mag arcsec^{-2})	σ_e (kms^{-1})	Aperture	λ_R	Classification
Dressler193	4.07	18.81	126	1.0	0.11	S
IC4011	5.41	19.12	101	0.58	0.28	F
IC4051	17.67	19.93	249	0.46	0.04	S
NGC4860	6.99	18.27	178	1.0	0.10	S
NGC4867	2.35	16.98	206	1.0	0.20	F
NGC4872	4.35	18.05	216	1.0	0.34	F
NGC4873	8.57	19.24	153	1.0	0.17	F
NGC4874	54.31	20.78	214	0.31	0.08	S
NGC4883	7.49	18.99	122	1.0	0.15	F
NGC4886	7.16	18.93	129	1.0	0.06	F
NGC4889	31.61	19.45	393	0.56	0.11	S
PGC44533	4.95	19.66	102	0.74	0.20	F
PGC44602	6.00	19.78	89	0.95	0.21	F
PGC44662	4.46	18.68	130	0.99	0.22	F

6.2 Measuring σ_e

Once R_e and ϵ_e have been determined it is possible to measure the velocity dispersion within 1 R_e, σ_e, directly from the IFU data cubes. For galaxies where the IFU field of view > 2 R_e, an R_e aperture spectrum was formed by binning all pixels lying within an elliptical aperture with semi-major axis length of 1 R_e and ellipticity ϵ_e. For galaxies larger than this an aperture spectrum was formed by accreting spaxels into an aperture of ellipticity ϵ_e until the mean S/N of a just-accreted spaxel falls below 2. At this point the diminishing returns from adding additional low S/N pixels means accreting additional spaxels makes little difference to the quality of the aperture spectrum. I repeated the pPXF fitting procedure described in Section 5.6 on this aperture spectrum, allowing the template spectrum to vary, and so determined σ_e. The measured values, along with the spectroscopic aperture size (as a fraction of R_e) are given in Table 6.1. Formal errors from the pPXF fits were 5-10 per cent (5-30 kms^{-1}).

6.3 The Fundamental Plane of ETGs in Coma

As described in Chapter 1 the Fundamental Plane (FP) of ETGs is a key observable relation in constraining the evolution of ETGs. It is a relation between R_e, $\langle I_e \rangle$ and σ_e. The FP was initially used as an accurate distance estimator (Dressler et al., 1987) because of the dependence of R_e on distance and the independence of the other two parameters. However this is a drawback when using the FP as a test of galaxy evolution as inaccurate distance estimates are the primary source of scatter in the relation. Measuring the FP within a single cluster, where all objects have essentially the same distance, eliminates this source of error, allowing very accurate FP determinations. This is one of the principal motivations behind observing the SWIFT Coma ETG sample – to provide an accurate FP determination.

The determination of the three FP parameters (listed in Table 6.1) was described in the previous section. Here I will discuss the fitting of the plane to these variables. I initially determined the FP from a robust bi-weight fit (using the IDL AstroLib routine *robust_planefit*, based on Tukey's biweight method; Tukey, 1977) to the observations. This gives a FP of the form:

$$\log\left(\frac{R_e}{\mathrm{arcsec}}\right) = (1.20\pm0.22)\log\left(\frac{\sigma_e}{\mathrm{kms}^{-1}}\right) - (0.79\pm0.09)\log\left(\frac{\langle I_e\rangle}{L_\odot \mathrm{pc}^{-2}}\right) - (7.74\pm0.83) \tag{6.3}$$

The errors were determined by a bootstrap procedure and the rms residuals in the y direction from the fit are 0.11 (12 per cent). The large errors are due to the small sample size. This projection of the data is shown in Figure 6.1.

6.3.1 Comparison to the literature

As discussed in Chapter 1 many authors have made independent determinations of the FP. I list just a small subset of these in Table 6.2. My FP determination is broadly consistent with the other results from the literature. Jorgensen et al.

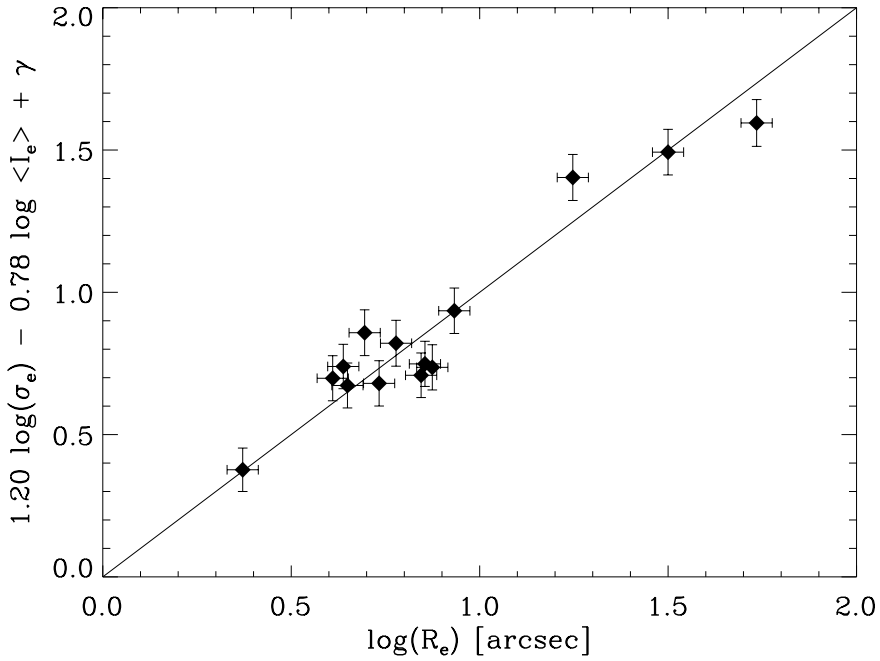

Figure 6.1: The FP determined from the SWIFT Coma ETG sample using a robust biweight fit. The error on σ_e was determined by pPXF (typically 7.5 per cent) and the R_e and I_e errors are based on the results of growth curve fits with different levels of sky subtraction. (typically 10 per cent in R_e and $\langle I_e \rangle$).

Table 6.2: FP determinations from other authors

Author	α	β	Sample Size	Notes
Djorgovski (1987)	1.39	-0.88	260	Mixed sample
Jorgensen (1996)	1.24	-0.82	226	Average over multiple clusters
Jorgensen (1996)	1.31	-0.84	79	Coma only
Bernadi (2003)	1.49	-0.75	$\sim$ 9000	SDSS, mixed sample with redshifts
Thomas (2011)	1.26	-0.72	16	Coma only

(1996) and Thomas et al. (2011) both determined the FP in Coma, so can be directly compared to this work. Jorgensen et al. (1996) used a sample of 79 ETGs with ground-based photometry and single aperture spectroscopy for each galaxy. Thomas et al. (2011) used a sample of 16 ETGs but made use of composite HST and ground-based photometry and multiple long slit apertures for each galaxy. My FP determination is consistent with both studies, with errors comparable to Thomas et al. (2011) and approximately twice those of Jorgensen et al. (1996). The larger range in σ_e covered by this sample compensates for the slightly larger sample size of Thomas et al. (2011).

6.3.2 Future work on the Fundamental Plane

I have three further goals for the SWIFT Coma FP study. These are:

i) Increase the sample size by carrying out further observations with SWIFT. A larger sample will allow a more accurate determination of the FP, as well as being important for the other principal aspect of this study, the environmental dependece of $\lambda_{\rm R}$ (discussed in detail below).

ii) Combining the MGE models described above with the IFU kinematics I intend to construct JAM models of all the SWIFT Coma ETGs. These JAM models will allow the dynamical M/L to be determined, which is closely related to the tilt of the FP. Recent studies have examined the Fundamental Mass Plane (replacing $\langle I_e \rangle$ with the surface mass density Σ_M in the FP determination; Bolton et al., 2007; Thomas et al., 2011) which appears to follow the Virial prediction. With the M/L values from the JAM models I will be able to determine the Fundamental Mass Plane for the Coma cluster.

iii) Examine the environmental dependence of the FP. By comparing the results of this study in a high density cluster to those of the SAURON FP study (Falcón-Barroso et al., in preparation) which has been carried out using iden-

tical analysis techniques it is possible to study any environmental dependence of the FP free from systematic effects.

6.4 Measuring $\lambda_{\rm R}$ - a kinematic classification scheme

As discussed in Chapter 1 it is possible to classify ETGs into different sub-classes based on their dynamical properties. One such classification system is based on the $\lambda_{\rm R}$ parameter, which quantifies the specific stellar angular momentum of a galaxy. Emsellem et al. (2007) classified ETGs into Slow Rotators (SRs, $\lambda_{\rm R} \leq 0.1$) and Fast Rotators (FRs, $\lambda_{\rm R} > 0.1$). This classification scheme was modified by Emsellem et al. (2011) to account for inclination effects; SRs were redefined as objects with $\lambda_{\rm R} \leq 0.31\sqrt{\epsilon}$ and FRs those objects with $\lambda_{\rm R}$ above this threshold. $\lambda_{\rm R}$ is defined as:

$$\lambda_{\rm R} \equiv \frac{\langle R|V|\rangle}{\langle R\sqrt{V^2+\sigma^2}\rangle} \tag{6.4}$$

Measured from two dimensional spectroscopy this becomes:

$$\lambda_{\rm R} = \frac{\sum_{i=1}^{N} F_i R_i |V_i|}{\sum_{i=1}^{N} F_i R_i \sqrt{V_i^2+\sigma_i^2}} \tag{6.5}$$

where F_i is the flux in the ith bin, R_i its distance to the centre and V_i and σ_i the stellar velocity and velocity dispersion of the bin. For large V, $\lambda_{\rm R}$ tends to 1. The normalisation, $\sqrt{V_i^2+\sigma_i^2}$ is a reasonable proxy for mass. $\lambda_{{\rm R}_e}$ is the $\lambda_{\rm R}$ value measured within an elliptical aperture of major axis radius $\rm R_e$ and ellipticity ϵ_e, or the largest elliptical aperture that fits within the extent of the IFU data, whichever is the smaller for a given galaxy. $\lambda_{\rm R}$ depends on the velocity structure of a galaxy as well as its global V/σ value.

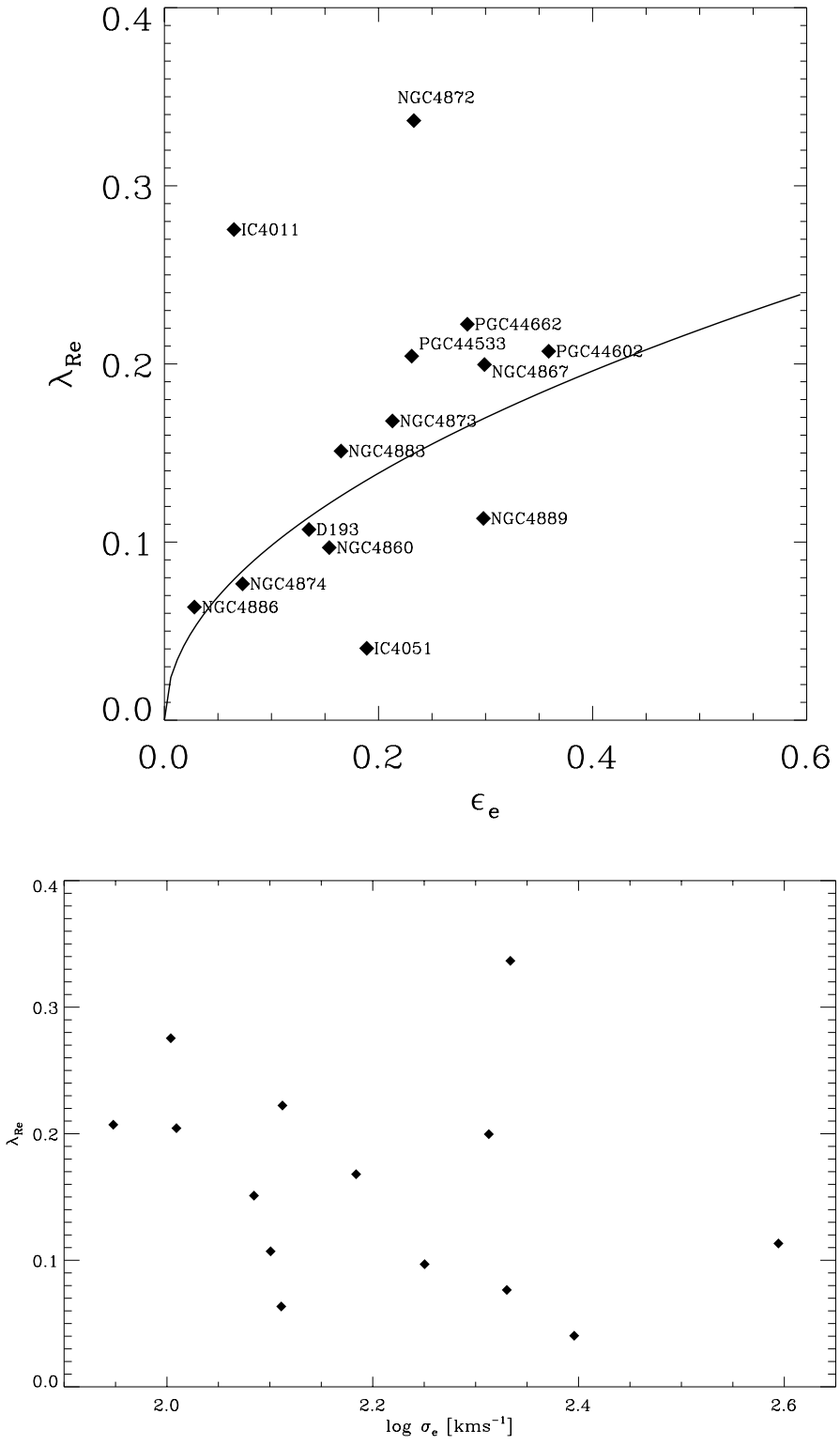

Figure 6.2: Upper panel: The λ_{R_e} - ϵ diagram for the SWIFT Coma ETG sample. The solid black line shows the divide between SRs and FRs given by $0.31\sqrt{\epsilon}$. Lower panel: λ_{R_e} vs σ_e. High σ_e galaxies tend to have lower λ_R, though there are low σ_e SRs and high σ_e FRs.

6.4.1 The Fast- and Slow-rotator distribution of Coma ETGs

I measured λ_{R_e} for the ETGs of the SWIFT Coma sample from the flux, velocity and velocity dispersion maps presented in the previous chapter. The λ_{R_e} values are given in Table 6.1, along with the galaxy's classification as either an SR or FR. The λ_{R_e} vs. ϵ_e diagram for the sample is shown in the upper panel of Figure 6.2, where the SR/FR divide is shown as the solid black line. Galaxies falling below this line were classified as SRs. There is no clear bimodality in Figure 6.2, but given the small sample size one would not necessarily expect ot see this behaviour. This is also consistent with the updated picture provided by Emsellem et al. (2011) from the ATLAS^{3D} survey, where a more subtle kinematic classification is put forward, compared to the obvious division found in the SAURON survey (Emsellem et al., 2007). The SR/FR classification agrees with the superficial impression from the v and σ maps, where all galaxies showing significant rotation are classified as FRs. The poor quality of the IFU data for Dressler193 makes its classification unreliable. The lower panel of Figure 6.2 shows the λ_{R_e} distribution of the sample as a function of σ_e. Excluding Dressler193 I found 4 SRs and 9 FRs in the SWIFT Coma ETG sample. This gave a SR fraction of 4/13 or 31 per cent. NGC4886, despite having a low value of λ_{R_e}, is extremely round ($\epsilon = 0.03$) and so likely to be very close to face on.

6.4.2 Environmental dependence of λ_R; comparison to the ATLAS^{3D} survey

The second primary science goal of the SWIFT Coma project is to explore the dependence of λ_R on environment. Coma is one of the densest environments in the local Universe ($\sim$ 10 times denser than the Virgo cluster) hence significantly expands the range of environments for which λ_R determinations are available. By comparing the SR/FR fraction found in Coma to the corresponding fraction in lower density

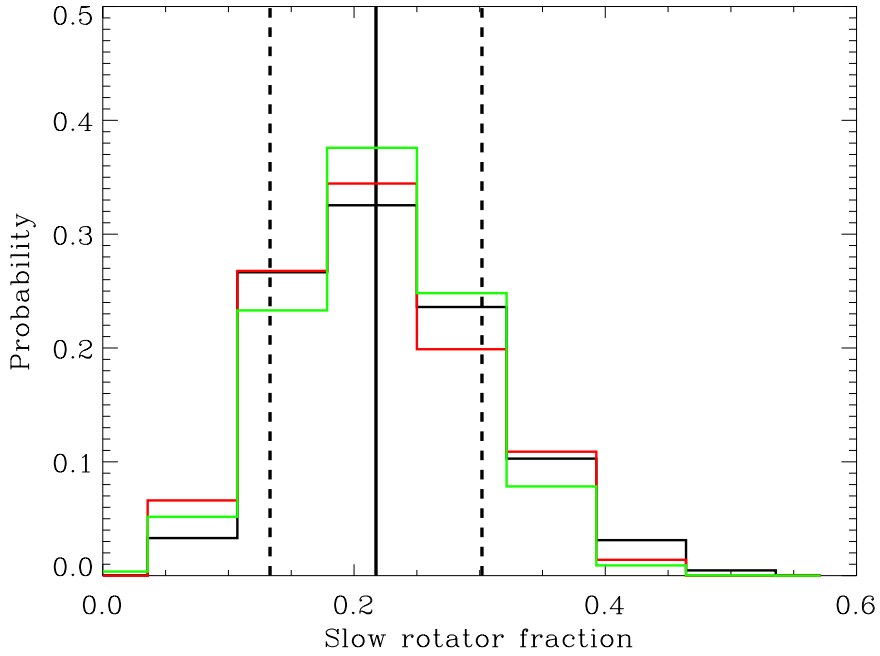

Figure 6.3: The slow rotator fraction (as a fraction of the total ETG population) expected to be observed in the ATLAS^{3D} sample if the SWIFT sample selection criteria had been used. The black histogram shows the results of randomly selecting subsamples of ATLAS^{3D} galaxies that satisfy the SWIFT Coma sample selection criteria. The green and red histograms show the same analysis for the non-Virgo and Virgo subsamples respectively. The expected slow rotator fraction and $1-\sigma$ bounds are shown as the solid and dashed vertical lines respectively. The expected slow rotator fraction for the full sample is 0.22.

environments from the ATLAS^{3D} survey the variation of λ_R can be explored over a wide range of local environmental densities.

Because I have observed only a small fraction of the total ETG population of the Coma cluster it was first necessary to match the SWIFT Coma ETG sample to the ATLAS^{3D} sample. The simplest way to accomplish this was to map the sample selection criteria I used to select the Coma sample to the ATLAS^{3D} sample and compare the expected SR/FR fraction in the two samples under the same sample selection criteria. For this analysis I chose to divide the ATLAS^{3D} sample into Virgo and non-Virgo subsamples to provide three independent environmental densities.

The SWIFT Coma ETG sample was selected based on central velocity dispersion (see the previous Chapter for details). Using the central velocity dispersions for the

ATLAS^{3D} sample obtained from the SAURON data (Cappellari, private communication) I used a Monte Carlo technique to extract samples of galaxies matching the Coma sample selection criteria from both the Virgo and non-Virgo ATLAS^{3D} samples. For each subset of galaxies I determined the SR/FR fraction, determining the likelihood of 'observing' a given SR/FR fraction given the underlying FR/SR and σ distribution of the two samples and the SWIFT Coma selection criteria. The results of this analysis are shown in Figure 6.3; where the histogram shows the results of the Monte Carlo analysis and the mean SR/FR fraction and $1-\sigma$ bounds are shown as the vertical solid and dashed lines respectively. Because of the relatively small sample size of the SWIFT Coma ETG sample the 1-σ bounds are large. There is little difference between the full, Virgo and non-Virgo samples which is unsurprising given that Cappellari et al. (2011b) found an increase in the SR fraction only in the very core of Virgo. It is interesting to note that the mean slow rotator fraction in Virgo is only 16 per cent, however this rises to 31 per cent when considering only the core.

In Figure 6.4 I plot the mean expected FR/SR fraction for each environment against the projected local environmental density. Densities for the Virgo and non-Virgo ATLAS^{3D} samples are taken from Cappellari et al. (2011b) and the mean density of the Coma cluster is taken from Conselice & Gallagher (1998). In order to properly examine the environmental dependence of λ_R I require a more discriminatory measure of the local environment than the coarse measure used in Figure 6.4. Unfortunately the small sample size does not allow the FR/SR fraction to be determined in Coma with a finer density measure with any degree of accuracy. As mentioned above I intend to expand the sample with further SWIFT observations of Coma ETGs, focusing on improved sampling of the range of environmental densities found in the Coma cluster.

It is also interesting to ask, what is the likelihood of observing a SR fraction of 31 per cent given the SWIFT Coma sample selection criteria? Using the Monte-

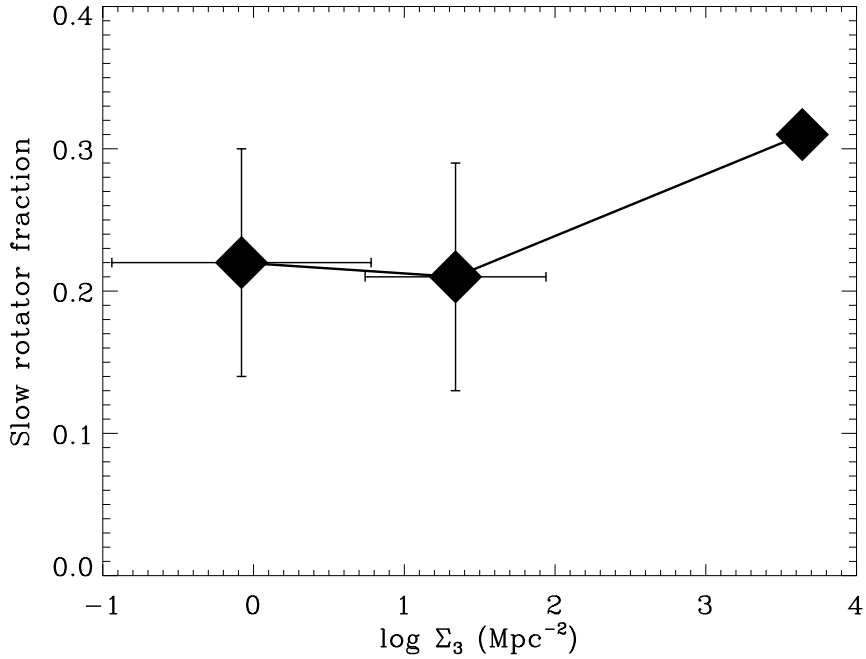

Figure 6.4: The dependence of the slow rotator fraction on the local environment, quantified using Σ_3 (defined in Section 4.4.4. The first two points show the results from the non-Virgo and Virgo ATLAS^{3D} subsamples. The third point is from the SWIFT Coma ETG sample. No error bars are shown for the Coma datapoint because the incomplete information available on the cluster does not allow the errors to be easily quantified.

Carlo technique above I constructed cumulative frequency histograms showing the probability of observing a SR fraction less than a given value for the full, Virgo and non-Virgo ATLAS^{3D} samples. This is shown in Figure 6.5. The SR fraction for the sample is shown as a solid vertical line. The black curve is a polynomial fit to the cumulative frequency histogram for the full ATLAS^{3D} sample. If I had observed the ATLAS^{3D} sample with the same selection criteria as in this sample the probability that I would have observed an equal or higher SR fraction is only 33 per cent. This suggests the Coma cluster has a higher fraction of slow rotators than the lower density environments sampled by the ATLAS^{3D} survey, but improved statistics from a larger sample will be required to confirm this result.

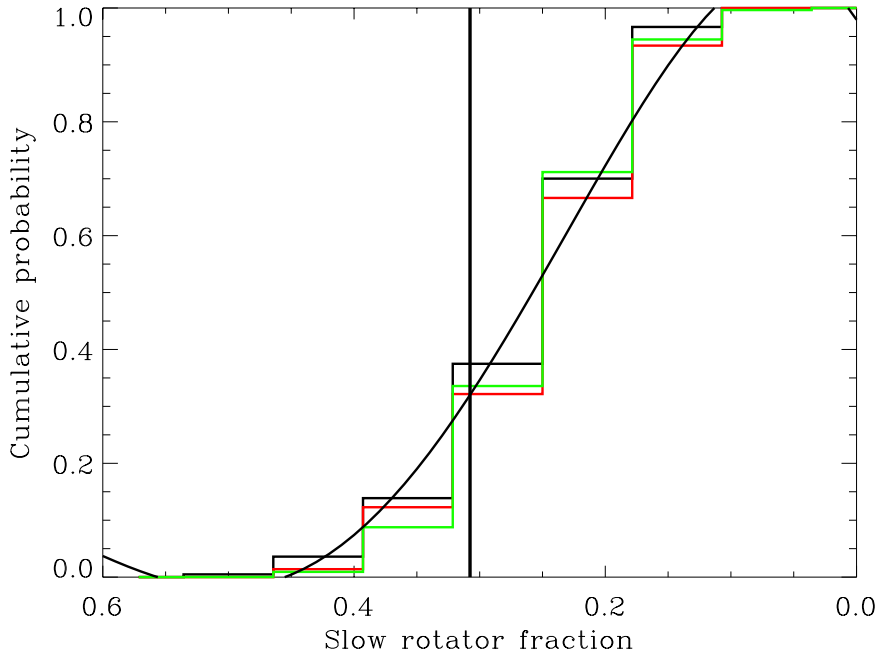

Figure 6.5: Cumulative probability histogram (based on the Monte-Carlo analysis shown in Figure 6.3) showing the probability of observing a SR fraction equal to or greater than a given value. The black histogram shows the results for the full ATLAS^{3D} sample, while the green and red histograms show the non-Virgo and Virgo subsamples respectively. The smooth curve is a fit to the black histogram. The black vertical line indicates the SR fraction found in the SWIFT Coma ETG sample.

Chapter 7

Conclusions

In Chapter 1 I presented the two general areas of galaxy evolution I wished to investigate: how the dynamical properties of ETGs are related to their stellar population properties and what effect, if any, the local environment of an ETG has on these properties. In the course of this work I have refined these general topics into three specific questions. These are:

- What is the relationship between the local gravitational potential, quantified by V_{esc}, and the stellar populations of ETGs?
- Are these relationships influenced by any of the other properties of these galaxies?
- Do ETGs in high-density environments have different properties than similar galaxies in lower density environments?

In attempting to answer these questions I have made extensive use of IFU spectroscopy, complemented by optical photometry and a wide range of multiwavelength data. In this thesis I have presented answers to some of these questions and evidence suggesting partial answers for the others. The previous chapters divide neatly into two parts. Chapters 2, 3 and 4 explore the role of V_{esc} in ETGs using the SAURON and ATLAS^{3D} surveys. Chapters 5 and 6 describe the IFU observations and analy-

sis of a sample of ETGs in the Coma cluster. In this chapter I will summarise the results presented in this work, address how those results answer the above questions and briefly discuss how I intend to proceed in filling in any remaining unanswered questions.

7.1 Empirical relations

In Chapter 3 I examined the correlation of stellar population properties with V_{esc}. I found that the three absorption line strength indices covered by the SAURON spectral range, Mgb, Fe5015 and Hβ, all correlate tightly with V_{esc}. The scatter in all three relations is comparable to that in other relations found between dynamical and stellar population properties of ETGs such as the colour-magnitude relation and the mass-metallicity relation. In the case of Mgb this correlation is both global and local; the relation is the same both within individual galaxies and between different galaxies. This is not the case for the Fe5015 and Hβ indices; the gradients within individual galaxies are respectively steeper and shallower than the corresponding global relation. This scale-independent behaviour of the Mgb-V_{esc} relation suggests a tight link between the depth of the local gravitational potential well and the star formation history of ETGs.

Using the volume limited ATLAS^{3D} sample with its extensive SDSS photometric coverage, I found (in Chapter 4) a correlation between the local colour in an ETG and V_{esc}. The colour-V_{esc} relations exhibited the same local and global behaviour as the Mgb-V_{esc} relation. That this behaviour is found between V_{esc} and several different stellar population indicators is compelling evidence that these observations reflect some physical process that connects the depth of the local potential to an ETG's stellar population.

To understand what is driving the Index-V_{esc} relations I turned to SSP modelling to examine the dependence of age, metallicity and alpha enhancement on V_{esc}. I

found a reasonable correlation between [Z/H] and V_{esc}, though with more scatter than the Mgb-V_{esc} relation. The trends with t and [α/Fe] were much weaker and complicated by the limitations of the SSP models. Despite the correlation between [Z/H] and V_{esc} this relation did not reproduce the local and global behaviour of the Mgb-V_{esc} relation. However, by choosing a suitable combination of [Z/H] with t (or [α/Fe]) I was able to reproduce the local and global behaviour and the small scatter of the Mgb-V_{esc} relation. When this constraint was applied and the SSP models were inverted the observed line strength - V_{esc} relations were recovered.

Using the SSP models I was able to explore how constraints on the SSP parameters would affect the observed relations. Fixing t or [α/Fe] had little effect on the observed relation (except at very young ages – see below), however when [Z/H] was fixed the relation broke down. This is consistent with the correlation between [Z/H] and V_{esc} and the mass-metallicity relation reported by other authors. It is unclear why additional parameters are required to reproduce the local and global connection found in the observations.

7.1.1 Factors affecting the Mgb-V_{esc} relation

Because of the local and global behaviour I focused the remainder of my analysis on the Mgb-V_{esc} relation. I examined under what conditions the relation remains unchanged and what, if anything, can cause the breakdown of the relation. Few internal properties of ETGs appear to affect the relation. I found no dependence on a wide range of properties including, but not limited to: classification (both morphological and kinematic), size, mass, luminosity and apparent flattening. Those parameters that do have an effect on the relation do so in two ways: by affecting the internal gradients of galaxies or as a systematic offset from the relation while preserving the internal gradient.

The only parameter that was found to significantly affect internal gradients was the presence of recent star formation, typically centrally concentrated, indicated by

high central Hβ values and young central ages. Galaxies with recent star formation all showed strongly negative Mgb-V_{esc} gradients. These negative gradient galaxies also have lower metallicities and higher molecular gas masses and dust content than typical ETGs. Using SSP modelling I demonstrated that for the majority of these galaxies the deviation from the Mgb-V_{esc} relation was a temporary phenomenon and passive ageing will return these galaxies to the relation. This is consistent with the idea that the young population represents a perturbation to an underlying older population that is dominant by mass. As the young population ages and fades the old stars will come to dominate the light of the galaxy and it will return to the relation.

I found several parameters that influenced the absolute deviation of a galaxy from the Mgb-V_{esc} relation without affecting the galaxy's internal gradient. The strongest correlations of the residuals were found with local environment and [α/Fe]. At fixed V_{esc}, galaxies in higher density environments were enhanced in Mgb over galaxies in low density environments. Similarly, at fixed V_{esc} galaxies with higher [α/Fe] were also enhanced in Mgb. This is consistent with the picture of Thomas et al. (2005), where galaxies in higher density environments experience more rapid or more efficient star formation. The residuals from the Mgb-V_{esc} relation show that this effect occurs to the same degree throughout an entire galaxy while the underlying global and local connection is preserved.

7.2 Environmental influences on early-type galaxy properties

While some environmental effects were observed in the ATLAS^{3D} survey, including the effect described above, the sample does not probe the densest environments. I observed a sample of 14 ETGs in the nearby Coma cluster, the densest cluster in the local Universe, to expand the range of environments for which IFU observations

are available. While the Coma sample is incomplete and relatively small, combined with the ATLAS^{3D} sample it can be used to study the effect of environment on the kinematic and dynamical properties of ETGs.

I first examined the slow rotator fraction (N_{SR}/N_{ETG}) as a function of environment. I found that the SR fraction of 31 per cent observed in the Coma cluster was significantly higher than that expected in the Virgo (20 per cent) and non-Virgo (21 per cent) ATLAS^{3D} samples. Taking into account the incompleteness of the Coma sample, I found that the probability that the SR fraction is higher in the Coma cluster than in the ATLAS^{3D} sample is 67 per cent. However, Cappellari et al. (2011b) find that the SR fraction increases significantly (to 31 per cent) only in the core of the Virgo cluster. The current Coma sample is too small to study the variation of environmental density within the cluster; it will be necessary to expand the sample to probe the local density on a finer scale. Accurately determining the density threshold at which the SR fraction begins to increase will provide important constraints on the mechanism(s) that form SRs. Whether the SR fraction continues to increase with density above this threshold is as yet unknown

I also examined the FP of galaxies within the Coma cluster. Though the sample is small, the large range in σ_e sampled and the availability of IFU data allow the FP to be determined with an accuracy comparable to that of much larger samples. Increasing the sample size is desirable to further reduce these errors. The FP in the Coma cluster is given by: $\log R_e = (1.20 \pm 0.22) \log \sigma_e - (0.79 \pm 0.09) \log \langle I_e \rangle$. This is consistent with other determinations of the FP in the Coma cluster. This analysis was carried out in an identical fashion to a study of the FP in the SAURON survey (Falcón-Barroso et al., in preparation) which will allow direct investigation of the environmental dependence of the FP free from any systematic differences between the two studies.

7.3 Final conclusions

I will now consider how the results summarised above address the three questions I proposed at the start of this chapter. I found that the stellar populations of ETGs are closely linked to the depth of the local gravitational potential. This correlation appears to be predominantly driven by the local metallicity, however the age and abundance pattern also play a role. It is not clear what physical process gives rise to this correlation, though chemical evolution models based on the monolithic collapse scenario of galaxy formation do qualitatively reproduce the observations.

The dependence of the stellar populations on the local potential seems robust, in the sense that the result holds across a wide range of galaxy types and properties. Recent star formation is the only effect that completely destroys the connection, however this appears to be a temporary effect, and as galaxies age they will return to the relation. Simple analytic models and simulations both suggest that a limited amount of dry merging will not disrupt the relation, though galaxies will be systematically shifted to higher V_{esc} at constant Mgb. This result, combined with the observed scatter in the relation, provides a constraint on the major dry mergers a typical ETG can have experienced which is consistent with other estimates of major merger rates.

The local environmental density appears to influence both the stellar populations and kinematics of ETGs, though the effects are subtle. ETGs in high density environments or with high [α/Fe] are enhanced in Mgb at fixed V_{esc}. This is true across the full range of environmental densities sampled by the ATLAS^{3D} survey. In contrast, the kinematic properties of ETGs are only affected by the highest densities. The SR fraction only increases in the dense environment of the Coma cluster (and the core of the Virgo cluster; Cappellari et al., 2011b).

In this work I have presented tantalising evidence of the environmental and dynamical dependence of ETG galaxy properties. Interpreting this evidence is not straightforward, and to draw firm conclusions about the physical processes of ETG

formation and evolution requires further work. In the case of the environmental effects this predominantly means further observations to expand the sample, improve the accuracy of the results and fully sample the range of environmental densities found in the local Universe. For the local gravitational potential effects it is the interpretation that remains unclear. While the empirical relations are robust, the interpretation via stellar population modelling requires further work both observationally and from simulations.

Bibliography

Abazajian, K. N., Adelman-McCarthy, J. K., Agüeros, M. A., Allam, S. S., Allende Prieto, C., An, D., Anderson, K. S. J., Anderson, S. F., Annis, J., Bahcall, N. A., & et al. 2009, ApJS, 182, 543

Abraham, R. G., Valdes, F., Yee, H. K. C., & van den Bergh, S. 1994, ApJ, 432, 75

Alpher, R. A., Bethe, H., & Gamow, G. 1948, Physical Review, 73, 803

Andrae, R., Jahnke, K., & Melchior, P. 2011, MNRAS, 411, 385

Astier, P., Guy, J., Regnault, N., Pain, R., Aubourg, E., Balam, D., Basa, S., Carlberg, R. G., Fabbro, S., Fouchez, D., Hook, I. M., Howell, D. A., Lafoux, H., Neill, J. D., Palanque-Delabrouille, N., Perrett, K., Pritchet, C. J., Rich, J., Sullivan, M., Taillet, R., Aldering, G., Antilogus, P., Arsenijevic, V., Balland, C., Baumont, S., Bronder, J., Courtois, H., Ellis, R. S., Filiol, M., Gonçalves, A. C., Goobar, A., Guide, D., Hardin, D., Lusset, V., Lidman, C., McMahon, R., Mouchet, M., Mourao, A., Perlmutter, S., Ripoche, P., Tao, C., & Walton, N. 2006, A&A, 447, 31

Bacon, R., Copin, Y., Monnet, G., Miller, B. W., Allington-Smith, J. R., Bureau, M., Carollo, C. M., Davies, R. L., Emsellem, E., Kuntschner, H., Peletier, R. F., Verolme, E. K., & de Zeeuw, P. T. 2001, MNRAS, 326, 23

Baldry, I. K., Glazebrook, K., Brinkmann, J., Ivezić, Ž., Lupton, R. H., Nichol, R. C., & Szalay, A. S. 2004, ApJ, 600, 681

Balogh, M. L., Morris, S. L., Yee, H. K. C., Carlberg, R. G., & Ellingson, E. 1999, ApJ, 527, 54

Barnes, J. E. 1988, ApJ, 331, 699

Bell, E. F., McIntosh, D. H., Katz, N., & Weinberg, M. D. 2003, ApJS, 149, 289

Bender, R., Burstein, D., & Faber, S. M. 1992, ApJ, 399, 462

—. 1993, ApJ, 411, 153

Bender, R., Surma, P., Doebereiner, S., Moellenhoff, C., & Madejsky, R. 1989, A&A, 217, 35

Bernardi, M., Nichol, R. C., Sheth, R. K., Miller, C. J., & Brinkmann, J. 2006, AJ, 131, 1288

Bernardi, M., Sheth, R. K., Annis, J., Burles, S., Eisenstein, D. J., Finkbeiner, D. P., Hogg, D. W., Lupton, R. H., Schlegel, D. J., SubbaRao, M., Bahcall, N. A., Blakeslee, J. P., Brinkmann, J., Castander, F. J., Connolly, A. J., Csabai, I., Doi, M., Fukugita, M., Frieman, J., Heckman, T., Hennessy, G. S., Ivezić, Ž., Knapp, G. R., Lamb, D. Q., McKay, T., Munn, J. A., Nichol, R., Okamura, S., Schneider, D. P., Thakar, A. R., & York, D. G. 2003, AJ, 125, 1866

Bershady, M. A., Jangren, A., & Conselice, C. J. 2000, AJ, 119, 2645

Bertola, F. & Capaccioli, M. 1975, ApJ, 200, 439

Binney, J. 1977, ApJ, 215, 483

Binney, J. 1979, in Photometry, Kinematics and Dynamics of Galaxies, ed. D. S. Evans, 357

—. 1985, MNRAS, 212, 767

Binney, J. & Tremaine, S. 1987, Galactic dynamics (Princeton)

Binney, J. J., Davies, R. L., & Illingworth, G. D. 1990, ApJ, 361, 78

Blanton, M. R., Dalcanton, J., Eisenstein, D., Loveday, J., Strauss, M. A., SubbaRao, M., Weinberg, D. H., Anderson, Jr., J. E., Annis, J., Bahcall, N. A., Bernardi, M., Brinkmann, J., Brunner, R. J., Burles, S., Carey, L., Castander, F. J., Connolly, A. J., Csabai, I., Doi, M., Finkbeiner, D., Friedman, S., Frieman, J. A., Fukugita, M., Gunn, J. E., Hennessy, G. S., Hindsley, R. B., Hogg, D. W., Ichikawa, T., Ivezić, Ž., Kent, S., Knapp, G. R., Lamb, D. Q., Leger, R. F., Long, D. C., Lupton, R. H., McKay, T. A., Meiksin, A., Merelli, A., Munn, J. A., Narayanan, V., Newcomb, M., Nichol, R. C., Okamura, S., Owen, R., Pier, J. R., Pope, A., Postman, M., Quinn, T., Rockosi, C. M., Schlegel, D. J., Schneider, D. P., Shimasaku, K., Siegmund, W. A., Smee, S., Snir, Y., Stoughton, C., Stubbs, C., Szalay, A. S., Szokoly, G. P., Thakar, A. R., Tremonti, C., Tucker, D. L., Uomoto, A., Vanden Berk, D., Vogeley, M. S., Waddell, P., Yanny, B., Yasuda, N., & York, D. G. 2001, AJ, 121, 2358

Bois, M., Bournaud, F., Emsellem, E., Alatalo, K., Blitz, L., Bureau, M., Cappellari, M., Davies, R. L., Davis, T. A., de Zeeuw, P. T., Duc, P., Khochfar, S., Krajnović, D., Kuntschner, H., Lablanche, P., McDermid, R. M., Morganti, R., Naab, T., Oosterloo, T., Sarzi, M., Scott, N., Serra, P., Weijmans, A., & Young, L. M. 2010, MNRAS, 406, 2405

Bolton, A. S., Burles, S., Treu, T., Koopmans, L. V. E., & Moustakas, L. A. 2007, ApJ, 665, L105

Bower, R. G., Benson, A. J., Malbon, R., Helly, J. C., Frenk, C. S., Baugh, C. M., Cole, S., & Lacey, C. G. 2006, MNRAS, 370, 645

Bower, R. G., Kodama, T., & Terlevich, A. 1998, MNRAS, 299, 1193

Bower, R. G., Lucey, J. R., & Ellis, R. S. 1992, MNRAS, 254, 601

Bundy, K., Ellis, R. S., Conselice, C. J., Taylor, J. E., Cooper, M. C., Willmer, C. N. A., Weiner, B. J., Coil, A. L., Noeske, K. G., & Eisenhardt, P. R. M. 2006, ApJ, 651, 120

Bunker, A. J., Stanway, E. R., Ellis, R. S., & McMahon, R. G. 2004, MNRAS, 355, 374

Butcher, H. & Oemler, Jr., A. 1978, ApJ, 226, 559

—. 1984, ApJ, 285, 426

Cappellari, M. 2002, MNRAS, 333, 400

—. 2008, MNRAS, 390, 71

Cappellari, M., Bacon, R., Bureau, M., Damen, M. C., Davies, R. L., de Zeeuw, P. T., Emsellem, E., Falcón-Barroso, J., Krajnović, D., Kuntschner, H., McDermid, R. M., Peletier, R. F., Sarzi, M., van den Bosch, R. C. E., & van de Ven, G. 2006, MNRAS, 366, 1126

Cappellari, M. & Copin, Y. 2003, MNRAS, 342, 345

Cappellari, M., di Serego Alighieri, S., Cimatti, A., Daddi, E., Renzini, A., Kurk, J. D., Cassata, P., Dickinson, M., Franceschini, A., Mignoli, M., Pozzetti, L., Rodighiero, G., Rosati, P., & Zamorani, G. 2009, ApJ, 704, L34

Cappellari, M. & Emsellem, E. 2004, PASP, 116, 138

Cappellari, M., Emsellem, E., Bacon, R., Bureau, M., Davies, R. L., de Zeeuw, P. T., Falcón-Barroso, J., Krajnović, D., Kuntschner, H., McDermid, R. M., Peletier, R. F., Sarzi, M., van den Bosch, R. C. E., & van de Ven, G. 2007, MNRAS, 379, 418

Cappellari, M., Emsellem, E., Krajnović, D., McDermid, R. M., Scott, N., Verdoes Kleijn, G. A., Young, L. M., Alatalo, K., Bacon, R., Blitz, L., Bois, M., Bournaud, F., Bureau, M., Davies, R. L., Davis, T. A., de Zeeuw, P. T., Duc, P.-A., Khochfar, S., Kuntschner, H., Lablanche, P.-Y., Morganti, R., Naab, T., Oosterloo, T., Sarzi, M., Serra, P., & Weijmans, A.-M. 2011a, MNRAS, 413, 813

Cappellari, M., Emsellem, E., Krajnović, D., McDermid, R. M., Serra, P., Alatalo, K., Blitz, L., Bois, M., Bournaud, F., Bureau, M., Davies, R. L., Davis, T. A., de Zeeuw, P. T., Khochfar, S., Kuntschner, H., Lablanche, P.-Y., Morganti, R., Naab, T., Oosterloo, T., Sarzi, M., Scott, N., Weijmans, A.-M., & Young, L. M. 2011b, ArXiv, 1104.3545

Cappellari, M., Verolme, E. K., van der Marel, R. P., Kleijn, G. A. V., Illingworth, G. D., Franx, M., Carollo, C. M., & de Zeeuw, P. T. 2002, ApJ, 578, 787

Carollo, C. M. & Danziger, I. J. 1994, MNRAS, 270, 523

Carollo, C. M., Franx, M., Illingworth, G. D., & Forbes, D. A. 1997, ApJ, 481, 710

Cenarro, A. J., Cardiel, N., Gorgas, J., Peletier, R. F., Vazdekis, A., & Prada, F. 2001, MNRAS, 326, 959

Cimatti, A., Daddi, E., & Renzini, A. 2006, A&A, 453, L29

Cole, S., Aragon-Salamanca, A., Frenk, C. S., Navarro, J. F., & Zepf, S. E. 1994, MNRAS, 271, 781

Coles, P. 2005, Nature, 433, 248

Colless, M., Burstein, D., Davies, R. L., McMahan, R. K., Saglia, R. P., & Wegner, G. 1999, MNRAS, 303, 813

Conselice, C. J. & Gallagher, III, J. S. 1998, MNRAS, 297, L34

Copi, C. J., Schramm, D. N., & Turner, M. S. 1995, Science, 267, 192

Côté, P., McLaughlin, D. E., Cohen, J. G., & Blakeslee, J. P. 2003, ApJ, 591, 850

Cowie, L. L. & Barger, A. J. 2008, ApJ, 686, 72

Cowie, L. L., Songaila, A., Hu, E. M., & Cohen, J. G. 1996, AJ, 112, 839

Crockett, R. M., Kaviraj, S., Silk, J. I., Whitmore, B. C., O'Connell, R. W., Mutchler, M., Balick, B., Bond, H. E., Calzetti, D., Carollo, C. M., Disney, M. J., Dopita, M. A., Frogel, J. A., Hall, D. N. B., Holtzman, J. A., Kimble, R. A., McCarthy, P. J., Paresce, F., Saha, A., Trauger, J. T., Walker, A. R., Windhorst, R. A., Young, E. T., Jeong, H., & Yi, S. K. 2011, ApJ, 727, 115

Croton, D. J., Springel, V., White, S. D. M., De Lucia, G., Frenk, C. S., Gao, L., Jenkins, A., Kauffmann, G., Navarro, J. F., & Yoshida, N. 2006, MNRAS, 365, 11

Curtis, H. D. 1921, Bulletin of the National Research Council, 2, 194

Daddi, E., Renzini, A., Pirzkal, N., Cimatti, A., Malhotra, S., Stiavelli, M., Xu, C., Pasquali, A., Rhoads, J. E., Brusa, M., di Serego Alighieri, S., Ferguson, H. C., Koekemoer, A. M., Moustakas, L. A., Panagia, N., & Windhorst, R. A. 2005, ApJ, 626, 680

Davies, R. I. 2007, MNRAS, 375, 1099

Davies, R. L., Efstathiou, G., Fall, S. M., Illingworth, G., & Schechter, P. L. 1983, ApJ, 266, 41

Davies, R. L., Sadler, E. M., & Peletier, R. F. 1993, MNRAS, 262, 650

Davis, M., Efstathiou, G., Frenk, C. S., & White, S. D. M. 1985, ApJ, 292, 371

de Vaucouleurs, G. 1948, Annales d'Astrophysique, 11, 247

de Vaucouleurs, G., de Vaucouleurs, A., Corwin, Jr., H. G., Buta, R. J., Paturel, G., & Fouque, P. 1991, Third Reference Catalogue of Bright Galaxies

de Zeeuw, P. T., Bureau, M., Emsellem, E., Bacon, R., Carollo, C. M., Copin, Y., Davies, R. L., Kuntschner, H., Miller, B. W., Monnet, G., Peletier, R. F., & Verolme, E. K. 2002, MNRAS, 329, 513

Dekel, A. & Silk, J. 1986, ApJ, 303, 39

Djorgovski, S. & Davis, M. 1987, ApJ, 313, 59

Dolphin, A. E. 2000, PASP, 112, 1397

Dressler, A. 1980, ApJ, 236, 351

Dressler, A., Lynden-Bell, D., Burstein, D., Davies, R. L., Faber, S. M., Terlevich, R., & Wegner, G. 1987, ApJ, 313, 42

Eisenstein, D. J., Zehavi, I., Hogg, D. W., Scoccimarro, R., Blanton, M. R., Nichol, R. C., Scranton, R., Seo, H.-J., Tegmark, M., Zheng, Z., Anderson, S. F., Annis, J., Bahcall, N., Brinkmann, J., Burles, S., Castander, F. J., Connolly, A., Csabai, I., Doi, M., Fukugita, M., Frieman, J. A., Glazebrook, K., Gunn, J. E., Hendry, J. S., Hennessy, G., Ivezić, Z., Kent, S., Knapp, G. R., Lin, H., Loh, Y.-S., Lupton, R. H., Margon, B., McKay, T. A., Meiksin, A., Munn, J. A., Pope, A., Richmond, M. W., Schlegel, D., Schneider, D. P., Shimasaku, K., Stoughton, C., Strauss, M. A., SubbaRao, M., Szalay, A. S., Szapudi, I., Tucker, D. L., Yanny, B., & York, D. G. 2005, ApJ, 633, 560

Emsellem, E., Cappellari, M., Krajnović, D., Alatalo, K., Blitz, L., Bois, M., Bournaud, F., Bureau, M., Davies, R. L., Davis, T. A., de Zeeuw, P. T., Khochfar, S., Kuntschner, H., Lablanche, P., McDermid, R. M., Morganti, R., Naab, T., Oosterloo, T., Sarzi, M., Scott, N., Serra, P., van de Ven, G., Weijmans, A., & Young, L. M. 2011, ArXi, 1102.4444

Emsellem, E., Cappellari, M., Krajnović, D., van de Ven, G., Bacon, R., Bureau, M., Davies, R. L., de Zeeuw, P. T., Falcón-Barroso, J., Kuntschner, H., McDermid, R., Peletier, R. F., & Sarzi, M. 2007, MNRAS, 379, 401

Emsellem, E., Cappellari, M., Peletier, R. F., McDermid, R. M., Bacon, R., Bureau, M., Copin, Y., Davies, R. L., Krajnović, D., Kuntschner, H., Miller, B. W., & de Zeeuw, P. T. 2004, MNRAS, 352, 721

Emsellem, E., Monnet, G., & Bacon, R. 1994, A&A, 285, 723

Evrard, A. E., Metzler, C. A., & Navarro, J. F. 1996, ApJ, 469, 494

Faber, S. M. 1973, ApJ, 179, 731

Faber, S. M. & Gallagher, J. S. 1976, ApJ, 204, 365

Faber, S. M. & Jackson, R. E. 1976, ApJ, 204, 668

Faber, S. M., Willmer, C. N. A., Wolf, C., Koo, D. C., Weiner, B. J., Newman, J. A., Im, M., Coil, A. L., Conroy, C., Cooper, M. C., Davis, M., Finkbeiner, D. P., Gerke, B. F., Gebhardt, K., Groth, E. J., Guhathakurta, P., Harker, J., Kaiser, N., Kassin, S., Kleinheinrich, M., Konidaris, N. P., Kron, R. G., Lin, L., Luppino, G., Madgwick, D. S., Meisenheimer, K., Noeske, K. G., Phillips, A. C., Sarajedini, V. L., Schiavon, R. P., Simard, L., Szalay, A. S., Vogt, N. P., & Yan, R. 2007, ApJ, 665, 265

Fan, X., Narayanan, V. K., Lupton, R. H., Strauss, M. A., Knapp, G. R., Becker, R. H., White, R. L., Pentericci, L., Leggett, S. K., Haiman, Z., Gunn, J. E., Ivezić, Ž., Schneider, D. P., Anderson, S. F., Brinkmann, J., Bahcall, N. A., Connolly, A. J., Csabai, I., Doi, M., Fukugita, M., Geballe, T., Grebel, E. K., Harbeck, D., Hennessy, G., Lamb, D. Q., Miknaitis, G., Munn, J. A., Nichol, R., Okamura, S., Pier, J. R., Prada, F., Richards, G. T., Szalay, A., & York, D. G. 2001a, AJ, 122, 2833

Fan, X., Strauss, M. A., Schneider, D. P., Gunn, J. E., Lupton, R. H., Becker, R. H., Davis, M., Newman, J. A., Richards, G. T., White, R. L., Anderson, Jr., J. E., Annis, J., Bahcall, N. A., Brunner, R. J., Csabai, I., Hennessy, G. S., Hindsley, R. B., Fukugita, M., Kunszt, P. Z., Ivezić, Ž., Knapp, G. R., McKay, T. A., Munn, J. A., Pier, J. R., Szalay, A. S., & York, D. G. 2001b, AJ, 121, 54

Francis, P. J. & Wills, B. J. 1999, in Astronomical Society of the Pacific Conference Series, Vol. 162, Quasars and Cosmology, ed. G. Ferland & J. Baldwin, 363

Franx, M. & Illingworth, G. 1990, ApJ, 359, L41

Fukugita, M., Hogan, C. J., & Peebles, P. J. E. 1998, ApJ, 503, 518

Gamow, G. 1948, Nature, 162, 680

Gerhard, O., Kronawitter, A., Saglia, R. P., & Bender, R. 2001, AJ, 121, 1936

Giavalisco, M., Dickinson, M., Ferguson, H. C., Ravindranath, S., Kretchmer, C., Moustakas, L. A., Madau, P., Fall, S. M., Gardner, J. P., Livio, M., Papovich, C., Renzini, A., Spinrad, H., Stern, D., & Riess, A. 2004, ApJ, 600, L103

Glazebrook, K., Abraham, R. G., McCarthy, P. J., Savaglio, S., Chen, H.-W., Crampton, D., Murowinski, R., Jørgensen, I., Roth, K., Hook, I., Marzke, R. O., & Carlberg, R. G. 2004, Nature, 430, 181

Gómez, P. L., Nichol, R. C., Miller, C. J., Balogh, M. L., Goto, T., Zabludoff, A. I., Romer, A. K., Bernardi, M., Sheth, R., Hopkins, A. M., Castander, F. J., Connolly, A. J., Schneider, D. P., Brinkmann, J., Lamb, D. Q., SubbaRao, M., & York, D. G. 2003, ApJ, 584, 210

Graham, A. W. & Driver, S. P. 2005, PASA, 22, 118

Hammer, D., Verdoes Kleijn, G., Hoyos, C., den Brok, M., Balcells, M., Ferguson, H. C., Goudfrooij, P., Carter, D., Guzmán, R., Peletier, R. F., Smith, R. J., Graham, A. W., Trentham, N., Peng, E., Puzia, T. H., Lucey, J. R., Jogee, S., Aguerri, A. L., Batcheldor, D., Bridges, T. J., Chiboucas, K., Davies, J. I., del Burgo, C., Erwin, P., Hornschemeier, A., Hudson, M. J., Huxor, A., Jenkins, L., Karick, A., Khosroshahi, H., Kourkchi, E., Komiyama, Y., Lotz, J., Marzke, R. O., Marinova, I., Matkovic, A., Merritt, D., Miller, B. W., Miller, N. A., Mobasher, B., Mouhcine, M., Okamura, S., Percival, S., Phillipps, S., Poggianti, B. M., Price, J., Sharples, R. M., Tully, R. B., & Valentijn, E. 2010, ApJS, 191, 143

Hanuschik, R. W. 2003, A&A, 407, 1157

Hernquist, L. 1990, ApJ, 356, 359

Hopkins, P. F., Lauer, T. R., Cox, T. J., Hernquist, L., & Kormendy, J. 2009, ApJS, 181, 486

Hubble, E. 1929, Proceedings of the National Academy of Sciences of America, 168

Hubble, E. P. 1936, Realm of the Nebulae

Im, M., Simard, L., Faber, S. M., Koo, D. C., Gebhardt, K., Willmer, C. N. A., Phillips, A., Illingworth, G., Vogt, N. P., & Sarajedini, V. L. 2002, ApJ, 571, 136

Jeans, J. H. 1922, MNRAS, 82, 122

Jester, S., Schneider, D. P., Richards, G. T., Green, R. F., Schmidt, M., Hall, P. B., Strauss, M. A., Vanden Berk, D. E., Stoughton, C., Gunn, J. E., Brinkmann, J., Kent, S. M., Smith, J. A., Tucker, D. L., & Yanny, B. 2005, AJ, 130, 873

Jorgensen, I. 1997, MNRAS, 288, 161

Jorgensen, I., Franx, M., & Kjaergaard, P. 1996, MNRAS, 280, 167

Kauffmann, G. & White, S. D. M. 1993, MNRAS, 261, 921

Kauffmann, G., White, S. D. M., & Guiderdoni, B. 1993, MNRAS, 264, 201

Kaviraj, S., Schawinski, K., Devriendt, J. E. G., Ferreras, I., Khochfar, S., Yoon, S.-J., Yi, S. K., Deharveng, J.-M., Boselli, A., Barlow, T., Conrow, T., Forster, K., Friedman, P. G., Martin, D. C., Morrissey, P., Neff, S., Schiminovich, D., Seibert, M., Small, T., Wyder, T., Bianchi, L., Donas, J., Heckman, T., Lee, Y.-W., Madore, B., Milliard, B., Rich, R. M., & Szalay, A. 2007, ApJS, 173, 619

Khochfar, S. & Silk, J. 2006, MNRAS, 370, 902

Koopmans, L. V. E., Treu, T., Bolton, A. S., Burles, S., & Moustakas, L. A. 2006, ApJ, 649, 599

Kormendy, J. 1977, ApJ, 218, 333

Kormendy, J. & Bender, R. 1996, ApJ, 464, L119

Kormendy, J., Fisher, D. B., Cornell, M. E., & Bender, R. 2009, ApJS, 182, 216

Krajnović, D., Bacon, R., Cappellari, M., Davies, R. L., de Zeeuw, P. T., Emsellem, E., Falcón-Barroso, J., Kuntschner, H., McDermid, R. M., Peletier, R. F., Sarzi, M., van den Bosch, R. C. E., & van de Ven, G. 2008, MNRAS, 390, 93

Krajnović, D., Emsellem, E., Cappellari, M., Alatalo, K., Blitz, L., Bois, M., Bournaud, F., Bureau, M., Davies, R. L., Davis, T. A., de Zeeuw, P. T., Khochfar, S., Kuntschner, H., Lablanche, P.-Y., McDermid, R. M., Morganti, R., Naab, T., Oosterloo, T., Sarzi, M., Scott, N., Serra, P., Weijmans, A.-M., & Young, L. M. 2011, ArXiv, 1102.3801

Kuntschner, H., Emsellem, E., Bacon, R., Bureau, M., Cappellari, M., Davies, R. L., de Zeeuw, P. T., Falcón-Barroso, J., Krajnović, D., McDermid, R. M., Peletier, R. F., & Sarzi, M. 2006, MNRAS, 369, 497

Kuntschner, H., Emsellem, E., Bacon, R., Cappellari, M., Davies, R. L., de Zeeuw, P. T., Falcón-Barroso, J., Krajnović, D., McDermid, R. M., Peletier, R. F., Sarzi, M., Shapiro, K. L., van den Bosch, R. C. E., & van de Ven, G. 2010, MNRAS, 408, 97

Kuntschner, H., Lucey, J. R., Smith, R. J., Hudson, M. J., & Davies, R. L. 2001, MNRAS, 323, 615

Landsman, W. B. 1993, in Astronomical Society of the Pacific Conference Series, Vol. 52, Astronomical Data Analysis Software and Systems II, ed. R. J. Hanisch, R. J. V. Brissenden, & J. Barnes, 246

Lemaître, G. 1931, MNRAS, 91, 483

Lewis, A. D., Buote, D. A., & Stocke, J. T. 2003, ApJ, 586, 135

Lilly, S. J., Le Fevre, O., Hammer, F., & Crampton, D. 1996, ApJ, 460, L1

Lotz, J. M., Primack, J., & Madau, P. 2004, AJ, 128, 163

Mac Low, M.-M. & Ferrara, A. 1999, ApJ, 513, 142

Madau, P., Pozzetti, L., & Dickinson, M. 1998, ApJ, 498, 106

Morganti, R., de Zeeuw, P. T., Oosterloo, T. A., McDermid, R. M., Krajnović, D., Cappellari, M., Kenn, F., Weijmans, A., & Sarzi, M. 2006, MNRAS, 371, 157

Naab, T., Johansson, P. H., & Ostriker, J. P. 2009, ApJ, 699, L178

Naab, T., Johansson, P. H., Ostriker, J. P., & Efstathiou, G. 2007, ApJ, 658, 710

Navarro, J. F., Frenk, C. S., & White, S. D. M. 1996, ApJ, 462, 563

Norberg, P., Cole, S., Baugh, C. M., Frenk, C. S., Baldry, I., Bland-Hawthorn, J., Bridges, T., Cannon, R., Colless, M., Collins, C., Couch, W., Cross, N. J. G., Dalton, G., De Propris, R., Driver, S. P., Efstathiou, G., Ellis, R. S., Glazebrook, K., Jackson, C., Lahav, O., Lewis, I., Lumsden, S., Maddox, S., Madgwick, D., Peacock, J. A., Peterson, B. A., Sutherland, W., & Taylor, K. 2002, MNRAS, 336, 907

Oemler, Jr., A. 1974, ApJ, 194, 1

Ostriker, J. P. & Steinhardt, P. J. 1995, Nature, 377, 600

Paturel, G., Petit, C., Prugniel, P., Theureau, G., Rousseau, J., Brouty, M., Dubois, P., & Cambrésy, L. 2003, A&A, 412, 45

Pei, Y. C. 1995, ApJ, 438, 623

Penzias, A. A. & Wilson, R. W. 1965, ApJ, 142, 419

Percival, W. J., Baugh, C. M., Bland-Hawthorn, J., Bridges, T., Cannon, R., Cole, S., Colless, M., Collins, C., Couch, W., Dalton, G., De Propris, R., Driver, S. P., Efstathiou, G., Ellis, R. S., Frenk, C. S., Glazebrook, K., Jackson, C., Lahav, O., Lewis, I., Lumsden, S., Maddox, S., Moody, S., Norberg, P., Peacock, J. A., Peterson, B. A., Sutherland, W., & Taylor, K. 2001, MNRAS, 327, 1297

Percival, W. J., Reid, B. A., Eisenstein, D. J., Bahcall, N. A., Budavari, T., Frieman, J. A., Fukugita, M., Gunn, J. E., Ivezić, Ž., Knapp, G. R., Kron, R. G., Loveday, J., Lupton, R. H., McKay, T. A., Meiksin, A., Nichol, R. C., Pope, A. C., Schlegel, D. J., Schneider, D. P., Spergel, D. N., Stoughton, C., Strauss, M. A., Szalay, A. S., Tegmark, M., Vogeley, M. S., Weinberg, D. H., York, D. G., & Zehavi, I. 2010, MNRAS, 401, 2148

Perlmutter, S., Aldering, G., Goldhaber, G., Knop, R. A., Nugent, P., Castro, P. G., Deustua, S., Fabbro, S., Goobar, A., Groom, D. E., Hook, I. M., Kim, A. G., Kim, M. Y., Lee, J. C., Nunes, N. J., Pain, R., Pennypacker, C. R., Quimby, R., Lidman, C., Ellis, R. S., Irwin, M., McMahon, R. G., Ruiz-Lapuente, P., Walton, N., Schaefer, B., Boyle, B. J., Filippenko, A. V., Matheson, T., Fruchter, A. S., Panagia, N., Newberg, H. J. M., Couch, W. J., & The Supernova Cosmology Project. 1999, ApJ, 517, 565

Pipino, A., D'Ercole, A., Chiappini, C., & Matteucci, F. 2010, MNRAS, 407, 1347

Postman, M. & Geller, M. J. 1984, ApJ, 281, 95

Press, W. H. & Schechter, P. 1974, ApJ, 187, 425

Press, W. H., Teukolsky, S. A., Vetterling, W. T., & Flannery, B. P. 1992, Numerical recipes in FORTRAN. The art of scientific computing

Refregier, A. 2003, ARA&A, 41, 645

Renzini, A. & Ciotti, L. 1993, ApJ, 416, L49

Riess, A. G., Filippenko, A. V., Challis, P., Clocchiatti, A., Diercks, A., Garnavich, P. M., Gilliland, R. L., Hogan, C. J., Jha, S., Kirshner, R. P., Leibundgut, B., Phillips, M. M., Reiss, D., Schmidt, B. P., Schommer, R. A., Smith, R. C., Spyromilio, J., Stubbs, C., Suntzeff, N. B., & Tonry, J. 1998, AJ, 116, 1009

Rood, H. J., Page, T. L., Kintner, E. C., & King, I. R. 1972, ApJ, 175, 627

Rubin, V. C. & Ford, Jr., W. K. 1970, ApJ, 159, 379

Sánchez-Blázquez, P., Gorgas, J., & Cardiel, N. 2006a, A&A, 457, 823

Sánchez-Blázquez, P., Gorgas, J., Cardiel, N., & González, J. J. 2006b, A&A, 457, 787

Sánchez-Blázquez, P., Peletier, R. F., Jiménez-Vicente, J., Cardiel, N., Cenarro, A. J., Falcón-Barroso, J., Gorgas, J., Selam, S., & Vazdekis, A. 2006c, MNRAS, 371, 703

Sandage, A. 1961, The Hubble atlas of galaxies

Schechter, P. 1976, ApJ, 203, 297

Schiavon, R. P. 2007, ApJS, 171, 146

Schlegel, D. J., Finkbeiner, D. P., & Davis, M. 1998, ApJ, 500, 525

Schmidt, M. 1968, ApJ, 151, 393

Scodeggio, M., Giovanelli, R., & Haynes, M. P. 1998, AJ, 116, 2728

Scott, N., Cappellari, M., Davies, R. L., Bacon, R., de Zeeuw, P. T., Emsellem, E., Falcón-Barroso, J., Krajnović, D., Kuntschner, H., McDermid, R. M., Peletier, R. F., Pipino, A., Sarzi, M., van den Bosch, R. C. E., van de Ven, G., & van Scherpenzeel, E. 2009, MNRAS, 398, 1835

Sersic, J. L. 1968, Atlas de galaxias australes

Shapiro, K. L., Falcón-Barroso, J., van de Ven, G., de Zeeuw, P. T., Sarzi, M., Bacon, R., Bolatto, A., Cappellari, M., Croton, D., Davies, R. L., Emsellem, E., Fakhouri, O., Krajnović, D., Kuntschner, H., McDermid, R. M., Peletier, R. F., van den Bosch, R. C. E., & van der Wolk, G. 2010, MNRAS, 402, 2140

Shapley, H. 1921, Bulletin of the National Research Council, 2, 171

Silk, J. & Rees, M. J. 1998, A&A, 331, L1

Skrutskie, M. F., Cutri, R. M., Stiening, R., Weinberg, M. D., Schneider, S., Carpenter, J. M., Beichman, C., Capps, R., Chester, T., Elias, J., Huchra, J., Liebert, J., Lonsdale, C., Monet, D. G., Price, S., Seitzer, P., Jarrett, T., Kirkpatrick, J. D., Gizis, J. E., Howard, E., Evans, T., Fowler, J., Fullmer, L., Hurt, R., Light, R., Kopan, E. L., Marsh, K. A., McCallon, H. L., Tam, R., Van Dyk, S., & Wheelock, S. 2006, AJ, 131, 1163

Spergel, D. N., Verde, L., Peiris, H. V., Komatsu, E., Nolta, M. R., Bennett, C. L., Halpern, M., Hinshaw, G., Jarosik, N., Kogut, A., Limon, M., Meyer, S. S., Page, L., Tucker, G. S., Weiland, J. L., Wollack, E., & Wright, E. L. 2003, ApJS, 148, 175

Springel, V., Frenk, C. S., & White, S. D. M. 2006, Nature, 440, 1137

Springel, V., White, S. D. M., Jenkins, A., Frenk, C. S., Yoshida, N., Gao, L., Navarro, J., Thacker, R., Croton, D., Helly, J., Peacock, J. A., Cole, S., Thomas, P., Couchman, H., Evrard, A., Colberg, J., & Pearce, F. 2005, Nature, 435, 629

Springel, V., White, S. D. M., Tormen, G., & Kauffmann, G. 2001, MNRAS, 328, 726

Suh, H., Jeong, H., Oh, K., Yi, S. K., Ferreras, I., & Schawinski, K. 2010, ApJS, 187, 374

Tecza, M., Thatte, N., Clarke, F., Goodsall, T., & Symeonidis, M. 2006, New A Rev., 49, 647

Thomas, D., Maraston, C., Bender, R., & Mendes de Oliveira, C. 2005, ApJ, 621, 673

Thomas, J., Saglia, R. P., Bender, R., Thomas, D., Gebhardt, K., Magorrian, J., Corsini, E. M., & Wegner, G. 2007, MNRAS, 382, 657

Thomas, J., Saglia, R. P., Bender, R., Thomas, D., Gebhardt, K., Magorrian, J., Corsini, E. M., Wegner, G., & Seitz, S. 2011, ArXiv, 1103.3414

Trager, S. C., Faber, S. M., Worthey, G., & González, J. J. 2000, AJ, 120, 165

Tremaine, S., Gebhardt, K., Bender, R., Bower, G., Dressler, A., Faber, S. M., Filippenko, A. V., Green, R., Grillmair, C., Ho, L. C., Kormendy, J., Lauer, T. R., Magorrian, J., Pinkney, J., & Richstone, D. 2002, ApJ, 574, 740

Tremonti, C. A., Heckman, T. M., Kauffmann, G., Brinchmann, J., Charlot, S., White, S. D. M., Seibert, M., Peng, E. W., Schlegel, D. J., Uomoto, A., Fukugita, M., & Brinkmann, J. 2004, ApJ, 613, 898

Treu, T. & Koopmans, L. V. E. 2004, ApJ, 611, 739

Tukey, J. W. 1977, Exploratory data analysis

van Albada, T. S., Bahcall, J. N., Begeman, K., & Sancisi, R. 1985, ApJ, 295, 305

van den Bosch, R. C. E. & van de Ven, G. 2009, MNRAS, 398, 1117

van Dokkum, P. G. 2001, PASP, 113, 1420

Visvanathan, N. & Sandage, A. 1977, ApJ, 216, 214

Walker, T. P., Steigman, G., Kang, H.-S., Schramm, D. M., & Olive, K. A. 1991, ApJ, 376, 51

Weijmans, A., Cappellari, M., Bacon, R., de Zeeuw, P. T., Emsellem, E., Falcón-Barroso, J., Kuntschner, H., McDermid, R. M., van den Bosch, R. C. E., & van de Ven, G. 2009, MNRAS, 398, 561

Weijmans, A., Krajnović, D., van de Ven, G., Oosterloo, T. A., Morganti, R., & de Zeeuw, P. T. 2008, MNRAS, 383, 1343

White, S. D. M. & Rees, M. J. 1978, MNRAS, 183, 341

Willmer, C. N. A., Faber, S. M., Koo, D. C., Weiner, B. J., Newman, J. A., Coil, A. L., Connolly, A. J., Conroy, C., Cooper, M. C., Davis, M., Finkbeiner, D. P., Gerke, B. F., Guhathakurta, P., Harker, J., Kaiser, N., Kassin, S., Konidaris, N. P., Lin, L., Luppino, G., Madgwick, D. S., Noeske, K. G., Phillips, A. C., & Yan, R. 2006, ApJ, 647, 853

Wittman, D. M., Tyson, J. A., Kirkman, D., Dell'Antonio, I., & Bernstein, G. 2000, Nature, 405, 143

Wolf, C., Meisenheimer, K., Rix, H.-W., Borch, A., Dye, S., & Kleinheinrich, M. 2003, A&A, 401, 73

Worthey, G., Faber, S. M., Gonzalez, J. J., & Burstein, D. 1994, ApJS, 94, 687

Yamada, T., Kodama, T., Akiyama, M., Furusawa, H., Iwata, I., Kajisawa, M., Iye, M., Ouchi, M., Sekiguchi, K., Shimasaku, K., Simpson, C., Tanaka, I., & Yoshida, M. 2005, ApJ, 634, 861

Yi, S. K., Yoon, S.-J., Kaviraj, S., Deharveng, J.-M., Rich, R. M., Salim, S., Boselli, A., Lee, Y.-W., Ree, C. H., Sohn, Y.-J., Rey, S.-C., Lee, J.-W., Rhee, J., Bianchi, L., Byun, Y.-I., Donas, J., Friedman, P. G., Heckman, T. M., Jelinsky, P., Madore, B. F., Malina, R., Martin, D. C., Milliard, B., Morrissey, P., Neff, S., Schiminovich, D., Siegmund, O., Small, T., Szalay, A. S., Jee, M. J., Kim, S.-W., Barlow, T., Forster, K., Welsh, B., & Wyder, T. K. 2005, ApJ, 619, L111

Young, L. M., Bureau, M., Davis, T. A., Combes, F., McDermid, R. M., Alatalo, K., Blitz, L., Bois, M., Bournaud, F., Cappellari, M., Davies, R. L., de Zeeuw, P. T., Emsellem, E., Khochfar, S., Krajnović, D., Kuntschner, H., Lablanche, P., Morganti, R., Naab, T., Oosterloo, T., Sarzi, M., Scott, N., Serra, P., & Weijmans, A. 2011, ArXiv, 1102.4633

Zwicky, F. 1933, Helvetica Physica Acta, 6, 110

—. 1937, ApJ, 86, 217